The numerics of hydrostatic structured-grid coastal ocean models: state of the art and future perspectives

Knut Klingbeil, Florian Lemarié, Laurent Debreu, Hans Burchard

The numerics of hydrostatic structured-grid coastal ocean models: state of the art and future perspectives

Knut Klingbeil [a] Florian Lemarié [b] Laurent Debreu [b]
Hans Burchard [c]

[a] *Dept. of Mathematics, University of Hamburg, Germany*

[b] *Inria, Univ. Grenoble Alpes, CNRS, LJK, Grenoble F-38000, France*

[c] *Leibniz Institute for Baltic Sea Research Warnemünde, Seestraße 15, D-18119 Rostock, Germany*

Abstract

The state of the art of the numerics of hydrostatic structured-grid coastal ocean models is reviewed here. First, some fundamental differences in the hydrodynamics of the coastal ocean, such as the large surface elevation variation compared to the mean water depth, are contrasted against large scale ocean dynamics. Then the hydrodynamic equations as they are used in coastal ocean models as well as in large scale ocean models are presented, including parameterisations for turbulent transports. As steps towards discretisation, coordinate transformations and spatial discretisations based on a finite-volume approach are discussed with focus on the specific requirements for coastal ocean models. As in large scale ocean models, splitting of internal and external modes is essential also for coastal ocean models, but specific care is needed when drying & flooding of intertidal flats is included. As one obvious characteristic of coastal ocean models, open boundaries occur and need to be treated in a way that correct model forcing from outside is transmitted to the model domain without reflecting waves from the inside. Here, also new developments in two-way nesting are presented. Single processes such as internal inertia-gravity waves, advection and turbulence closure models are discussed with focus on the coastal scales. Some overview on existing hydrostatic structured-grid coastal ocean models is given, including their extensions towards non-hydrostatic models. Finally, an outlook on future perspectives is made.

Key words: coastal ocean models, hydrostatic models, adaptive coordinates, mode-splitting, drying & flooding, two-way nesting

1 Introduction

This review paper presents the state of the art numerics of the hydrodynamic cores of coastal ocean models, with focus on structured-grid hydrostatic models. Here, we define the coastal ocean as ranging from estuaries and shallow coastal areas to the shelf break region. On the small scale end, near-shore

(e.g., Stockdon et al., 2006) and coastal engineering (Rennau et al., 2012) scales are not resolved, but parameterised, if needed. On the large scale end, the dynamics of the ocean basins will not be explicitly treated, since their effects are introduced by means of lateral boundary conditions (see, e.g., Holt et al. (2009)).

The coastal ocean as defined here, is strongly affected by the superposition of direct human impacts and climate change and variability (Halpern et al., 2008). Direct human impacts include for example eutrophication (Conley et al., 2009), fishery (Jackson et al., 2001), large scale constructions (such as offshore wind farms (Carpenter et al., 2016)), dredging and dumping of material (Winterwerp et al., 2013), discharges (e.g., of cooling water (Hofmeister et al., 2013)) and pollution (Gao and Chen, 2012). Aspects of natural and anthropogenic climate change and variability impacting on the coastal ocean are relative sea level rise (global and local, e.g., Wahl et al. (2013)), global warming (e.g., Wiltshire and Manly, 2004), changes of the water cycle (precipitation, evaporation, run-off, e.g., Meier et al. (2006)), and changed wind forcing (e.g., Sydeman et al., 2014). These local, regional and global forcings may lead to severe changes in the coastal environment, such as coastal erosion (Feagin et al., 2005), flooding of low-laying coastal regions (Nicholls et al., 1999), increase of oxygen minimum zones (Diaz and Rosenberg, 2008), shifts in biodiversity and invasion of alien species (Lotze et al., 2006), and many more. Changes are strong in many coastal regions around the world (see, e.g., BACC II Author Team (2015) for the Baltic Sea and Quante and Colijn (2016) for the North Sea), but specifically serious in the Arctic where the warming is strongly accelerated (Screen and Simmonds, 2010).

Coastal ocean models can be applied on various scales to simulate scenarios to test management options, such as for example for nutrient reduction experiments (Neumann et al., 2002; Lenhart et al., 2010), or for coastal engineering scenarios (Rennau et al., 2012; Van Maren et al., 2016).

To understand the changing coastal oceans, numerical modelling is one of the most effective tools, allowing for reconstructions of historic states, hindcasts and analysis of the dynamics in the last decades, short term forecasts of coastal ocean states, as well as for coastal climate projections and possible future scenarios. One core requirement for the predictability of such model exercises is the way how basic hydrodynamic processes are reproduced.

Main aspects which need to be resolved are exchanges of matter (such as salt, heat, oxygen, nutrients and particulate matter) in vertical and lateral directions. In the lateral direction, the coast-to-ocean exchange is mediated by estuarine dynamics, tidal dispersion, tidal fronts, river plumes, and meso-scale and submeso-scale dynamics (see, e.g., Huthnance (1995); Wheless and Klinck (1995); Capet et al. (2008); Horner-Devine et al. (2015); Burchard and Badewien (2015)). In the vertical, critical interfaces play a crucial role, such as the sediment-water interface, the *clines* (lutocline, halocline, thermocline, redoxcline), the surface and bottom wave-affected layers as well as the air-sea interface (Ross and Mehta, 1989; Burchard et al., 2008). Internal waves play a special role for linking horizontal and vertical scales (Scotti and Pineda, 2004). All these features need to be properly resolved.

In this paper, we discuss specific requirements for models of the coastal ocean. The coupling of the hydrodynamic core with models for other compartments such as atmospheric models, wind wave models, sea ice models, hydrological models and bottom sediment models is not discussed in detail, as each of these topics deserves and requires an in-depth review on its own. Scales where resolution of non-hydrostatic effects become relevant will be parameterised such that we focus on hydrostatic models. The inclusion of the non-hydrostatic pressure contribution into an existing hydrostatic kernel is outlined. Furthermore, we restrict ourselves to the class of structured-grid models, since the numerical methods in unstructured-grid modelling differ significantly from the structured-grid methods. Due to their flexible grids, unstructured-

grid models are known to be specifically suitable for investigating multi-scale dynamics in the ocean. We will here discuss how also structured-grid models combined with nesting strategies are able to resolve multiple scales.

The paper is structured as follows: After this introduction, the specific properties of the coastal ocean are discussed in section 2. The class of mathematical equations on which coastal ocean models are generally based is presented in section 3, including momentum and tracer equations (section 3.1) and turbulence closures (section 3.2). Based on these equations, the most common coordinate transformations and related spatial discretisation methods are introduced (section 4), while temporal discretisation including mode-splitting and drying & flooding is presented in section 5. Section 6 is then dedicated to open boundary conditions and model nesting. The numerical treatment of single processes is discussed in section 7. Finally, the most common coastal ocean community models are presented in section 8 and an outlook is given in section 9.

2 Characteristics of coastal ocean dynamics

The coastal ocean has a number of characteristics which discriminate it from the global ocean in a way that specific physical and numerical treatment is required. In the following, these characteristics are expressed in terms of characteristic horizontal and vertical length scales H and L, respectively, and the time scale T.

2.1 Relatively thick mixed layers

In temperate shelf seas, the surface and bottom mixed layers may occupy a considerable fraction of the water depth. In summer, when stratification shows a maximum, they may still cover 60%-80% of the water column, while in autumn and winter they may completely merge into a vertically homogeneous water column (Bolding et al., 2002; Burchard and Rippeth, 2009). In contrast to this, surface and bottom mixed layers in ocean basins, which may have a comparable absolute thickness to shelf seas may cover only a small portion of the total depth of several thousands of metres (Martin, 1985).

With H being the local time-averaged water depth, and D_s and D_b denoting surface and bottom mixed layer thickness, respectively, this characteristics of coastal seas can be expressed as

$$\frac{D_s + D_b}{H} = \mathscr{O}(1) \tag{2.1}$$

The major consequence of this is that turbulence closure models are needed which resolve the vertical structure of the mixed layers including the interaction of vertical stratification and mixing (see Section 3.2.1). For the relatively thick bottom boundary layers, another implication is that the bed friction generates relatively strong dissipation of kinetic energy in the water column. The latter may be enhanced in shallow water, when the wave length of surface gravity waves becomes comparable to the water depth, such that the orbital wave motion adds to the bed stress. Due to the dynamic importance of the bottom boundary layer it is required that it is vertically well-resolved everywhere. Considering the generally strongly variable bottom bathymetry of the coastal ocean, this can be best achieved by *bottom-following vertical coordinates* (see section 4.2).

2.2 *Relatively high surface elevation amplitude*

Coastal ocean models need to accurately predict the temporally and spatially varying free surface elevation η. The sea surface elevation variability due to tides and storm surges is strongly enhanced in the shallow coastal ocean, adding an important non-linearity to the dynamics, which cannot be neglected in the model numerics. When denoting the standard deviation of the surface elevation as $\sigma(\eta)$, this characteristics of the coastal ocean could be formulated as

$$\frac{\sigma(\eta)}{H} = \mathcal{O}(1). \tag{2.2}$$

Furthermore, the relatively high surface elevation variation requires the use of *surface-following vertical coordinates* to ensure sufficient vertical resolution of the near surface region.

An extreme case occurs when the surface elevation variability is larger than the mean water depth, such that the sea bed is falling dry at times:

$$\frac{\sigma(\eta)}{H} > 1. \tag{2.3}$$

In such cases, drying & flooding algorithms must be implemented to prevent unphysical negative water depths (see Section 5.2).

2.3 *Relatively strong horizontal and vertical gradients*

In all eddy-resolving ocean models significant gradients due to detached eddies or upwelling can be found. However, by definition, all global riverine input is discharged into coastal seas. Since the exchange between the coasts and the interior of the adjacent shelf seas is limited, strong gradients build up in the coastal ocean. Therefore, salinity in coastal ocean models may vary from river concentration (almost zero) to ocean concentration within a few kilometres in the horizontal. It is this almost zero salinity that demands not only for accurate, but also positive-definite numerical transport schemes. Strong stratification may be generated in the vicinity of freshwater discharge such that also vertical gradients may be strong. In addition to the salinity, also other tracers such as nutrients or suspended matter discharged by rivers may show strong gradients.

2.4 *Relatively short response time*

Due to the shallow depth and the limited extension, the coastal ocean typically reacts much stronger and on much shorter time scales on external forcing than the global ocean. The key time scales in the coastal ocean are tidal, inertial, diurnal or synoptic, i.e. $\mathcal{O}(1\text{ day})$. One relevant time scale in the open ocean is the life time of mesoscale eddies, i.e. order of week(s). Large scale ocean studies often concentrate on much longer time scales by parameterising effects of tides, inertial oscillations or storms (see, e.g., Eden et al. (2014)). In estuaries and coastal regions, complex dynamical changes will occur during a tidal cycle with strong tidal asymmetries in mixing and secondary circulation, and substantial impact on transport e.g. of salt and suspended matter (see, MacCready and Geyer (2010)). One example for this is the strain-induced periodic stratification (SIPS, see Simpson et al. (1990)) due to horizontal density gradients as often observed in regions of freshwater influence (see, e.g., Rippeth et al., 2001). Interior mixing in shelf seas is often caused by inertial shear caused by episodic storm events combined with coastal coupling (Craig (1989); van Haren et al. (1999); Knight et al. (2002)), a process which cannot be parameterised

in the coastal ocean due to its complex bathymetry and coastline. Therefore, different model physics e.g. in terms of turbulence closure models (see the discussion at the end of section 3.2.1) requiring different numerical schemes are needed for coastal ocean models.

2.5 Relatively small spatial scales

Probably the most obvious characteristics of the coastal ocean is its limited spatial extent:

$$L \ll r_{Earth}, \tag{2.4}$$

with the Earth's radius r_{Earth}. Even if the entire coastal ocean is considered as one single global object (see concepts by Holt et al. (2009)), large scale global or regional drivers need to be transferred to the coastal ocean. For the remote meteorological forcing (weather systems) this is typically done by one-way or two-way nesting to a regional atmospheric model which itself is coupled to a global model. For the remote oceanic impact (tides, surges, planetary waves, etc.) this has to be done via lateral boundary conditions coming from external models. Therefore, the problem of *open boundary conditions (OBCs) and model nesting* is characteristic for coastal ocean models (as well as for the basin-scale ocean models), see the discussions in Section 6. As for horizontal scales, also vertical scales are often smaller in the coastal ocean than in the global ocean. Typically, the aspect ratio (depth to width ratio) is also sufficiently small in the coastal ocean to justify application of the hydrostatic approximation. Since the Rossby radii in the coastal ocean are often smaller than in the global ocean (see, e.g., Fennel et al. (1991)), only higher horizontal resolution allows for eddy resolving simulations.

3 Basic equations

3.1 Momentum and tracer equations

Coastal and large scale ocean models typically use a common set of dynamic equations, which is based on the Reynolds-averaged primitive equations including hydrostatic and Boussinesq approximations. Detailed derivations of these equations are e.g. found in Griffies and Adcroft (2008).

These equations are derived from the Navier-Stokes equations on the rotating Earth by first adopting the Boussinesq approximation which includes the use of a constant reference density ρ_0 (instead of the density ρ) in all terms except in the gravity term. This has the consequence that mass conservation is replaced by volume conservation. In a next step, the effects of small-scale turbulent fluctuations on the larger scales are considered in a parameterised way without the necessity to numerically resolve them. This procedure assumes an ensemble averaging of the Navier-Stokes equations resulting in the Reynolds-averaged Navier-Stokes equations which now include unknown turbulent stresses which need to be parameterised (see section 3.2). Finally, a scaling analysis assuming a small aspect ratio (vertical scales are much smaller than horizontal scales) motivates the degeneration of the vertical component of the momentum equation to the hydrostatic balance, neglecting vertical acceleration, the non-linear and the stress divergence terms and the effects of Earth rotation (see the discussion in Kanarska et al., 2007; Klingbeil and Burchard, 2013). The hydrostatic approximation enforces the traditional approximation for the Coriolis terms, neglecting the horizontal contributions of Earth rotation in the horizontal momentum equations. The dynamic equations are here for simplicity expressed in local Cartesian coordinates. After inserting the Boussinesq

approximation into the mass conservation equation, the incompressibility condition remains:

$$\partial_x u + \partial_y v + \partial_z w = 0, \tag{3.1}$$

with the Cartesian coordinates (x, y, z) (eastwards, northwards, upwards), and (u, v, w) being the Cartesian components of the three-dimensional velocity vector $\mathbf{u}$.

Applying the incompressibility condition (3.1) and the hydrostatic condition (with pressure p and gravitational acceleration $g = 9.81\,\mathrm{m\,s^{-2}}$),

$$\partial_z p = -g\rho, \tag{3.2}$$

(remainder of the vertical component of the Navier-Stokes equations) into the horizontal momentum equations, the resulting dynamic equations are of the following form:

$$\begin{aligned} &\partial_t u + \partial_x \left(u^2\right) + \partial_y \left(uv\right) + \partial_z \left(uw\right) \\ &= \partial_x T_{\mathrm{xx}} + \partial_y T_{\mathrm{yx}} + \partial_z T_{\mathrm{zx}} + fv - \frac{1}{\rho_0}\partial_x p_a - g\partial_x \eta + \partial_x \int_z^\eta b\,\mathrm{d}z' \end{aligned} \tag{3.3}$$

and

$$\begin{aligned} &\partial_t v + \partial_x \left(vu\right) + \partial_y \left(v^2\right) + \partial_z \left(vw\right) \\ &= \partial_x T_{\mathrm{xy}} + \partial_y T_{\mathrm{yy}} + \partial_z T_{\mathrm{zy}} - fu - \frac{1}{\rho_0}\partial_y p_a - g\partial_y \eta + \partial_y \int_z^\eta b\,\mathrm{d}z', \end{aligned} \tag{3.4}$$

with time t, the local Coriolis frequency $f = 2\Omega\sin(\phi)$ (with the angular speed of Earth rotation $\Omega = 7.29 \cdot 10^{-5}\mathrm{s}^{-1}$ and the latitude ϕ), the surface elevation η, and the surface pressure p_a. T_{ij} are the Cartesian components of the viscous stress tensor $\mathbf{T}$. The terms on the right hand sides of (3.3) and (3.4) are the stress divergence terms, the Coriolis term and the horizontal pressure gradient components $\partial_x p/\rho_0$ and $\partial_y p/\rho_0$, with the latter already split into the external pressure gradient (composed of the atmospheric pressure gradient and the surface slope) and the internal pressure gradient, where $b = -(g/\rho_0)(\rho - \rho_0)$ is the buoyancy. In (3.3) and (3.4), the flux form for the advective terms is used, which results for any quantity q from the incompressibility condition (3.1):

$$u\partial_x q + v\partial_y q + w\partial_z q = \partial_x(uq) + \partial_y(vq) + \partial_z(wq), \tag{3.5}$$

which is the preferred form for coastal models in contrast to large-scale models sometimes based on the vector-invariant form for nonlinear terms (see section 7.1). Equations (3.3) and (3.4) are valid for $-H(x, y) \le z \le \eta(x, y, t)$ (with the bottom coordinate $z = -H$). Dynamic boundary conditions at the free surface are

$$\nabla(z - \eta) \cdot \mathbf{T}\Big|_{z=\eta} = \boldsymbol{\tau}^{\mathrm{s}}, \tag{3.6}$$

with the horizontal Cartesian components of the surface stress vector $(\tau_{\mathrm{x}}^{\mathrm{s}}, \tau_{\mathrm{y}}^{\mathrm{s}})$, calculated from meteorological data using bulk formulae (e.g., Kondo (1975); Fairall et al. (1996)) [1]. At the bottom, the dynamic boundary conditions are the no-slip conditions

$$\nabla(z + H) \cdot \mathbf{u}\Big|_{z=-H} = 0. \tag{3.7}$$

[1] Note that the physical stress in units of Pa is obtained as $\rho_0\boldsymbol{\tau}^{\mathrm{s}}$. The vertical component can be absorbed into the surface pressure.

For numerical reasons, however, generally an equivalent flux boundary condition is applied,

$$\nabla(z+H)\cdot\mathbf{T}\Big|_{z=-H}=\boldsymbol{\tau}^{\mathrm{b}}, \tag{3.8}$$

with the horizontal Cartesian components of the bed stress vector $(\tau_{\mathrm{x}}^{\mathrm{b}},\tau_{\mathrm{y}}^{\mathrm{b}})$ reconstructed from a logarithmic velocity profile (see Section 7.6) [2] .

Kinematic surface and bottom boundary conditions are:

$$w\Big|_{z=\eta}=\partial_t\eta+u\Big|_{z=\eta}\partial_x\eta+v\Big|_{z=\eta}\partial_y\eta+(E-P), \tag{3.9a}$$

$$w\Big|_{z=-H}=-u\Big|_{z=-H}\partial_x H-v\Big|_{z=-H}\partial_y H, \tag{3.9b}$$

with the evaporation rate E and the precipitation rate P. River run-off can be treated in various ways, e.g. as lateral boundary condition.

There is a large variety of lateral boundary conditions, which will be further discussed in section 6.

Within the Boussinesq approximation, the budget equation for internal energy reduces to a conservation equation for conservative temperature Θ:

$$\partial_t\Theta+\partial_x\left(u\Theta\right)+\partial_y\left(v\Theta\right)+\partial_z\left(w\Theta\right)=-\partial_x J_{\mathrm{x}}^{\Theta}-\partial_y J_{\mathrm{y}}^{\Theta}-\partial_z J_{\mathrm{z}}^{\Theta}+\frac{1}{C_p\rho_0}\partial_z I, \tag{3.10}$$

with the horizontal and vertical turbulent fluxes of Θ given by $J_{[x,y,z]}^{\Theta}$, the specific heat capacity of water at constant pressure, C_p, and irradiance in water, I. The positive vertical gradient of irradiance depends on the light absorption model applied. A classical model would be the model by Paulson and Simpson (1977), but often more complex models taking into account water colour, suspended matter and biogeochemical components are used. In (3.10), the heating due to viscous dissipation of turbulent kinetic energy is neglected, since in comparison to other terms in the local heat budget of the ocean this is a very small term (in contrast to conditions in the higher atmosphere). The surface boundary condition for the turbulent flux of temperature is formulated as

$$\nabla(z-\eta)\cdot\mathbf{J}^{\Theta}\Big|_{z=\eta}=\frac{Q_s+Q_l+Q_b}{C_p\rho_0}, \tag{3.11}$$

with the sensible heat flux Q_s (due to the air-sea temperature difference), the latent heat flux Q_l (due to evaporation), and the long-wave back radiation Q_b. Note that upward (positive) fluxes of temperature lead to cooling at the surface. For the parameterisation of these heat fluxes various models are available, with the bulk formulae by Kondo (1975) and Fairall et al. (1996) being the most common ones for coastal applications.

The conservation equation for the absolute salinity S is of similar form as the temperature conservation equation, but without source term:

$$\partial_t S+\partial_x\left(uS\right)+\partial_y\left(vS\right)+\partial_z\left(wS\right)=-\partial_x J_{\mathrm{x}}^{\mathrm{S}}-\partial_y J_{\mathrm{y}}^{\mathrm{S}}-\partial_z J_{\mathrm{z}}^{\mathrm{S}}. \tag{3.12}$$

In order to guarantee that no salt crosses the free surface, the diffusive salinity flux at the surface must compensate the advective salinity flux associated with (3.9a),

$$\nabla(z-\eta)\cdot\mathbf{J}^{\mathrm{S}}\Big|_{z=\eta}=-(E-P)S, \tag{3.13}$$

[2] The vertical component is not considered in hydrostatic models.

see Beron-Vera et al. (1999) for details. In contrast to this analytical formulation, in the discrete model equations the salinity of the surface freshwater flux simply can be set to zero and no compensating diffusive salinity flux is necessary (see end of Section 4.1). The density is calculated by means of an empirical equation of state as function of temperature Θ, salinity S and pressure p:

$$\rho = \rho(\Theta, S, p). \tag{3.14}$$

A recent and accurate formulation for Boussinesq models has been provided by Roquet et al. (2015). This is based on the new international standard TEOS-10 (IOC, SCOR and IAPSO, 2010), replacing the old thermodynamic description of seawater EOS-80 from Fofonoff and Millard Jr. (1983).

3.2 Turbulence closure

Turbulence closure modelling involves complex theories. For an overview, the reader is referred to text books (Kantha and Clayson, 2000b; Griffies, 2004; Cushman-Roisin and Beckers, 2011; Olbers et al., 2012). The parameterisation of the viscous stress tensor is usually based on a transversely isotropic Newtonian viscosity tensor, yielding

$$T_{\mathrm{z}[x,y]} = K_{\mathrm{M}} \partial_z [u, v], \tag{3.15}$$

with the vertical eddy viscosity K_{M}, and two possible formulations with the horizontal eddy viscosity A_{M}:

$$\begin{bmatrix} T_{\mathrm{xx}} & T_{\mathrm{yx}} \\ T_{\mathrm{xy}} & T_{\mathrm{yy}} \end{bmatrix} (u, v) = A_{\mathrm{M}} \begin{bmatrix} 2\partial_x u & \partial_y u + \partial_x v \\ \partial_y u + \partial_x v & 2\partial_y v \end{bmatrix}, \tag{3.16}$$

or

$$\begin{bmatrix} T_{\mathrm{xx}} & T_{\mathrm{yx}} \\ T_{\mathrm{xy}} & T_{\mathrm{yy}} \end{bmatrix} (u, v) = A_{\mathrm{M}} \begin{bmatrix} \partial_x u - \partial_y v & \partial_y u + \partial_x v \\ \partial_y u + \partial_x v & -(\partial_x u - \partial_y v) \end{bmatrix}. \tag{3.17}$$

Both formulations are valid for incompressible fluids, but only (3.17) is also valid for compressible ones. An alternative to the resulting Laplacian friction operator in (3.3) and (3.4) is biharmonic friction, which more selectively acts on the smallest resolved scales and reduces the overdissipation of the larger flow features (Griffies and Hallberg, 2000). In (3.16) and (3.17) the turbulent fluxes are oriented in the horizontal direction. Since the transformation of the stress divergence to general vertical coordinates is cumbersome, the momentum diffusion is usually simply carried out along coordinate surfaces. Whereas this treatment is justified for the anyhow highly empirical momentum fluxes, more care is necessary for scalar tracer fluxes. In most ocean models, vertical and horizontal turbulent fluxes of scalars are parameterised by a down-gradient approximation of the form

$$\mathbf{J}^c = -(A_c \mathbf{R} + K_c \hat{\mathbf{z}} \otimes \hat{\mathbf{z}}) \cdot \nabla c, \tag{3.18}$$

using lateral and vertical eddy diffusivities A_c and K_c for any scalar c. Whereas the vertical diffusivity is defined in the direction of the vertical unit vector $\hat{\mathbf{z}}$, the lateral diffusivity acts in a direction depending on the rotation tensor $\mathbf{R}$ (see Section 7.5.1). In the simplest case, the turbulent tracer fluxes are given by $J^c_{[x,y]} = -A_c \partial_{[x,y]} c$ and $J^c_z = -K_c \partial_z c$.

3.2.1 *Vertical turbulence modelling*

For the parametrisation of vertical eddy viscosity and diffusivity two basic approaches are commonly used in ocean models.

One of them is based on direct algebraic computation of the eddy parameters from bulk properties (boundary fluxes, mixed layer depth, bulk Richardson number) of the surface and bottom mixed layers, the so-called K-profile parameterisation (KPP) which has been originally proposed for large-scale ocean models by Large et al. (1994). In addition to the down-gradient fluxes, also counter-gradient flux components (for example for convectively unstable boundary layers) are included in the KPP model. Many modifications of the original KPP model have been proposed (see, e.g., Smyth et al., 2002; Durski et al., 2004; Uchiyama et al., 2010) to extend its applicability also to coastal ocean applications (see, e.g., Blaas et al., 2007). The KPP model assumes that the boundary layer turbulence is in equilibrium with the surface or bottom fluxes, respectively. For large scale ocean models, this might often be an adequate approximation. In many coastal model applications however, the deviation from this equilibrium is a first-order process which cannot be neglected.

The other closure approach, which in contrast to the KPP model considers high temporal and spatial variability in boundary layers, is based on a dynamic equation for the turbulent kinetic energy (TKE), k, which can be derived from the Navier-Stokes equations by means of Reynolds-averaging (Wilcox, 1998; Burchard, 2002a):

$$\partial_t k + \partial_x (uk) + \partial_y (vk) + \partial_z (wk) - \partial_z \left(\frac{K_\mathrm{M}}{Sc_k} \frac{\partial k}{\partial z} \right) = P + B - \varepsilon, \tag{3.19}$$

with the shear production, $P = K_\mathrm{M} M^2$ including the vertical shear squared, M^2, and the buoyancy production, $B = -K_c N^2$, with the buoyancy frequency (or Brunt-Väisälä frequency) squared, N^2, and the dissipation rate, ε. The shear production P transfers kinetic energy lost from the mean flow due to vertical stress divergence to the turbulent kinetic energy, whereas the buoyancy production B exchanges energy between the mean potential energy to the turbulent kinetic energy. Note, that in (3.19) the down-gradient approximation has been adopted with the turbulent Schmidt number Sc_k, which is of order unity. Horizontal turbulent fluxes are generally neglected for the TKE budget (Delhez et al., 1999). This may also be the case for the advective terms, but in tidally energetic regimes, such a neglect might lead to significant errors or instabilities. In addition to the TKE, also the length scale of the energy containing eddies, l, needs to be approximated to obtain an estimate for the vertical eddy viscosity and eddy diffusivity. Once k and l are known, the vertical eddy coefficients can be calculated as

$$K_\mathrm{M} = S_\mathrm{M} k^{1/2} l, \qquad K_c = S_c k^{1/2} l, \tag{3.20}$$

with the non-dimensional stability functions S_M and S_c. The dissipation rate ε can be calculated from l via the cascading relation, derived from integration of the kinetic energy spectrum over the inertial subrange,

$$\varepsilon = c_\varepsilon \frac{k^{3/2}}{l} \tag{3.21}$$

with the empirical constant c_ε. In stably stratified turbulence, l is often limited by the buoyancy scale $L_b = k^{1/2}/N$ (Galperin et al., 1988; Burchard, 2002a). To avoid unrealistically low diapycnal diffusivities in the thermocline, unresolved TKE production due to internal wave breaking is parameterized by a prescibed minimum TKE (Bolding et al., 2002). Surface and bottom boundary conditions are typically derived from the law of the wall, resulting in k being proportional to the surface or bed stress, respectively, and the length

scale to be proportional to the respective roughness length. Equivalent flux conditions, which proved to be numerically more stable have been proposed (Burchard and Petersen, 1999). To parameterise effects of breaking surface waves, injection of TKE at the surface is applied (Burchard, 2001). Effects of Langmuir Circulation on the dynamics of the surface mixed layer may be parameterised as well (see, e.g., Harcourt, 2014). Additional frictional effects of surface waves on wave drag in shallow water can also be considered in the bottom boundary condition (Mellor, 2002).

Various methods are used in ocean modelling to calculate the length scale l. In one-equation turbulence closure models (the one equation is for the computation of the TKE), l is calculated from combinations of geometric length scales (such as the distance from the surface or the bottom) or from hydrodynamic length scales (such as the Ozmidov scale), see e.g., Mellor and Yamada (1982); Gaspar et al. (1990). More common in coastal ocean models are however two-equation turbulence closure models which in addition to the TKE equation calculate a budget equation for an independent length-scale related quantity. Most commonly, a budget equation for the dissipation rate ε (k-ε models, see Rodi, 1987; Burchard and Baumert, 1995) is constructed and closed by the assumption that the source and sink terms can be modelled as a linear combination of P, B and ε. Instead of ε, also other length-scale-related properties could be budgeted (Mellor and Yamada, 1982; Wilcox, 1998; Umlauf and Burchard, 2003). However, when properly calibrated, all these two-equation models which differ only in the turbulent transport term perform similarly (Burchard et al., 1998; Umlauf and Burchard, 2003; Warner et al., 2005).

Two-equation turbulence closure models including algebraic second-moment closures as outlined here (see also the review by Umlauf and Burchard, 2005) have proven in many applications as a good compromise between computational efficiency and realistic representation of relevant processes in the coastal ocean.

There is a number of reasons, why such second-moment turbulence closure models are an important feature of coastal ocean models. First of all, as discussed in section 2.1, a large portion of water columns in the coastal ocean (if not the entire water column) are covered by surface or bottom boundary layers. These boundary layers have a vertical structure which locally influences the mixing coefficients. One example is tidal straining in coastal regions of freshwater influence, where flood shear destabilises and ebb shear stabilises the water water column, leading to asymmetric eddy coefficients and residual currents (Jay and Musiak, 1994; Rippeth et al., 2001). Therefore, boundary layer models reacting on local forcing instead of surface or bottom fluxes only are required. Secondly, relevant times scale in the coastal ocean are much shorter than in the global ocean (see section 2.4). Therefore, the turbulence closure models need to react on correct time scales to rapid time changes in surface or bottom stress instead of instantaneouly adjusting the eddy coefficients in the entire mixed layers such as in the KPP model. Such requirements are only fulfilled by carefully calibrated second-moment turbulence closure models. Nonetheless, successful implementations of extended KPP models to coastal ocean scenarios on shelf sea scale have been reported (Durski et al., 2004; Wilkin et al., 2005).

There are a few global ocean models using low-level second-moment closures (see, e.g., Oschlies (2002); Danabasoglu et al. (2014)), which typically are based on the Gaspar et al. (1990) one-equation model, where the turbulent length scale l is algebraically computed. Two-equation turbulence closure models are typically not used in global ocean models. For climate models, this is mainly due to the large baroclinic time steps (about 1 hour) and the coarse resolution in boundary layers. In high-resolution global models, temporal and spatial resolution of boundary layers may be sufficiently high for applying two-equation turbulence closure models, but there, the focus is still more on bulk effects of the boundary layers on transmitting fluxes between ocean and atmosphere or ocean and sea floor, rather than resolving

their dynamics. Therefore, in large-scale ocean models, the KPP model (see above) or other models with reduced dynamics (see, e.g., Jackson et al. (2008)) are used.

3.2.2 Horizontal subgrid-scale closure

Whereas in ocean models a consistent theoretical framework for the vertical turbulent fluxes exists, such a rigorous closure for the horizontal turbulent fluxes due to meso-scale and submeso-scale eddies is still missing. For large scale ocean models which do not resolve meso-scale eddies, closures have been proposed, such as the Gent and McWilliams (1990) closure for isopycnal mixing or the dynamic meso-scale eddy closure by Eden and Greatbatch (2008). In addition, for high-resolution global models submeso-scale eddy closures (Fox-Kemper et al., 2011) and flow-dependent subgrid-scale closures (Pearson et al., 2017) have been investigated. Coastal ocean models usually do not deal with sophisticated eddy parameterisations. This practice is motivated by the high horizontal resolution, and the difficult treatment of isopycnal eddy-induced fluxes in well-mixed coastal areas and their rotation in vertically boundary-following coordinates. Two simplistic common approaches used in the coastal ocean modelling community are to either neglect horizontal turbulent fluxes (and then rely on the diffusive fluxes associated with monotone, upstream-biased advection schemes, see section 7.1 or to set A_{M} and A_c to constant values. In the latter case, the proper choice of the horizontal exchange coefficients is then determined by sensitivity studies. Alternatively, a flow- and resolution-dependent parameterisation of the horizontal momentum fluxes proposed by Smagorinsky (1963) is applied. Consistent with (3.16) or (3.17) the horizontal eddy viscosity can be derived from dimensional analysis in terms of the local shear, strain and tension rates of the flow as

$$A_{\mathrm{M}} = C_{\mathrm{M}}(\Delta x\,\Delta y)\sqrt{(\partial_x u)^2 + \tfrac{1}{2}(\partial_y u + \partial_x v)^2 + (\partial_y v)^2}, \tag{3.22}$$

or

$$A_{\mathrm{M}} = C_{\mathrm{M}}(\Delta x\,\Delta y)\sqrt{\tfrac{1}{2}(\partial_x u - \partial_y v)^2 + \tfrac{1}{2}(\partial_y u + \partial_x v)^2}. \tag{3.23}$$

The empirical parameter C_{M} has been estimated for (3.22) by Holt and James (2006) in a shelf sea application as $C_{\mathrm{M}} \approx 0.2$. For decreasing horizontal grid sizes Δx and Δy the horizontal eddy viscosity becomes smaller, which is reasonable, as it represents the reduced effect of subgrid-scale eddies. The same approach as (3.22) or (3.23) may also be applied for horizontal tracer diffusivities by using a horizontal turbulent Prandtl number as proportionality factor. One important deficiency of the Smagorinsky closure is the assumption of isotropic turbulence, which limits the physical justification at least for large-scale geophysical flows (Griffies and Hallberg, 2000; Fox-Kemper and Menemenlis, 2008; Bachmann et al., 2017).

4 Coordinate transformations and spatial discretisation

The set of governing equations, consisting of the continuity equation (3.1), the hydrostatic momentum equations (3.3) and (3.4), and the prognostic equations for temperature (3.10) and salinity (3.12), so far has been formulated in a local Cartesian reference frame at the Earth surface for simplicity. However, the transformation to coordinate systems that align with the geometry of the domain is often advantageous.

Most coastal ocean models support orthogonal curvilinear coordinates in the horizontal to offer the formulation in spherical coordinates and to some extent the alignment with coastlines. Orthogonal curvilinear coordinates also provide some flexibility to increase the horizontal resolution in certain parts of the domain such as estuaries or towards the coast as required to resolve the typically strong near-coastal horizontal gradients, see Section 2.3. In this way also structured-grid models can be used for multi-scale applications.

The corresponding basis transformation to orthogonal curvilinear coordinates introduces additional metric coefficients (see, e.g. Kantha and Clayson (2000a)). For clarity, the governing equations in the remainder of this review will be kept in horizontal Cartesian coordinates.

In the vertical the alignment with the boundaries (free surface and bottom topography) and proper resolution (of e.g. the boundary layers and pycnoclines) is even more critical than in the horizontal. A general description that supports various types of vertical coordinates is given by the s-coordinates of Kasahara (1974). The general vertical coordinate $s(x, y, z, t)$ must be strictly monotone in z in order to guarantee a unique inverse transformation $z(x, y, s, t)$ and a well-defined Jacobian $\partial_s z = (\partial_z s)^{-1}$ for the transformation of the governing equations. For isopycnal coordinates $s = \rho$ this precludes the representation of unstable stratification. The horizontal coordinates and time do not change under the transformation and, if necessary for the purpose of clarity, derivatives with respect to constant s and z will be distinguished by $(\cdot)_s$ and $(\cdot)_z$, respectively. With the Lagrangian derivative $\mathrm{D}/\mathrm{D}t$ the dia-surface velocity component (see, e.g., Griffies (2004)) is given by

$$w^{\mathrm{s}} = \partial_s z \frac{\mathrm{D}s}{\mathrm{D}t} = w - (\partial_t z)_s - u\,(\partial_x z)_s - v\,(\partial_y z)_s\,. \tag{4.1}$$

Coastal ocean models traditionally discretise the governing equations on an Arakawa C-grid (Arakawa and Lamb, 1977), as the Rossby radius of deformation is usually properly resolved and the C-grid arrangement offers a better representation of small coastal inlets. In the vertical the corresponding variable arrangement is known as Lorenz grid (Lorenz, 1960). This fully staggered arrangement of velocities between tracer points also naturally fits to a conservative Finite-Volume discretisation around tracer cells (see Fig. 1). The corresponding discrete equations can be derived from the continuous ones by integration over a discrete control volume cell. Thereby divergence terms are cast into differences of fluxes through opposite cell interfaces. In order to demonstrate the procedure, in the following only the integration along the vertical dimension is carried out.

4.1 Layer-integrated equations

The vertical discretisation of the transformed space into $k_{\max}$ layers with interfaces at fixed levels $s_{k+1/2}$ (independent of x, y, t and with $k \in [0, k_{\max}]$) is equivalent to a discretisation of the physical space into $k_{\max}$ layers with interfaces at variable levels $z_{k+1/2}\,(x, y, t) = z\left(x, y, s_{k+1/2}, t\right)$ and $z_{k+1/2} > z_{k-1/2}$, see Burchard and Petersen (1997).

With layer heights $h_k(x, y, t) = \int_{s_{k-1/2}}^{s_{k+1/2}} \partial_s z \mathrm{d}s = z_{k+1/2} - z_{k-1/2}$, layer-averaged prognostic quantities $q_k(x, y, t) = h_k^{-1} \int_{z_{k-1/2}}^{z_{k+1/2}} q\,\mathrm{d}z$, for $k \in [1, k_{\max}]$ and $q \in \{1, u, v, \Theta, S\}$, and $w^{\mathrm{s}}_{k+1/2}\,(x, y, t) = w^{\mathrm{s}}\left(x, y, z_{k+1/2}, t\right)$, the layer-integration of (3.1), (3.3), (3.4), (3.10) and (3.12) yields the prototype equation:

$$\begin{aligned}\partial_t\,(h_k q_k) + \partial_x\,(h_k u_k q_k) + \partial_y\,(h_k v_k q_k) + \left(w^{\mathrm{s}}_{k+1/2}\tilde{q}_{k+1/2} - w^{\mathrm{s}}_{k-1/2}\tilde{q}_{k-1/2}\right)& \\ = -\partial_x\left(h_k J^{\mathrm{q}}_{\mathrm{x},k}\right) - \partial_y\left(h_k J^{\mathrm{q}}_{\mathrm{y},k}\right) - \left(J^{\mathrm{q}}_{\mathrm{z},k+1/2} - J^{\mathrm{q}}_{\mathrm{z},k-1/2}\right) + h_k F^{\mathrm{q}}_k.&\end{aligned} \tag{4.2}$$

In (4.2) the interfacial values $\widetilde{q}_{k+1/2}$ with $q \in \{u, v, \Theta, S\}$ are approximated by the vertical advection scheme, see Sec. 7.1. According to (4.1) the kinematic boundary conditions (3.9a) and (3.9b) transform to $w^{\mathrm{s}}_{k_{\max}+1/2} = E - P$ and $w^{\mathrm{s}}_{1/2} = 0$.

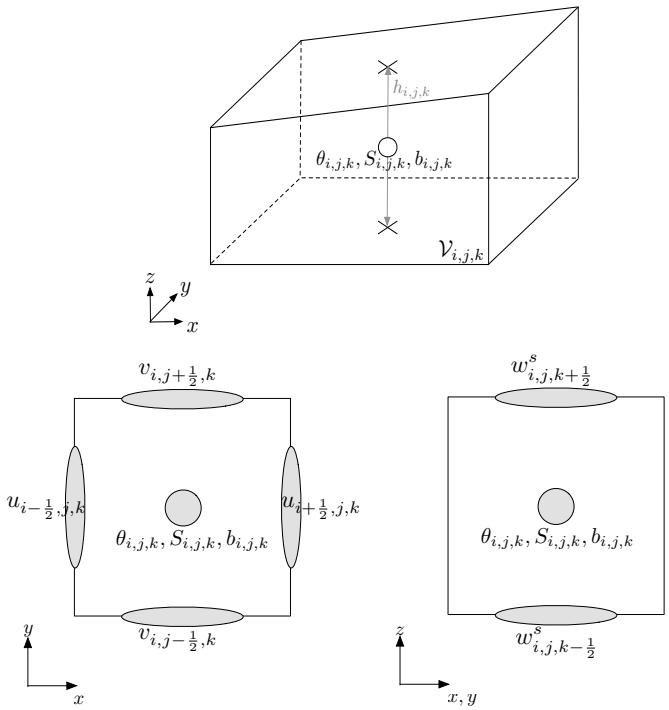

Fig. 1. Control volume for cell-centered tracer variables (top), staggering showing the location of the dependent variables in the horizontal (bottom, left) and in the vertical (bottom, right).

The full set of layer-integrated equations can be found in A. The layer-integrated continuity equation (A.1) can be obtained from (4.2) with $q = 1$ and $\mathbf{J}^1_k = F^1_k = 0$.

Within the layer-integrated momentum equations (A.2) and (A.3) the momentum fluxes through the interfaces, i.e. the vertical shear stresses, are defined as

$$-J^{[\mathrm{u,v}]}_{\mathrm{z},k+1/2} = \tau_{[\mathrm{x,y}],k+1/2} = \begin{cases} \tau^{\mathrm{s}}_{[\mathrm{x,y}]}(u_{k_{\max}}, v_{k_{\max}}), & k = k_{\max} \\ K_{\mathrm{M},k+1/2}\dfrac{[u,v]_{k+1} - [u,v]_k}{z_{k+1} - z_k}, & k \in [1, k_{\max} - 1]\,, \\ \tau^{\mathrm{b}}_{[\mathrm{x,y}]}(h_1, u_1, v_1), & k = 0 \end{cases} \tag{4.3}$$

based on (3.15) with the dynamic boundary conditions (3.6) and (3.8), and with centre positions $z_k = \frac{1}{2}\left(z_{k-1/2} + z_{k+1/2}\right)$. Following the discussion in Section 3.2, the lateral contributions of the stress tensor are often approximated according to Mellor and Blumberg (1985) and Kantha and Clayson (2000a):

$$\widetilde{F}^{\mathrm{h}}_{[\mathrm{x,y}]}(h,u,v) = \frac{1}{h}\left(\partial_x\left(hT_{\mathrm{x}[\mathrm{x,y}]}(u,v)\right) + \partial_y\left(hT_{\mathrm{y}[\mathrm{x,y}]}(u,v)\right)\right), \tag{4.4}$$

i.e. $J^{\mathrm{u}}_{[\mathrm{x,y}]} = -T_{[\mathrm{x,y}]\mathrm{x}}$ and $J^{\mathrm{v}}_{[\mathrm{x,y}]} = -T_{[\mathrm{x,y}]\mathrm{y}}$ in (4.2), with the components of the stress tensor $T_{\alpha\beta}$ given by (3.16) or (3.17) and all gradients calculated along layer k. In case of diffusion along directions not aligned with constant s, additional terms due to non-diagonal elements of the diffusion tensor would occur (Griffies (2004)). One numerically demanding contribution to $F^{[\mathrm{u,v}]}_k$ is the internal pressure gradient force given by

$$F^{\mathrm{IPG}}_{[\mathrm{x,y}],k} = \frac{1}{h_k}\int_{z_{k-1/2}}^{z_{k+1/2}} \left(\partial_{[x,y]}\right)_z \int_z^\eta b(x,y,z')\mathrm{d}z'\mathrm{d}z, \tag{4.5}$$

and approximated in terms of the layer-averaged buoyancies b_k (see Section 7.2).

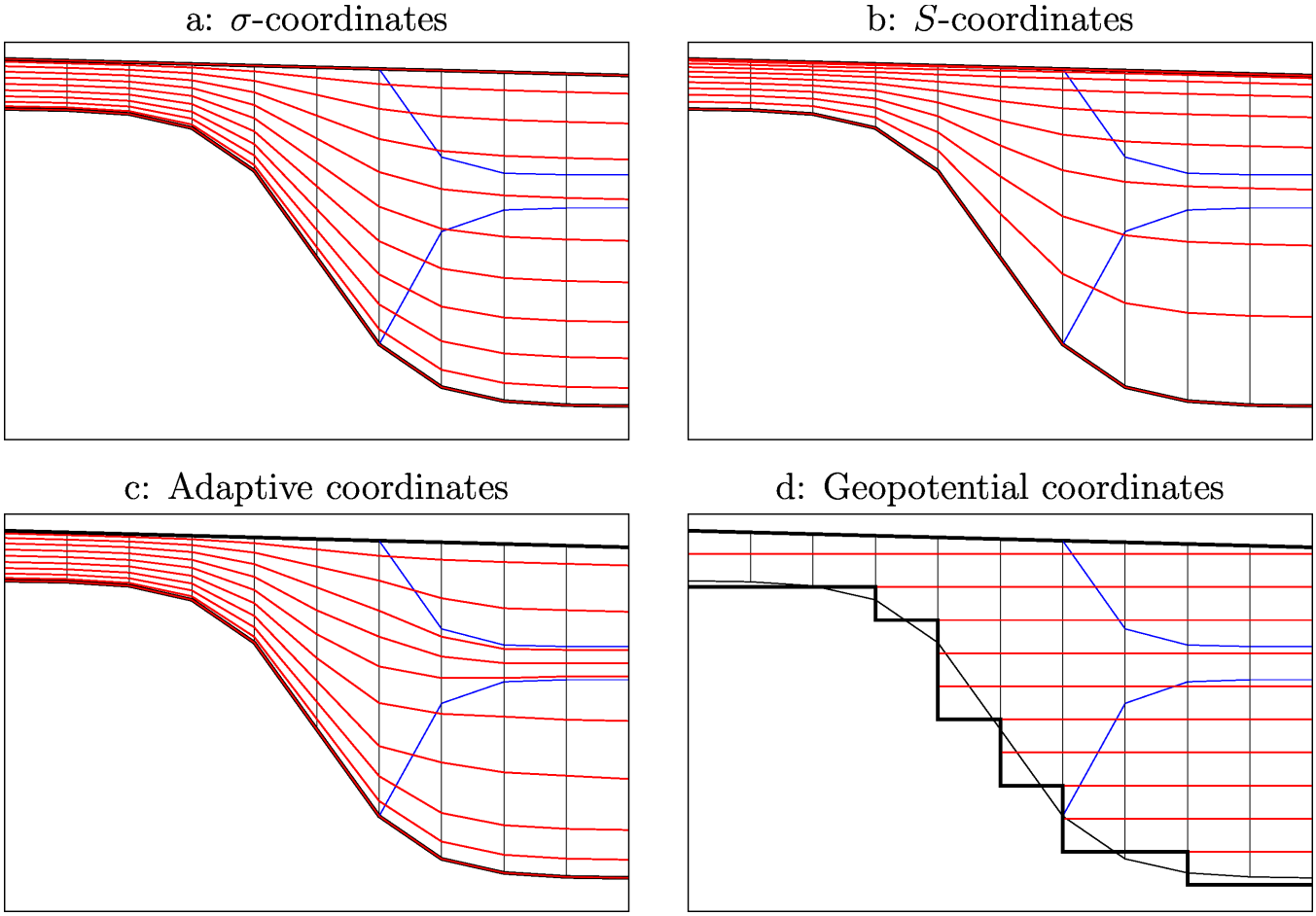

Fig. 2. Sketch showing a vertical transect through a coastal ocean model domain including four different vertical coordinates. The blue lines indicate two selected isopycnals representing a tidal front with a stratified shelf sea region to the right and a well-mixed coastal region to the left. The vertical lines indicate the horizontal discretisation, the red lines show the vertical coordinate surfaces and the bold black lines show the bottom and surface representation of the coordinates. a: σ-coordinates with zooming towards the surface and the bottom; b: S-coordinates with high near-surface resolution; c: Adaptive coordinates with increased resolution in the stratified region; d: Geopotential coordinates (note that shaved cells would remove the staircase representation of the bottom topography).

Within the layer-integrated temperature and salinity equations (A.4) and (A.5) the turbulent fluxes $J^{[\Theta,\mathrm{S}]}_{[\mathrm{x,y,z}]}$ are based on (3.18). The surface temperature flux is given according to (3.11) by $J^{\Theta}_{\mathrm{z},k_{\max}+1/2} = \frac{Q_s+Q_l+Q_b}{C_p\rho_0}$ and the source term by the divergence of the interfacial irradiance $F^{\Theta}_k = \frac{1}{C_p\rho_0}\frac{I_{k+1/2}-I_{k-1/2}}{h_k}$.

As mentioned in the context of the boundary condition for salt fluxes (3.13), the surface salinity fluxes are zero. In a Lorenz-grid this can be easily achieved by setting $\widetilde{S}_{k_{\max}+1/2} = 0$ and $J^{\mathrm{S}}_{\mathrm{z},k_{\max}+1/2} = 0$.

4.2 Examples for vertical coordinates

The almost arbitrary choice of the transformation function $s = s(x, y, z, t)$ or equivalently of the moving layer interfaces $z_{k+1/2}\,(x, y, t)$ allows for a high degree of freedom for the vertical layout which can be exploited to improve the model performance.

4.2.1 Geopotential coordinates

Geopotential (or z-) coordinates (see Figure 2d) are based on globally defined z-levels $z_{k+1/2}$ which do not depend on location or time, except for the uppermost coordinate level $z_{k_{\max}+1/2} = \eta$ which is identical to the free surface. Vertical resolution is typically increased near the surface to properly reproduce the dynamics of the surface mixed layer. Since for too fine near-surface vertical resolution the moving and sloping free surface might intersect with one or more coordinate levels, the fixed geopotential coordinate level $z_{k_{\max}-1/2}$ must be chosen such that it is below the minimum surface elevation. For models of shelf seas with a large maximum tidal range (see Sec. 2.2) this would result in a large mean thickness of the upper layer of $\mathcal{O}(10\mathrm{m})$, such that near-surface processes are not well-resolved (see, e.g., Mathis et al. (2015)). For simulations of shallow coastal regions including drying and flooding this would mean that all areas with intertidal flats are not vertically resolved. One solution to this problem has been proposed by Casulli and Cheng (1992) and Burchard and Baumert (1998): Layers at the surface are locally added or removed when the surface layer becomes too thick or too thin, respectively. This problem can also be solved by applying so-called z^*-coordinates (Adcroft and Campin (2004)), where geopotential coordinates are obtained for $\eta = 0$ everywhere, and all layer thicknesses are then locally multiplied by $(\eta + H)/H$, such that the layers are squeezed or expanded with the changing water depth. Another advantage of these surface-following coordinates is a reduced vertical transport across the moving layer interfaces and thus significantly reduced numerical mixing caused by advection schemes (see Sections 4.2.3 and 7.5.2). In particular near the surface the tidal elevation triggers a large oscillating vertical velocity relative to the fixed z-coordinate levels which generates strong numerical mixing.

At the bottom geopotential layers will be intersecting with the sloping bottom. This leads to a stair-case type of discretisation of bottom slopes which leads to low accuracy in resolving bottom parallel currents such as dense bottom currents (Ezer and Mellor, 2004). A partial solution to this problem has been proposed by Beckmann and Döscher (1997) by coupling an empirical terrain-following bottom boundary layer model to the geopotential model grid, allowing for bottom-parallel down-slope flow. Another approach to improve representation of along-bottom flow has been proposed by Adcroft et al. (1997): to introduce partial steps and shaved cells at the bottom to better fit the bottom topography. Geopotential coordinates over sloping topography have one other inherent problem: practically they do not allow a high vertical resolution near the bottom. A resolution of the bottom layer of 1 m would require equidistant geopotential coordinates over the entire water column, which is often computationally not affordable.

Given all these disadvantages of geopotential coordinates they can generally not be recommended for coastal ocean simulations. There is however one potential problem of vertical coordinates which is not relevant for geopotential coordinates: the internal pressure gradient problem, see Sec. 7.2. Furthermore, in strongly stratified systems isopycnal surfaces can align well with geopotential levels, and in this case diapycnal mixing is not artificially increased by any along-layer mixing. Therefore, models with geopotential coordinates are still applied for problems with strong stratification such as the Baltic Sea, see e.g. Hordoir et al. (2015).

The numerical treatment of geopotential coordinates fits into the concept of general vertical coordinates by formally allowing layers of zero thickness at the bottom and, in the case of removable surface layers, also at the surface.

4.2.2 *Terrain-following coordinates*

A transformation function of the form

$$z(x, y, s, t) - \eta = S(x, y, s, t)D \tag{4.6}$$

with the local water depth $D = \eta + H$, the stretching function S being strictly monotone in s, $S\left(s_{1/2}\right) = -1$ and $S\left(s_{k_{\max}+1/2}\right) = 0$ generates terrain-following coordinates with $z_{1/2} = -H$ and $z_{k_{\max}+1/2} = \eta$. In addition to the free surface being a coordinate surface (as for the z^*-coordinates), also the bottom is a coordinate surface. Thus, in every watercolumn $k_{\max}$ layers are active and masking of layers is not necessary. A classical option for coastal ocean model simulations are σ-coordinates defined by $S = s = \sigma$ (Nihoul et al. (1986); Blumberg and Mellor (1987)), see Figure 2a. They result in layer thicknesses proportional only to the local water depth, which is a disadvantage especially in deeper waters (where layers may become too thick and thus resolution in critical parts of the water column too coarse) or above steep bottom slopes (where coordinate slopes are relatively steep throughout the water column, see Deleersnijder and Beckers (1992)). One other problem of terrain-following coordinates is the intersection of sloping coordinate surfaces with isopycnals. For the calculation of the internal pressure gradient, this results in a balance of two large terms which typically results in large truncation errors and thus artificial currents (see Sec. 7.2 for a detailed discussion).

Some of these problems can be reduced by using non-equidistant σ-levels $\sigma_{k+1/2}$ (equivalent to non-linear stretching functions $S(s)$) and modified stretching functions $S(x, y, s)$ that rescale the near-surface layer heights proportional to a fixed critical water depth instead of to the local water depth (Song and Haidvogel, 1994; Shchepetkin and McWilliams, 2009b), see Figure 2b.

An alternative transformation function that maintains high resolution at the surface or at the bottom independently of the local water depth has been developed by Burchard and Petersen (1997) and Burchard and Bolding (2002).

In order to obtain higher accuracy, hybridisations between s- and z-coordinates have been proposed, leading to less steep coordinate slopes than for s coordinates and smaller bottom steps than for z-coordinates, see Gerdes (1993), Burchard and Petersen (1997), Dukhovskoy et al. (2009) or O'Dea et al. (2012) for details.

4.2.3 *Arbitrary Lagrangian-Eulerian (ALE) coordinates*

For geopotential and terrain-following coordinates the transformation function $z(s)$ is explicitly prescribed. The temporal evolution of the corresponding interface positions $z_{k+1/2}(x, y, t)$ and layer heights $h_k(x, y, t)$ is fully determined by a prognostic equation for the sea surface elevation $\eta(x, y, t)$ (see Sec. 5.1). In this case the continuity equation (A.1) does not serve as a prognostic equation for h_k, but as a diagnostic equation for the grid-related vertical velocity $w^{\mathrm{s}}_{k+1/2}$. Following Adcroft and Hallberg (2006), this is the Eulerian treatment of the vertical direction (EVD).

In contrast, the Lagrangian treatment of the vertical direction (LVD) is based on a Lagrangian vertical coordinate, formally defined by $\frac{\mathrm{D}s}{\mathrm{D}t} = 0$ (Starr, 1945). In this case the grid-related vertical velocity vanishes $w^{\mathrm{s}} = 0$, see (4.1), and the continuity equation (A.1) serves as a prognostic equation for the layer heights h_k. Numerical mixing (induced by truncation errors of discrete advective fluxes; see Section 7.5.2) is significantly reduced in Lagrangian vertical coordinates because of the missing advective transport through the coordinate surfaces. However, a pure Lagrangian movement of the layers is prone to grid distortion and possibly vanishing layers, which complicates the numerical treatment.

Therefore, a combination of LVD and EVD gains increasingly popularity. Originally Hirt et al. (1974) defined the Arbitrary Lagrangian-Eulerian (ALE) method by a Lagrangian mesh movement (LVD step) followed by an optional readjustment of the mesh associated with grid-related advective transports (EVD step). The advection during the EVD step can be replaced by instantaneous "remapping" (monotone and conservative interpolation, see e.g. White and Adcroft, 2008) which relaxes the strict CFL constraint to a less severe Lipschitz type criteria of the form $\Delta t \max|\nabla \boldsymbol{u}| < 1$.

Another approach is to consider Lagrangian tendencies in the calculation of the layer heights used in EVD algorithms. As the treatment of the full motion in a Lagrangian way is prone to grid distortion, only particular contributions are considered. Separable terrain-following coordinates of the form $z - \eta = S(s)D(x, y, t)$ inherently imply a Lagrangian treatment of merely barotropic motions (Shchepetkin and McWilliams, 2009b). Non-separable terrain-following coordinates with time-independent stretching functions $S(x, y, s)$ do not exactly treat barotropic motions in a Lagrangian way, but also significantly reduce the corresponding grid-related vertical transports by scaling the layer heights according to $h_k = \frac{D}{H} h_k^{(\eta=0)}$. The same holds for the z^*-coordinates of Adcroft and Campin (2004), see Section 4.2.1. Recently, Leclair and Madec (2011) proposed to also treat fast oscillating baroclinic currents in a Lagrangian way by introducing the so-called $\tilde{z}$-coordinate.

4.2.4 Adaptive coordinates

In order to further optimise the vertical grid layout in 3D models, Hofmeister et al. (2010) presented adaptive coordinates, see Figure 2c. These do not only consider Lagrangian tendencies, but also a zooming of layers towards boundaries, stratification and shear. This zooming is based on a vertical diffusion equation for the interface positions,

$$\partial_t z_{k+1/2} - \left(D^{\mathrm{grid}}_{k+1}(z_{k+3/2} - z_{k+1/2}) - D^{\mathrm{grid}}_{k}(z_{k+1/2} - z_{k-1/2}) \right) = 0, \tag{4.7}$$

with boundary conditions $z_{1/2} = -H$ and $z_{k_{\max}+1/2} = \eta$ (Burchard and Beckers, 2004). A vertically constant layer "diffusion" coefficient D^{grid} (unit s^{-1}) tends to generate equidistant layers, whereas locally increased coefficients (e.g. proportional to stratification and shear) increase the local concentration of layer interfaces and thus the vertical resolution. Improved vertical resolution decreases the truncation errors of vertical advective fluxes and thus reduces vertical numerical mixing. The layer distribution in adjacent water columns is coupled by lateral adjustment of layer heights and interface positions.

In addition, an optional isopycnal tendency, based on estimating the positions $\hat{z}$ of prescribed target densities $\hat{\rho}$ from a truncated Taylor series $\hat{z} = z + (\hat{\rho} - \rho) / \partial_z \rho$, aligns the layers with isopycnals and thus reduces the spurious diapycnal mixing of tracers due to explicit and numerical along-layer mixing in the model. Furthermore, an isopycnal alignment of the layers reduces internal pressure gradient errors (see Sec. 7.2). It should be noted, that pure isopycnal coordinates are not appropriate for coastal ocean models, because of the relatively large mixed layers according to (2.1).

Gräwe et al. (2015) demonstrated the clear advantages of adaptive coordinates compared to σ-coordinates in a realistic state-of-the-art model application with different dynamical regimes (tidal/non-tidal parts, seasonal thermocline / permanent halocline).

5 Choices for barotropic-baroclinic mode-splitting and drying & flooding

Due to the presence of a free surface, fast surface gravity waves are part of the numerical solution, and in shallow areas of the domain drying and flooding is possible, see (2.2). Both issues require special numerical techniques that will be outlined in the following two subsections.

5.1 Barotropic-baroclinic mode-splitting

Within the EVD-treatment (see Section 4.2.3) the layer-integrated continuity equation (A.1) serves as a diagnostic equation for the grid-related vertical velocities $w^{\mathrm{s}}_{k+1/2}$, and the layer heights h_k are determined in terms of the total water depth D and the free surface elevation η. In this case a prognostic equation for the free surface elevation must be derived from the vertical sum of the layer-integrated continuity equation (A.1) and consideration of the kinematic boundary conditions (3.9a) and (3.9b):

$$\partial_t(\eta + H) = \partial_t D = \partial_t \left(\sum_{k=1}^{k_{\max}} h_k \right) = -\partial_x \left(\sum_{k=1}^{k_{\max}} h_k u_k \right) - \partial_y \left(\sum_{k=1}^{k_{\max}} h_k v_k \right) - (E - P). \qquad (5.1)$$

The direct numerical integration of the set (5.1) and (A.1)–(A.5) is possible. However, the computational costs can be significantly reduced by a barotropic-baroclinic mode-splitting, based on different time-stepping of the barotropic mode associated with fast surface gravity waves, and the remaining baroclinic dynamics. Within an explicit temporal discretisation the time step of the barotropic mode is strongly constrained by the celerity of shallow water surface gravity waves (Beckers and Deleersnijder, 1993), whereas the much slower baroclinic motions can be integrated with an $\mathcal{O}(10^1)$ times larger time step. Therefore, a split-explicit mode-splitting (see e.g. Simons, 1974, and Section 5.1.2) is based on the prognostic integration of the barotropic mode by a series of smaller time steps carried out during one baroclinic time step. Alternatively, a (formal) split-implicit mode-splitting (see e.g. Madala and Piacsek, 1977, and Section 5.1.1) avoids the explicit time step constraint due the fast surface gravity waves by treating the transports in (5.1), and the surface slopes in (A.2) and (A.3) implicitly. Both methods have their own merits and complications, which will be outlined in the following Sections. An excellent comparison can also be found in Section 4 of Griffies et al. (2000).

5.1.1 Split-implicit mode-splitting

Following the θ-scheme of Casulli and Cattani (1994) the set (5.1), (A.2) and (A.3) can be solved simultaneously, with the transports in (5.1) being temporally weighted such that they are between the levels of the old and the new surface elevation, and equivalently, with η in (A.2) and (A.3) being temporally between the old and new transports. Insertion of (A.2) and (A.3) into (5.1) then gives an elliptic system for the new surface elevation with a matrix of dimension $N \times N$ with N denoting the number of free-surface grid boxes. Depending on the treatment of the Coriolis terms (explicit or implicit), each row of the matrix has 5 or 9 non-zero entries, such that the matrix is very sparse. One of the challenges for solving these large systems of equations is to find accurate (typically iterative) solvers which are efficient also on massively parallel high-performance computers. An early example for a semi-implicit coastal ocean model including semi-implicit treatment of the Coriolis term has been presented by Backhaus (1985).

To avoid the requirement of solving one large elliptic system, a directional-split method had been introduced by Peaceman and Rachford (1955), in which in an alternating manner the equations are solved along

one and then along the other coordinate direction implicitly. This method is called Alternating Directions Implicit (ADI). Many models in coastal engineering had adopted this approach (see, e.g., Pietrzak et al., 2002). While ADI is easier to handle computationally, additional errors due to the directional splitting have to be considered.

The advantage of the (formal) split-implicit mode-splitting is the relatively easy coupling between the modes, since both are computed with the same time step. In case of ADI, the baroclinic equations (A.1), (A.4), (A.5) and other tracer equations must be stepped forward consistent to the directional-split stepping of (5.1). A disadvantage of implicit schemes is the demanding computation of large and sparse linear system on parallel computers. While the scheme with $\theta = 0.5$ is energy-conserving (but still sensitive to instabilities arising from the discretisation of other terms), a larger degree of implicitness ($\theta \to 1$) stabilises the scheme, a procedure which however for larger time steps becomes too dissipative and thus artificially reduces the free surface variability (Walters et al., 2009). In tidal or tsunami simulations this sets a practical limitation to the overall model time step. In addition, the dispersion errors increase with the model time step of a semi-implicit formulation and this also imposes an accuracy constraint on the value of the model time step.

5.1.2 Split-explicit mode-splitting

In order to prognostically integrate the barotropic mode in a series of smaller time steps constrained by the celerity of shallow water surface gravity waves, an additional set of equations must be derived. Usually the slightly depth-dependent barotropic mode is approximated by the depth-integrated equations (also called external mode), given by (5.1) and the vertical sum of the layer-integrated momentum equations (A.2) and (A.3):

$$\partial_t \eta + \partial_x \left(D\bar{u}\right) + \partial_y \left(D\bar{v}\right) = -(E - P), \tag{5.2a}$$

$$\begin{aligned}\partial_t \left(D\bar{u}\right) + \partial_x \left(D\bar{u}\bar{u}\right) + \partial_y \left(D\bar{v}\bar{u}\right) \\ = D\widetilde{F}^{\mathrm{h}}_{\mathrm{x}}(D,\bar{u},\bar{v}) + \tau^{\mathrm{s}}_{\mathrm{x}}(\bar{u},\bar{v}) - \tau^{\mathrm{b}}_{\mathrm{x}}(D,\bar{u},\bar{v}) + fD\bar{v} - gD\partial_x\eta - D\tfrac{1}{\rho_0}\partial_x p_a + S_{\mathrm{x}},\end{aligned} \tag{5.2b}$$

$$\begin{aligned}\partial_t \left(D\bar{v}\right) + \partial_x \left(D\bar{u}\bar{v}\right) + \partial_y \left(D\bar{v}\bar{v}\right) \\ = D\widetilde{F}^{\mathrm{h}}_{\mathrm{y}}(D,\bar{u},\bar{v}) + \tau^{\mathrm{s}}_{\mathrm{y}}(\bar{u},\bar{v}) - \tau^{\mathrm{b}}_{\mathrm{y}}(D,\bar{u},\bar{v}) - fD\bar{u} - gD\partial_y\eta - D\tfrac{1}{\rho_0}\partial_y p_a + S_{\mathrm{y}},\end{aligned} \tag{5.2c}$$

with the water depth,

$$D \equiv \sum_{k=1}^{k_{\max}} h_k, \tag{5.3}$$

the barotropic transports,

$$[D\bar{u}, D\bar{v}] \equiv \sum_{k=1}^{k_{\max}} [h_k u_k, h_k v_k], \tag{5.4}$$

and the barotropic-baroclinic interaction terms:

$$
\begin{aligned}
S_{[\mathrm{x,y}]} = \quad & \partial_x \left(D\bar{u}[\bar{u},\bar{v}] \right) && - \sum_{k=1}^{k_{\max}} \partial_x \left(h_k u_k[u_k, v_k] \right) \\
& + \partial_y \left(D\bar{u}[\bar{u},\bar{v}] \right) && - \sum_{k=1}^{k_{\max}} \partial_y \left(h_k u_k[u_k, v_k] \right) \\
& - D\widetilde{F}^{\mathrm{h}}_{[\mathrm{x,y}]}(D,\bar{u},\bar{v}) && + \sum_{k=1}^{k_{\max}} h_k \widetilde{F}^{\mathrm{h}}_{[\mathrm{x,y}]}(h_k, u_k, v_k) \\
& - \tau^{\mathrm{s}}_{[\mathrm{x,y}]}(\bar{u},\bar{v}) && + \tau^{\mathrm{s}}_{[\mathrm{x,y}]}(u_{k_{\max}}, v_{k_{\max}}) \\
& + \tau^{\mathrm{b}}_{[\mathrm{x,y}]}(D,\bar{u},\bar{v}) && - \tau^{\mathrm{b}}_{[\mathrm{x,y}]}(h_1, u_1, v_1) \\
& && + \sum_{k=1}^{k_{\max}} h_k F^{\mathrm{IPG}}_{[\mathrm{x,y}],k}.
\end{aligned} \tag{5.5}
$$

The remaining 3D equations (A.1)–(A.5), as well as the turbulence closure equations (section 3.2) and other tracer equations such as biogeochemical model equations represent the internal (baroclinic) mode. With (5.3), (5.4) and (5.5) the splitting into external and internal mode equations is exact. But, as mentioned above, it does not exactly separate the slightly depth-dependent fast barotropic dynamics from the slow baroclinic ones. Therefore, the time-stepping of the internal mode might still be constrained by some fast dynamics. Besides that, since the surface elevation and the barotropic transports are provided by the external mode, an explicit temporal discretisation of the internal mode is not constrained by the celerity of the fastest surface gravity waves anymore.

In order to provide a reasonable free surface elevation and barotropic transports for updating the internal mode from stage ^{n} to stage $^{n+1}$, the external mode is integrated explicitly within a subcycle of $M_{\max}$ time steps from stage ^{n,0} to stage $^{n,M_{\max}}$. The timestep of the external mode is $\triangle t_{2\mathrm{D}}$, whereas the internal mode is integrated with a larger internal timestep $\triangle t_{3\mathrm{D}} = M \triangle t_{2\mathrm{D}}$ with $M \leq M_{\max}$.

It is easy and accurate to discretise the external mode (5.2a)–(5.2c) with an explicit-in-time solver. In the following a time-staggered two-level scheme is outlined. Staggering in time between the surface elevations and the barotropic transports would still guarantee second-order in time accuracy. This would be achieved by subsequently calculating the surface elevation and the barotropic transports with using the newly updated transports and elevations on the right hand sides (except for the barotropic-baroclinic interaction terms; see below). In the following the focus will be on volume and tracer mass conservation. Therefore, the discretisation of the momentum equations will be not presented in detail. A time-staggered discretisation of the free-surface equation (5.2a) is given by:

$$
\begin{aligned}
& \frac{\eta^{n,m+1} - \eta^{n,m}}{\triangle t_{2\mathrm{D}}} + \partial_x \left(D\bar{u} \right)^{n,m+1/2} + \partial_y \left(D\bar{v} \right)^{n,m+1/2} \\
& \qquad = - \left(E - P \right)^{n,m+1/2}
\end{aligned} \tag{5.6}
$$

Following Shchepetkin and McWilliams (2005) a filtered surface elevation is provided to the internal mode,

$$
\langle \eta \rangle^{n+1} \equiv \sum_{m=0}^{M_{\max}} a_m \eta^{n,m}, \tag{5.7}
$$

with normalised filter weights $\sum_{m=0}^{M_{\max}} a_m = 1$. If the initial surface elevation of each external mode cycle

is reset to $\eta^{n,0} \equiv \langle\eta\rangle^n$, the compatible surface elevation equation resolved by the internal mode can be derived from (5.6) as

$$\frac{\langle\eta\rangle^{n+1} - \langle\eta\rangle^n}{\triangle t_{3D}} + \partial_x \langle\langle D\bar{u}\rangle\rangle^{n+1/2} + \partial_y \langle\langle D\bar{v}\rangle\rangle^{n+1/2} = -\langle\langle E - P\rangle\rangle^{n+1/2} \quad (5.8)$$

with

$$\langle\langle\psi\rangle\rangle^{n+1/2} \equiv \sum_{m=0}^{M_{\max}-1} b_m \psi^{n,m+1/2} \quad (5.9)$$

and $b_m \equiv \frac{1}{M}\sum_{m'=m+1}^{M_{\max}} a_{m'}$. The general filter applied in (5.7) offers different types of filtering. Deleersnijder (1993) proposed to provide the instantaneous surface elevation $\langle\eta\rangle^{n+1} = \eta^{n,M}$ and averaged barotropic transports $\langle\langle[D\bar{u}, D\bar{v}]\rangle\rangle^{n+1/2} = \frac{1}{M}\sum_{m=0}^{M-1}[D\bar{u}, D\bar{v}]^{n,m+1/2}$ to the internal mode. This treatment corresponds to $M_{\max} = M$, $a_m = \delta_{mM}$, $b_m = \frac{1}{M}$ and involves no reset of the external quantities, i.e. $\eta^{n+1,0} = \eta^{n,M}$ and $[D\bar{u}, D\bar{v}]^{n+1,0-1/2} = [D\bar{u}, D\bar{v}]^{n,M-1/2}$. In order to stabilise the retained fast dynamics within the internal mode and to prevent aliasing errors Griffies (2007) suggested to provide an averaged surface elevation $\langle\eta\rangle^{n+1} = \frac{1}{2M+1}\sum_{m=0}^{2M}\eta^{n,m}$ to the internal mode, obtained by $M_{\max} = 2M$, $a_m = \frac{1}{2M+1}$ and $b_m = \frac{2M-m}{M(2M+1)}$. Non-uniform filter weights, centered around $m = M < M_{\max}$, were presented by Shchepetkin and McWilliams (2005) to offer more frequency-selective filtering.

Volume conservation requires that the layer-integrated continuity equation (A.1) in the internal mode,

$$\frac{h_k^{n+1} - h_k^n}{\triangle t_{3D}} + \partial_x (h_k u_k)^{n+1/2} + \partial_y (h_k v_k)^{n+1/2} + \left(w_{k+1/2}^{s,n+1/2} - w_{k-1/2}^{s,n+1/2}\right) = 0, \quad (5.10)$$

recovers (5.8) when vertically summed. Thus

$$\sum_{k=1}^{k_{\max}} h_k^{n+1} \equiv \langle\eta\rangle^{n+1} + \langle H\rangle^{n+1} = \langle D\rangle^{n+1}, \quad (5.11a)$$

$$\sum_{k=1}^{k_{\max}} [h_k u_k, h_k v_k]^{n+1/2} \equiv \langle\langle[D\bar{u}, D\bar{v}]\rangle\rangle^{n+1/2}, \quad (5.11b)$$

$$w_{k_{\max}+1/2}^{s,n+1/2} \equiv \langle\langle E - P\rangle\rangle^{n+1/2}. \quad (5.11c)$$

Compatibility condition (5.11b) requires a correction of the velocity profiles $[u_k, v_k]^{n+1/2,*}$ obtained from the baroclinic momentum equations (A.2) and (A.3). In order to preserve the vertical shear of the original velocity profiles, the final profiles $[u_k, v_k]^{n+1/2}$ can be obtained by shifting the original ones:

$$[u_k, v_k]^{n+1/2} = [u_k, v_k]^{n+1/2,*} + \left(\langle\langle[D\bar{u}, D\bar{v}]\rangle\rangle^{n+1/2} - \sum_{k=1}^{k_{\max}} [h_k u_k, h_k v_k]^{n+1/2,*}\right) / \langle D\rangle^{n+1/2}. \quad (5.12)$$

It should be noted again, that for tracer mass conservation the discrete tracer equations must recover (5.10) for constant tracer concentrations. Therefore, the shifting of velocity profiles must be done before the grid-related vertical velocity is diagnosed from (5.10) and the tracer equations are integrated. At the end of each internal timestep, the interaction-terms (5.5) can be updated in terms of $\langle\langle[D\bar{u}, D\bar{v}]\rangle\rangle^{n+1/2}$,

$[h_k u_k, h_k v_k]^{n+1/2}$ and $F^{\mathrm{IPG},n+1}_{[\mathrm{x,y}],k}$. Since these interaction-terms are held constant over the next external subcycle, integrating the barotropic transports from $[D\bar{u}, D\bar{v}]^{n+1,0-1/2}$ to $[D\bar{u}, D\bar{v}]^{n+1,M_{\max}-1/2}$, a time lag is introduced. It should be noted that the barotropic-baroclinic interaction terms provide a correction to the corresponding temporally-resolved barotropic terms in (5.2b) and (5.2c). Thus, the barotropic terms updated during the external subcycle only provide a tendency, whereas the interaction terms consider the more accurate estimates based on the vertically resolved quantities from the last internal time stage. Due to the strong non-linearity (see Section 2.2) and fast response time (see Section 2.4) of the coastal ocean, in particular the advection and drag terms in (5.2b) and (5.2c) are not kept constant (in contrast to many large-scale ocean models).

5.2 Drying & flooding

In many coastal areas intertidal flats are an important topographic feature. During high water those areas are inundated and during ebb tide they may fall dry, approaching zero water depth $D \to 0$, but never becoming negative. To understand how this is reflected in the mathematical formulations for coastal ocean dynamics, it is instructive to reformulate the depth-integrated continuity equation (5.2a):

$$\partial_t D + \bar{u}\partial_x D + \bar{v}\partial_y D = -\left(\partial_x \bar{u} + \partial_y \bar{v}\right) D - (E - P). \tag{5.13}$$

The form (5.13) demonstrates positivity of the water depth, because its total derivative depends on a sink term which vanishes for decaying water depth. The divergence stays bounded, because for frictionally dominated regimes the depth-integrated momentum equations (5.2b) and (5.2c), and the quadratic bed friction (7.15) guarantee bounded depth-mean velocities. The evaporation E which reduces the water depth also vanishes for vanishing water depth.

Various ways have been proposed in coastal ocean models to guarantee the two major properties (i) volume conservation (for incompressible flow) according to (5.2a) and (ii) positivity according to (5.13), also numerically.

Volume conservation can easily be achieved by a Finite-Volume discretisation of (5.2a). Positivity of the water depth requires some more care. Since any direct manipulation (e.g. clipping) of the water depth violates volume and tracer conservation, in most coastal ocean models the barotropic transports in (5.2a) are modified in a physical sound and reasonable way instead. For a semi-implicit barotropic model Stelling and Duinmeijer (2003) suggested to treat (5.2a) as an advection equation for the water depth and to approximate D at the interfaces of a water column according to positive-definite advection schemes. However, in an explicit discretisation as (5.6) this treatment seems to be inconsistent, as the barotropic transports are already known.

Therefore various approaches have been developed, all of them leaving a thin film of water in dry water columns, where the dynamics is manipulated in some way to avoid further drying towards zero or negative water depth. Of course any manipulation to the barotropic momentum equations must also be considered in the baroclinic ones in order to guarantee consistency of the barotropic and baroclinic transports. In early coastal ocean models (Flather and Heaps, 1975; Backhaus, 1976, 1985; Jungclaus and Backhaus, 1994), a number of rules were defined on how to reduce fluxes out of a water column when the application of these fluxes would lead to negative water depth (or the undercut of a prescribed minimum water depth). Also the drying & flooding schemes of Oey (2005) and Warner et al. (2013) are based on this principle. The method works reliably, but it has to be taken into account that reduction or shut-off of fluxes around one water column would change the net fluxes into the neighboring columns, such that an iterative procedure

might become necessary. This problem has been partially solved by Warner et al. (2013), by shutting off transports around a water column when the water depth at the old time step is below the critical depth, see also Defne and Ganju (2015) who simulated a large lagoonal back-barrier estuary at the US east coast including extensive intertidal flats. Moreover, the direct correction of fluxes might in some models lead to spatially and temporally oscillating patterns of dry and wet water columns. Furthermore, shutting on and off transports instantaneously could lead to complications in turbulence closure models, since the bed stress which largely determines the eddy viscosity profiles (via the turbulent kinetic energy and the macro length scale of turbulence, see section 3.2.1) would be suddenly switched on or shut off regularly.

In some models (e.g., Casulli and Cattani, 1994) the water depth at the transport points of a C-grid is chosen as the minimum depth between the adjacent pressure points, with the consequence that velocities feel the shallow water and bed friction strongly reduces the volume transport. This however might lead to significantly delayed drying and flooding processes (Burchard and Bolding, 2002).

In order to avoid explicit switching on or off of transports in drying water columns, Burchard et al. (2004) (see also Burchard and Bolding, 2002) proposed the following measures when calculating the layer-integrated momentum equations:

- A critical water depth D_{crit}, and a minimum water depth, $D_{\min}$ are defined with $D_{\text{crit}} > D_{\min}$ (see fig. 3). Typical values would be $D_{\text{crit}} = 0.2\,\text{m}$ and $D_{\min} = 0.05\,\text{m}$. To simplify the dynamics in very shallow water with $D < D_{\text{crit}}$, many terms in the momentum equations are reduced by a factor linearly decreasing between 1 (for $D = D_{\text{crit}}$) and 0 (for $D = D_{\min}$), which basically reduces the local dynamics to an external pressure gradient - friction balance. Such a balance supports reduction of local transports, since the friction coefficient calculated from the law of the wall increases towards infinity for the water depth converging towards zero, see equation (7.15).
- Additionally, when the surface elevation in one water column is below the bottom coordinate plus the minimum depth in any adjacent column (which often happens at steep bathymetry in shallow water and relatively coarse horizontal resolution, see fig. 3, where $\eta_{i+1,j} < -H_{i,j} + D_{\min}$), a virtual surface elevation is defined from which the external pressure gradient ($\partial_x\eta, \partial_y\eta$) is calculated. In that case, $\tilde{\eta}_{i+1,j} = \max\{\eta_{i+1,j}, -H_{i,j} + D_{\min}\}$, and the surface elevation gradient is calculated as $(\tilde{\eta}_{i+1,j} - \eta_{i,j})/\Delta x$. In the extreme case shown in fig. 3 water volume would actually flow against the elevation gradient, because $\eta_{i,j} < -H_{i,j} + D_{\min}$.
- Despite the above measures, direct reduction or shut-off of transports surrounding a water column may still be necessary at singular locations. To stabilise the drying and flooding algorithm, increasing the minimum and critical water depth is often a preferred option.

Using these algorithms Gräwe et al. (2016) could carry out a stable and multi-annual simulation of the entire Wadden Sea of the South-Eastern North Sea at a horizontal resolution of 200 m.

6 Treatment of open boundary conditions and model nesting

Coastal ocean models focus on limited areas of interest and thus data are needed to force the models at open boundaries, see Section 2.5. The data can typically come from an external source (e.g. climatology, coarser resolution run on a wider domain) following a one-way (coarse $\rightarrow$ fine) approach. In comparison, in a two-way approach, the external data (a numerical model) feel the local coastal solution through a feed-back term. Local and external models generally differ on several key points among them grid resolution (in space and time) and physics. Across the interface, inflow and outflow can occur. In the case of inflow

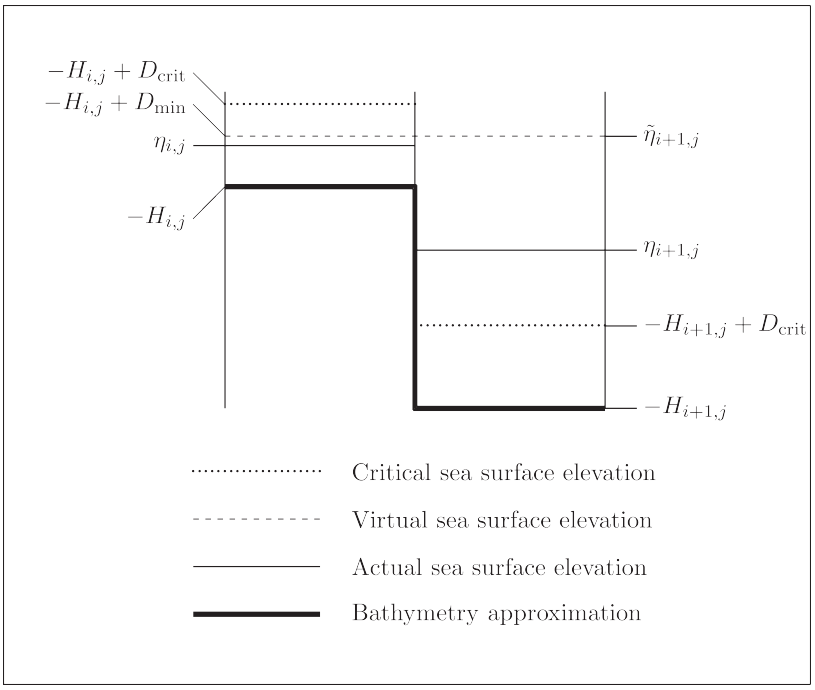

Fig. 3. Sketch explaining the geometry of bathymetry and surface elevation approximations for drying and flooding measures. This figure has been modified from Burchard et al. (2004).

conditions, the quality of the local solution is strongly dependent on the quality of external data while in the case of outflow, the main issue is to prevent wave reflection at the interface. A two-way approach helps in maintaining some consistency between local and external solutions, at least when the physics of the two models are close. In both one-way and two-way approaches, the design of the boundary conditions must be carefully done. Due to the complexity of the physics, the scale heterogeneity in space and time, ideal boundary conditions are not achievable and a reasonable choice relies on a compromise between accuracy and robustness. Section 6.1 briefly introduces the general framework. Section 6.2 treats the problem of model forcing in a one-way approach (open boundary conditions). Section 6.3 introduces two-way approaches.

6.1 General framework

We consider a domain Ω_{loc} embedded in a domain Ω_{ext} as shown in Figure 4. The local and external solutions, ϕ_{loc} and ϕ_{ext}, are integrated according to

$$\partial_t \phi_{\text{loc}} + L_{\text{loc}}(\phi_{\text{loc}}) = f_{\text{loc}} \text{ in } \Omega_{\text{loc}}, \quad \partial_t \phi_{\text{ext}} + L_{\text{ext}}(\phi_{\text{ext}}) = f_{\text{ext}} \text{ in } \Omega_{\text{ext}}.$$

L_{loc} and L_{ext} are spatial differential operators, f_{loc} and f_{ext} model forcings. ϕ is the vector of prognostic state variables. The models interact through a transition area Γ that, depending on the boundary conditions, may be restricted to a single interface γ.
Let Δx_{loc} and Δx_{ext} (resp. Δt_{loc} and Δt_{ext})) be the grid (resp. time) steps on Ω_{loc} and Ω_{ext}. Today, the availability of global/regional operational or reanalysis products allows to consider the case where typical values of time/grid steps obey:

$$\frac{\Delta x_{\text{ext}}}{\Delta x_{\text{loc}}} \approx \frac{\Delta t_{\text{ext}}}{\Delta t_{\text{loc}}} \approx 2 - 10.$$

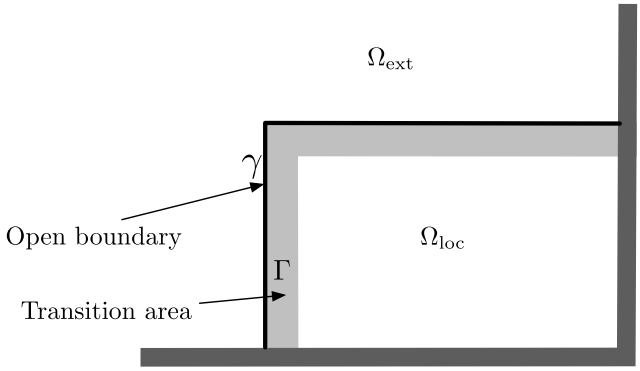

Fig. 4. The local domain Ω_{loc} embedded in the exterior domain Ω_{ext}. Ω_{loc} has an artificial interface γ and possibly a transition area Γ on which boundary conditions are prescribed.

Note that we won't consider the case where the vertical extent of the local domain does not cover the whole water column. Indeed, vertical parameterizations (see Section 3.2.1), coupling between barotropic and baroclinic modes (see Section 5.1) become cumbersome if only part of the water column is computed on the local grid.

The model interactions across the interface γ and/or within the transition area Γ are described in the next Sections.

6.2 Open boundary conditions (OBC) and one-way interaction

We start with a description of the two main classes of OBC methods: relaxation methods which aim to relax the local solution towards the external solution within the transition area Γ and radiation methods which propagate out the information to prevent waves reflection. Simple radiation methods are appropriate only for a first-order scalar equation, the extension to general hyperbolic systems using a characteristic variables approach is explained in Section 6.2.2. Advanced open boundary conditions like Perfectly Matched Layer (PML) and Absorbing Boundary Conditions (ABC) (see Nataf, 2013) will not be discussed here since their derivations require very simplified problems and they have still to be validated in realistic applications. For a review of open boundary conditions, the reader is referred to Palma and Matano (2000); Blayo and Debreu (2005).

The open boundary conditions presented in the next paragraphs can also be used for one-way nested models (i.e. when the external data comes from a coarse resolution run). One-way nesting may be performed online (both models are running simultaneously) (Penven et al., 2006) or offline (Mason et al., 2010). The key element for a choice between these two approaches is the spatio-temporal variability of the boundary conditions. When this variability is high, online nesting, with high frequency / high resolution exchanges between local and external domains, is more efficient. Indeed storage and performance issues limit the frequency/resolution of the outputs made during the coarse resolution run. However in an offline approach, the obvious advantage is that the area covered by the local (high resolution) domain does not have to be known in advance, i.e. before running the external (coarse resolution) model.

6.2.1 Relaxation and radiation methods

6.2.1.1 Relaxation methods Basic Dirichlet (a.k.a. clamped) boundary conditions do not perform well (except for certain basic equations): this abrupt forcing generates inconsistencies and discontinuities near the interface γ. The flow relaxation scheme (FRS) (Davies, 1976) relaxes the interior solution towards external data in the transition area Γ near the boundary and can be written under the following relaxation (or nudging) form (Martinsen and Engedahl, 1987) (considering ϕ as a scalar variable and omitting the model forcing):

$$\partial_t \phi_{\rm loc} + L_{\rm loc}(\phi_{\rm loc}) = -\frac{1}{\tau}(\phi_{\rm loc} - \phi_{\rm ext}) \quad \text{in } \Omega_{\rm loc}, \tag{6.1}$$

The right hand side of (6.1) is the relaxation term. τ is a relaxation time scale. $\lambda = \dfrac{1}{\tau}$ is a positive function, which decreases away from the lateral boundary γ and vanishes outside of Γ. At the discrete level, the right hand side of (6.1) can be discretized implicitly in time to remove associated stability constraints. It is difficult to prescribe the size of the transition area Γ and the variation of λ within Γ, since they depend on the space and time scales of the phenomena (Kållberg, 1977). Typical profiles of λ are based on quadratically or exponentially decreasing functions of the distance to the boundary γ.

Due to the smallness of the coastal model domain, it may also happen that the large scales of the solution are better reproduced in the external domain $\Omega_{\rm ext}$. It is particularly the case when the external model makes use of data assimilation techniques (reanalysis product or operational forecast). In this situation, there is a potential benefit to relax the large scales of the local solution to the ones computed by the external model while the small scales features are still governed by the coastal model evolution. To this aim, spectral nudging methods (Waldron et al., 1996) can be viewed as a FRS scheme which acts on the whole local domain on specified (large) scales. It can be written under the following form:

$$\partial_t \phi_{\rm loc} + L_{\rm loc}(\phi_{\rm loc}) + \Lambda(\phi_{\rm loc} - \phi_{\rm ext}) = 0 \quad \text{in } \Omega_{\rm loc}, \tag{6.2}$$

where the operator Λ is now a low pass filter acting on the whole $\Omega_{\rm loc}$ domain. The expression of Λ may be based on Fourier transform of $(\phi_{\rm loc}, \phi_{\rm ext})$ (with relaxation coefficients fixed in the Fourier space), on Gaussian correlation kernels and more simply on iterative Laplacian smoothing. When applied to coastal modelling, the nudging term is usually reduced near the coast where the external model may have a coarser representation of the coastline.

Finally, most of the time, the FRS scheme is associated to a sponge layer that damps the small scales near the boundary using increased viscosity/diffusivity ν_Γ:

$$\partial_t \phi_{\rm loc} + L_{\rm loc}(\phi_{\rm loc}) = -\frac{1}{\tau}(\phi_{\rm loc} - \phi_{\rm ext}) + \nu_\Gamma \, \Delta\phi_{\rm loc} \quad \text{in } \Omega_{\rm loc}, \tag{6.3}$$

where Δ is the Laplacian operator.

6.2.1.2 Radiation methods In the case of outflow conditions, the FRS scheme will only behave well (and in particular will prevent waves reflection) when the external data is already an accurate representation of the solution. In other cases, radiation methods can be used to propagate out the disturbances. The basic radiation methods solve the Sommerfeld radiation condition (6.4) at the interface,

$$\partial_t \phi_{\rm loc} + c \, \partial_n \phi_{\rm loc} = 0 \qquad \text{on } \gamma, \tag{6.4}$$

and corresponds to the transport of ϕ through γ at the phase speed projected to the boundary, c (∂_n denotes a derivative perpendicular to and towards the outside of the boundary). Obviously this boundary condition is only exact for a transport equation and when c is known. In practice, c $\left(= -\partial_t \phi_{\text{loc}} \left(\partial_n \phi_{\text{loc}}\right)^{-1}\right)$ is estimated at the discrete level using internal values (Orlanski, 1976), leading to different implementations, including, in two dimensions, variants taking into account tangential derivatives (Raymond and Kuo, 1984). Besides the evaluation of the phase speed c, the relevancy of this type of boundary condition for non-monochromatic and/or dispersive waves is questionable.
The radiation condition is valid only for outflow conditions (e.g. $c > 0$ at an eastern boundary). In other cases, relaxation methods as described in the previous paragraph are more appropriate. Radiation and relaxation methods can be combined to give:

$$\partial_t \phi_{\text{loc}} + c\, \partial_n \phi_{\text{loc}} = -\frac{\phi_{\text{loc}} - \phi_{\text{ext}}}{\tau_\gamma} \qquad \text{on } \gamma. \tag{6.5}$$

where τ_γ, the relaxation time scale, has different values $\tau_{\text{in}}, \tau_{\text{out}}$ according to inflow ($\tau_\gamma = \tau_{\text{in}}$) or outflow ($\tau_\gamma = \tau_{\text{out}}$) conditions (Marchesiello et al., 2001). During inflow conditions c is set to zero and τ_{in} is small leading to a strong relaxation towards external solution. τ_{out} is large but not infinity in order to prevent the internal solution to drift for external data. Note that even if (6.5) is written at the interface γ, it is most of the time associated to a relaxation term active on the whole transition area Γ. For consistency, the boundary value of the relaxation time scale τ defined in (6.1) should be greater than τ_{out}.

6.2.2 Characteristic methods

As mentioned previously, radiation methods are only valid when the temporal evolution of the state variable is governed by a first-order hyperbolic equation. They can be extended to more general cases by looking at the hyperbolic parts of the equations. By definition hyperbolic systems can be decomposed into a series of first-order scalar hyperbolic equations whose solutions are the characteristic variables. The problem is then well posed if the incoming characteristics variable are specified and the outgoing characteristic extrapolated from internal values.
Considering a one-dimensional version of the linearised barotropic equation

$$\partial_t \eta = -H \partial_x \bar{u}, \quad \partial_t \bar{u} = -g \partial_x \eta,$$

the two characteristics are given by

$$w_\pm = \bar{u} \pm \sqrt{\frac{g}{H}}\, \eta$$

and propagate with speeds $c_\pm = \pm\sqrt{gH}$ (i.e. $\partial_t w_\pm + c_\pm \partial_x w_\pm = 0$). At open boundaries, the incoming characteristics are prescribed ($w_{\text{loc}} = w_{\text{ext}}$) and the outgoing characteristic are computed from internal values. The computation of outgoing characteristic variables at the boundary can be based on simple extrapolation techniques or on the application of upwind biased schemes. It is well known (see, e.g., Blayo and Debreu, 2005) that the specification of the incoming characteristics of the barotropic equations is equivalent to the Flather boundary condition (Flather, 1976) (which can also be obtained by a Sommerfeld radiation condition for $\bar{u}$, with $c = \sqrt{gH}$, and a 1D version of the continuity equation). At an eastern boundary where $w_- = \bar{u} - \sqrt{\frac{g}{H}}\, \eta$ must be prescribed, the Flather boundary condition reads

$$\bar{u} = \bar{u}_{\text{ext}} + \sqrt{\frac{g}{H}}\, (\eta - \eta_{\text{ext}}) \tag{6.6}$$

and η is given by another boundary condition (e.g. $\partial_x \eta = 0$).
The use of the full characteristic method gives instead:

$$\bar{u} = \frac{1}{2}\left(w_{+,\mathrm{int}} + w_{-,\mathrm{ext}}\right) = \frac{1}{2}\left(\bar{u}_{\mathrm{ext}} + \bar{u}_{\mathrm{int}}\right) + \frac{1}{2}\sqrt{\frac{g}{H}}\left(\eta_{\mathrm{int}} - \eta_{\mathrm{ext}}\right) \tag{6.7}$$

and

$$\eta = \frac{1}{2}\sqrt{\frac{H}{g}}\left(w_{+,\mathrm{int}} - w_{-,\mathrm{ext}}\right) = \frac{1}{2}\left(\eta_{\mathrm{ext}} + \eta_{\mathrm{int}}\right) + \frac{1}{2}\sqrt{\frac{H}{g}}\left(\bar{u}_{\mathrm{int}} - \bar{u}_{\mathrm{ext}}\right), \tag{6.8}$$

where $w_{+,\mathrm{int}} = \bar{u}_{\mathrm{int}} + \sqrt{\frac{g}{H}}\eta_{\mathrm{int}}$ is computed from internal values. The Flather type boundary condition (6.6), or some of its variants, is used in most of the coastal ocean models where it is assumed that surface gravity waves are indeed dominant for the specification of the boundary conditions. If $\bar{u}_{\mathrm{ext}}$ is not known but only η_{ext} (e.g. tidal conditions), a reduced model (e.g. geostrophic balance) may be used to deduce $\bar{u}_{\mathrm{ext}}$. At the discrete level, the computation (extrapolation) of $\bar{u}_{\mathrm{int}}, \eta_{\mathrm{int}}$ in (6.7) has to be done with care. A stable implementation of (6.7) on a staggered C-grid is described in Mason et al. (2010).

6.2.3 3D models

The 3D primitive equation models support the propagation of internal gravity waves. In an idealized framework, their characteristics can be obtained through a vertical normal mode decomposition. Setting 3D boundary conditions on the original state variables without taking into account these propagations renders the problem ill-posed (Oliger and Sundström, 1978). A remedy can be to add a small vertical viscosity in the hydrostatic balance equations (3.2) (Témam and Tribbia, 2003). Characteristics-based methods can formally be extended to 3D-based on a vertical mode decomposition (Jensen, 1998; Blayo and Debreu, 2005) resulting into a series of shallow water models. However the number of assumptions used in their derivations (in particular the linearisation around a horizontally constant background density field and a constant background state velocity field, typically the barotropic solution) make them difficult to apply in practice. That is why, in 3D primitive equation models, the preceding relaxation/radiation boundary conditions are usually applied on each of the prognostic variables (u, v, Θ, S), with a Flather-like boundary condition for the barotropic part.

6.3 Two-way interaction

We consider now a two-way interaction between the external and local models. The external model feels the local model by a feedback of the local solution. We differentiate between traditional two-way nesting algorithms where the local domain corresponds to a local grid refinement of the external domain and more general two-way coupling algorithms.
We will not detail here the interpolation/update operators between the two models. The reader is referred to Debreu and Blayo (2008) for their design, in particular in terms of scale selectivity and conservation.

6.3.1 Two-way nesting

Two-way nesting algorithms have been reviewed in Debreu and Blayo (2008). In this paragraph, we describe strongly coupled models which eventually can be viewed as a single model with an abrupt change of resolution at the high/coarse resolution grids interface γ.

6.3.1.1 Grid interactions In two-way nesting applications, the feedback from the high to the coarse resolution grid prevents the two solutions to drift. In the limit of equal local and external grid resolutions ($L_{\rm ext} = L_{\rm loc}$) the original solution (without nesting) should be recovered. This implies a strong criterion on the forcing of the local model: the boundary conditions have to act on the difference between external and local solutions. We will call this a consistency condition. Typically, the sponge layer in (6.3) should now be written

$$\partial_t \phi_{\rm loc} + \ldots = \nu_\Gamma \, \Delta(\phi_{\rm loc} - \phi_{\rm ext}) \quad \text{in } \Omega_{\rm loc}, \tag{6.9}$$

and if radiation conditions are used, (6.5) should be replaced by:

$$\partial_t(\phi_{\rm loc} - \phi_{\rm ext}) + c\,\partial_n(\phi_{\rm loc} - \phi_{\rm ext}) = -\frac{\phi_{\rm loc} - \phi_{\rm ext}}{\tau}. \tag{6.10}$$

In a sense, in these equations, the temporal and spatial scales of the external solutions are not assumed to be much larger than those of the local domain so that the simplification occurring in (6.3) and (6.5) cannot be made. Condition (6.10) was used in Perkins et al. (1997).

6.3.1.2 Vertical grids In coastal applications, the capacity to change locally the vertical coordinate systems (see Section 4.2) can become crucial for some applications. Indeed, mesh refinement along coastal areas with very small water depths may require some local adaptation of the parameters of the vertical coordinate systems (parameters of the terrain-following coordinates, number of layers, ...). In that case, vertical remapping has to be applied between coarse and fine grids.

6.3.1.3 Time refinement In traditional applications, horizontal mesh refinement is most of the time coupled with time refinement in order to satisfy stability conditions. If the main stability constraint is given by external gravity waves propagation (cf 5.1), at a velocity of $\sqrt{gH}$, we may expect that, when refining the grid near the coast and so with smaller depths, the time step does not have to be reduced. This is certainly the case for some applications, but generally having the possibility to refine the time steps may become important when the actual time step is constrained by other phenomena (e.g. drying and flooding, advection ...).

6.3.2 Two-way coupling

Less strong local/external coupling may also be of interest, particularly when the space and time refinement factors are large and/or if the models $L_{\rm ext}$ and $L_{\rm loc}$ have different physics. In that case, two-way relaxation methods may also be of interest. The spectral nudging method introduced in Section 6.2.1.1 can be extended to two-way interactions. The smooth semi-prognostic method (Sheng et al., 2005) is an example of such a technique. More generally, grids interactions can be (weakly) incorporated in any assimilation scheme coupling at the same time the assimilation of observations and the grid interactions.

7 Numerical treatment of single terms and processes

This section discusses discrete algorithms that are commonly used for the solution of the governing equations formulated in Sec. 3 and 4. Originally, coastal ocean models were discretised using numerical methods loosely inherited from large scale ocean models, namely second-order in space and Leapfrog-in-time schemes (Blumberg and Mellor, 1987). However, over the years, the numerics of those models have

evolved toward the use of more advanced discretisation techniques, more similar to techniques used in other fields of computational fluid dynamics, in order to accommodate to the specific constraints of coastal applications (see Sec. 2). The diversity of methods in use in coastal models is large so that the discussion can only focus on techniques which are more widely used or are expected to become more widely used. For the sake of simplicity and since the numerical requirements for each process can be rather different, this section considers separately sub-systems of the full system of primitive equations. However, it should not overshadow the fact that a numerical kernel must be designed as a whole, not just as an advection or a wave propagation equation since interferences between numerical methods used for different processes exist; e.g. the numerics for pure gravity waves must be chosen under the constraint to be stable for the Coriolis term (Beckers and Deleersnijder, 1993; Walters et al., 2009), or time-stepping optimized for gravity waves are not always the best for advection and Coriolis, and inversely (e.g Shchepetkin and McWilliams, 2005).

Generally speaking, discretisation techniques in most existing structured-grid oceanic coastal models can be classified as finite volume discretisations. The arrangement on the computational grid is shown in Fig. 1. We now give more details on the specifics of different terms.

7.1 Tracer and momentum advection

In coastal ocean models, tracers must be interpreted in a finite-volume sense, meaning that for a given quantity q the discrete quantity $q_{i,j,k}$ is the average over a control volume $\mathscr{V}_{i,j,k}$ (Fig. 1). As far as momentum advection is concerned, in contrast to large-scale models which generally prefer a vector invariant form for nonlinear advection terms (which facilitates the conservation of quantities like potential vorticity, enstrophy and/or kinetic energy; see e.g. Arakawa and Lamb (1977)), coastal models generally adopt a conservative form inherited from Lilly (1965). Momentum advection terms in Lilly (1965) can be viewed as a finite-volume discretisation provided that proper horizontal metric terms are added. We, thus, consider here a generic advection equation written in a conservative way for a layer-averaged quantity q_k (q can either represent a tracer or horizontal momentum components) according to (4.2) along with the continuity equation (A.1)

$$\begin{aligned} \partial_t(h_k q_k) + \partial_x(h_k u_k q_k) + \partial_y(h_k v_k q_k) + \left(w^{\mathrm{s}}_{k+1/2}\tilde{q}_{k+1/2} - w^{\mathrm{s}}_{k-1/2}\tilde{q}_{k-1/2}\right) = 0, \\ \partial_t h_k + \partial_x(h_k u_k) + \partial_y(h_k v_k) + \left(w^{\mathrm{s}}_{k+1/2} - w^{\mathrm{s}}_{k-1/2}\right) = 0, \end{aligned} \tag{7.1}$$

using the notations introduced in Sec. 4. We retain the continuity equation here to emphasize that the advection equation must be conservative while satisfying a constancy preservation property (i.e. if q is initialised with a constant, it remains so). An overview of the time and space discretisations of (7.1) used in large and mesoscales oceanic models can be found in Griffies et al. (2000) or Lemarié et al. (2015).

7.1.1 Method of lines vs coupled space and time approach

In practice, several strategies to discretize (7.1) coexist in the coastal community. A first choice is to consider simple second-order centered schemes supplemented by an explicit diffusion and a non-dissipative time-stepping algorithm in order to ensure energy consistency of the whole code at a discrete level (Marsaleix et al., 2008). A second choice is to rely exclusively on standard high-order upwind schemes in the horizontal direction and weakly-dispersive centered advection schemes in the vertical (e.g.

fourth-order compact schemes), without any explicit dissipation, combined with a high-order predictor-corrector time-stepping algorithm using a method of lines (e.g. Shchepetkin and McWilliams, 2005). In this case, it is accepted that strong gradients will generate overshoots and undershoots and that there is an uncontrolled sink of kinetic energy and tracer variance in the model caused by dissipative truncation errors. As an alternative to the method of lines, where space and time discretisations are considered separately, a coupled space-time approach [3] could be used for advective terms (e.g. Hundsdorfer and Trompert, 1994; Daru and Tenaud, 2004). This type of approach can be viewed as a conservative semi-Lagrangian approach where the characteristics are tracked in space-time. The resulting schemes are one-step schemes with interfacial fluxes depending on the local Courant number $\boldsymbol{\alpha} = \mathbf{u}\Delta t/(\Delta x, \Delta y, \Delta z)$, with $\mathbf{u}$ the velocity vector. They have the property to be free of computational mode, and to be easily extended to arbitrary high-order of accuracy with minimum stencil (e.g. Daru and Tenaud, 2004). Examples of such schemes are the first-order upwind scheme, the Lax-Wendroff scheme or the QUICKEST scheme which are respectively first, second and third order accurate in space and time. Whatever the strategy used (method of lines or coupled space and time), it is generally preferable to prevent spurious numerical oscillations by imposing non-oscillatory constraints which are computationally demanding but provide a way to ensure nonlinear stability, as described in the next paragraph.

7.1.2 Nonlinear stability and flux correcting/limiting methods

Since non-oscillatory schemes, which are seldom used in large-scale models, are expected to be increasingly used to simulate coastal flows at very high-resolution, we provide comments on this point to highlight the associated delicacies. Numerical methods with an order of accuracy larger than one are prone to numerical oscillations. A nonlinear stability criteria often considered is that the numerical solution must not oscillate without bounds. Using the notion of total variation (TV) as a measure of the overall amount of oscillations, numerical schemes have been constructed to ensure that the total variation is either bounded (TVB) or diminishing (TVD) (Harten, 1983; Shu, 1987). Since TVD schemes necessarily degenerate to first order accuracy near smooth extrema, they are prone to clipping errors manifested by the appearance of a flat plateau in the solution due to an excess of diffusion. To avoid this type of error, a less stringent constraint is the monotonicity-preservation (MP) which relaxes the TVD constraint near extrema (e.g. Suresh and Huynh, 1997; Daru and Tenaud, 2004). Flux correcting/limiting is generally used to impose the TVD, TVB or MP stability conditions (e.g. Durran, 2010). Historically, the flux limiting/correcting methods were derived in a coupled space and time framework using the second-order Lax-Wendroff scheme. They can be easily extended to higher-order accuracy using one-step coupled time-space approach of arbitrary high order (e.g. Daru and Tenaud, 2004). However if a method of lines is used the time and space dimensions are decoupled therefore the constraints on total variation must be imposed both in time and space. For this purpose, a family of Runge-Kutta (RK) schemes satisfying the TVD property has been derived by Shu (1988) and Gottlieb and Shu (1998). Note that a consequence of the TVD, TVB and MP stability constraints is a better control of numerical oscillations hence those constraints could be used not only for momentum advection as a way to limit spurious mixing by reducing the grid Reynolds number (Ilicak et al., 2012), but also for the advection of tracers and layer thickness subject to monotonicity or positivity constraints. There is an abundant literature on the comparison of different flux limiting/correcting strategies, see Mohammadi-Aragh et al. (2015) for a recent study in the oceanic modelling context.

[3] The coupled space and time approach is also known in the literature as flux-form semi-Lagrangian approach, as well as transient interpolation method, or direct space-time discretisation.

7.1.3 Multidimensional aspects and stability constraints

The properties of advection schemes in terms of stability and accuracy are generally studied in 1D. The extension of one-dimensional schemes to multi-dimensions in the context of a method of lines is straightforward since the necessary transverse terms are discretised in a transparent way. If a quasi-Eulerian vertical coordinate is used, the stability constraint in three dimensions reads

$$\alpha^x + \alpha^y + \beta\alpha^z \leq \alpha^\star, \qquad (\alpha^x, \alpha^y, \alpha^z) = \mathbf{u}\Delta t/(\Delta x, \Delta y, \Delta z) \tag{7.2}$$

where $\alpha^\star$ is the CFL stability constraint associated to the numerical schemes used for the time and space, and β a coefficient arising from the fact that different advection schemes with different stability criteria may be used in the horizontal and vertical directions. As far as the coupled space and time approach is concerned, a simple application of the one-dimensional fluxes in each spatial direction would result in a scheme that can be at most first-order accurate, whatever the order of accuracy of the 1D fluxes, and the scheme would be unconditionally unstable. To overcome this issue a directional splitting can be used to introduce the necessary transverse terms in the discretisation. A simple method to introduce transverse terms while preserving constancy (e.g. Bott, 2010) corresponds to the following steps to advance from time n to time $n+1$

$$\begin{aligned}
(h_k q_k)^\star &= (h_k q_k)^n - \Delta t \left(w^{\mathrm{s}}_{k+1/2} \tilde{q}^n_{k+1/2} - w^{\mathrm{s}}_{k-1/2} \tilde{q}^n_{k-1/2} \right) \\
h^\star_k &= h^n_k - \Delta t \left(w^{\mathrm{s}}_{k+1/2} - w^{\mathrm{s}}_{k-1/2} \right) \\
(h_k q_k)^{\star\star} &= (h_k q_k)^\star - \Delta t \partial_x (u_k (h_k q_k)^\star) \\
h^{\star\star}_k &= h^\star_k - \Delta t \partial_x (h^\star_k u_k) \\
(h_k q_k)^{n+1} &= (h_k q_k)^{\star\star} - \Delta t \partial_y (v_k (h_k q_k)^{\star\star}) \\
h^{n+1}_k &= h^{\star\star}_k - \Delta t \partial_y (h^{\star\star}_k v_k)
\end{aligned}$$

where the discrete form of the ∂_x and ∂_y operator is given by any coupled space and time scheme. The order of integration in the different direction must be permuted at each time-step to further reduce splitting errors. With this type of approach the stability constraint is given by

$$\max\{\alpha^x, \alpha^y, \alpha^z\} \leq 1$$

which is less stringent than (7.2).

For coastal applications, Shchepetkin (2015) has emphasised the severe stability constraint potentially imposed by an explicit treatment of vertical advection. Several ways can be used to mitigate this issue: *(i)* use a semi-implicit advection scheme; *(ii)* use a local time-step for vertical advective terms based on the maximum vertical Courant number in each water column; *(iii)* use a quasi-Lagrangian vertical coordinate which is subject to a gentle Lipschitz stability condition rather than the usually severe CFL condition (e.g. James, 2000; White et al., 2009). This last remark applies to models using rezoning/remapping strategies because models using a transport algorithm instead of remapping (e.g. Hofmeister et al., 2010) will still be subject to a CFL type stability constraint.

In coastal ocean models with bottom-following coordinates (see Sec. 2.1 and Sec. 4.2.2), the coordinate surfaces may intersect with isopycnal or geopotential surfaces at a relatively large angle when the bathymetry is steep. This makes it significantly harder to accurately compute the internal pressure gradient force $F^{\mathrm{IPG}}_{[\mathrm{x,y}],k}$ defined in (4.5) since the buoyancy integrals $I_b(z) = \int_z^\eta b(x,y,z')\mathrm{d}z'$ are not directly available along constant horizontal surfaces. Using the notations introduced in Sec. 4, for a generalised vertical coordinate s, the x-component of the corresponding gradient can be alternatively expressed using the chain rule

$$\left(\partial_x I_b\right)_z = \left(\partial_x I_b(z)\right)_s + b\left(\partial_x z\right)_s . \tag{7.3}$$

The subscript s is denoting differentiation with respect to constant s. In an arbitrary general coordinate the two terms in rhs are nontrivial, of opposite sign and may be large compared to the order of magnitude of their difference. The second term in the rhs in (7.3) is sometimes referred to as compensating hydrostatic term which vanishes for geopotential coordinates ($s = z$).

7.2.1 Discretization of horizontal pressure gradient term

At a discrete level, unbalanced truncation errors in the computation of the two large terms in the rhs of (7.3) will interfere with each other and give rise to a possibly large pressure-gradient error leading to hydrostatic inconsistency manifested by unphysical spontaneous motions. A very large body of literature is dedicated to this subject (e.g. Blumberg and Mellor, 1987; Mellor et al., 1994; McCalpin, 1994; Burchard and Petersen, 1997; Lin, 1997; Shchepetkin and McWilliams, 2003; Adcroft et al., 2008; Marsaleix et al., 2011; Berntsen, 2011) where different strategies have been followed to reformulate (7.3) in a way more convenient for the discretisation. Those strategies are generally motivated either by achieving a high-order accuracy to cancel the two terms in (7.3) in the case of a flat stratification (e.g. McCalpin, 1994; Shchepetkin and McWilliams, 2003) or by ensuring an energetic consistency (e.g. Marsaleix et al., 2008). In this latter case, the aim is to make sure in a discrete sense that the change of kinetic energy due to the work of pressure forces is balanced by the change of potential energy due to buoyancy forces. This balance occurs only with a linear equation of state and involves the discrete advection for density (e.g. Shchepetkin and McWilliams, 2003, App. A).

Mainly three strategies have been followed in practical applications to reformulate and discretise (7.3). *(i)* A first strategy is to directly use (7.3). When discretising this form of pressure gradient, averaging of $I_b(z)$ in the vertical and b in the horizontal are needed since the only term computed at its natural position is $(\partial_x z)_s$. According to Shchepetkin and McWilliams (2003) this explains why this approach is often prone to large hydrostatic inconsistencies. However, high-order schemes have been proposed in McCalpin (1994) to compute the horizontal derivatives and horizontal averaging of b combined with a spectral representation in the vertical. *(ii)* a second and intuitive approach consists in computing $I_b(z)$ and then to vertically interpolate the result at an horizontal surface of reference before differentiating (e.g. Lin, 1997; White et al., 2009). This is the preferred option in atmospheric models. In Lin (1997) a flux-form finite-volume approach based on this concept is adopted. *(iii)* the preferred approach for most oceanic models is to use a *density-Jacobian* discretisation. With the Leibniz rule we easily obtain that

$$\left(\partial_x I_b\right)_z = b(\eta)\partial_x\eta + \int_z^\eta \underbrace{\left[\left(\partial_x b\right)_s - \partial_{z'} b\left(\partial_x z'\right)_s\right]}_{\mathscr{J}_{x,z'}(b,z')} \mathrm{d}z'. \tag{7.4}$$

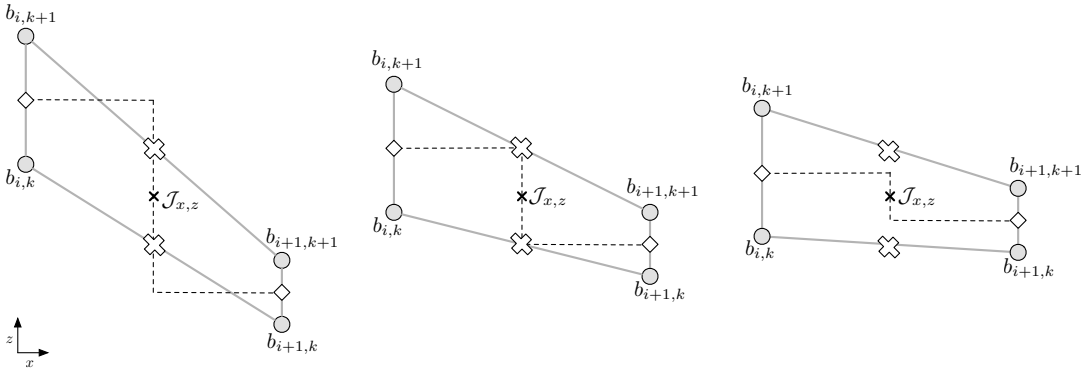

Fig. 5. Elementary computational stencil of the standard second-order density Jacobian $\mathscr{J}_{x,z}$ for different values of the grid slope r_x. The quantity $|r_x|$ geometrically corresponds to the vertical distance between the two white diamonds (located at $z_{i,k+1/2}$ and $z_{i+1,k+1/2}$) divided by the distance between the two white crosses (located at $z_{i+1/2,k}$ and $z_{i+1/2,k+1}$).

Compared to the straight-forward approach (7.3) differentiation comes first and integration then. The density-Jacobian formulation clearly shows that if $s = \rho$ only one term is nonzero and the pressure gradient term can be computed accurately provided that proper care is taken to the equation of state (Adcroft et al., 2008). The Jacobian in (7.4) must be computed at cell corners, if we refer to Fig. 5 a standard second-order discretisation reads

$$(\mathscr{J}_{x,z})_{i+1/2,k+1/2} = \frac{1}{2\Delta x}\Big\{(1+r_x)b_{i+1,k+1} + (1-r_x)b_{i+1,k} \\ -(1-r_x)b_{i,k+1} - (1+r_x)b_{i,k}\Big\} \tag{7.5}$$

with $r_x = -\frac{z_{i+1,k+1/2} - z_{i,k+1/2}}{z_{i+1/2,k+1} - z_{i+1/2,k}} = -(\Delta x/\Delta z)(\partial_x z)_s$ the grid slope. This discretisation of the Jacobian has been widely used in coastal models for years. It can be shown that the standard second-order Jacobian discretisation corresponds to a discrete form of Green's theorem since (7.5) can be written as the sum of four line integrals discretised using a simple trapezoidal rule. Shchepetkin and McWilliams (2003) have introduced a high-order (cubic) discretisation for those line integrals. The resultant scheme turned out to be a significant step forward compared to existing approaches.

Besides the imbalance in the truncation errors in (7.3) there is an other source of pressure gradient error stemming from the use of a nonlinear equation of state including compressibility of seawater (Dukowicz, 2001). Ways to remove this source of error by rearranging the terms in the equation of state are presented in Shchepetkin and McWilliams (2003), Adcroft et al. (2008) or Marsaleix et al. (2011). This latter source of error is sometimes overlooked, however it must be stressed that the careless inclusion of compressibility terms into the equation of state would have significant dynamic consequences.

7.2.2 *Control of pressure gradient discretization errors*

Following Mellor et al. (1994), a simple form of the truncation error, neglecting the horizontal derivatives involving buoyancy, associated to discretization (7.5) can be expressed as

$$\mathscr{E}_{\text{ipg}} = \frac{(\partial_x H)_s}{4H}\left\{\Delta z^2 - \Delta x^2 (\partial_x z)_s^2\right\}\left(\partial_z^2 b + \frac{1}{3} z \partial_z^3 b\right) + \mathscr{O}(\Delta x^4, \Delta z^4, \Delta x^2 \Delta z^2) \tag{7.6}$$

in the case of a separable σ coordinate. The expression for $\mathscr{E}_{\text{ipg}}$ shows that the leading order error vanishes for $r_x = \pm 1$ (i.e. $\Delta z = \pm \Delta x (\partial_x z)_s$), for $r_x = 0$ (i.e. $\partial_x H = 0$) and for a linear buoyancy profile ($\partial_z^m b = 0, m \geq 2$). Provided that sufficient computational power is available, (7.6) also shows that refining jointly the horizontal and vertical resolution is an obvious way to reduce IPG errors. More generally, the value of the parameter r_x in (7.5) is usually considered a good qualitative indicator of discretisation errors. For $|r_x| \leq 1$ the discretisation is expected to be fairly accurate since it is based on vertical interpolations, this is the so-called "hydrostatic consistency" situation (Fig. 5). Values of $|r_x|$ greater than 1 generally lead to a degradation of the accuracy due to the need of vertical extrapolation to compute the pressure gradient term. This corresponds to a situation of "hydrostatic inconsistency", see Haney (1991). However, this notion of "hydrostatic consistency" has to be considered with care since in general the actual discretization error of IPG discretizations does not behave monotonically with r_x. As emphasized by Mellor et al. (1994), the error compensation between the two terms in curly brackets in (7.6) can lead to smaller errors in hydrostatic inconsistency situations (typically for $|r_x|$ slightly larger than 1) than in hydrostatic consistency situations (for r_x around $1/2$). A usual requirement to avoid the emergence of spurious motions is to keep the value of r_x and/or of the slope parameter $\Delta x |\frac{(\partial_x H)_s}{2H}|$ at a reasonable level. To do so several ways are commonly used concurrently: *(i)* bathymetry smoothing (e.g. Martinho and Batteen, 2006) is systematically used in terrain-following coordinates to limit the maximum slopes; *(ii)* the function responsible for the vertical placement of grid points is designed in such a way to minimise the departure of the vertical coordinate isosurfaces from the horizontal direction (e.g. Schär et al., 2002; Shchepetkin and McWilliams, 2009b; Berntsen, 2011; Lemarié et al., 2012b) or alternatively use a mixed z-s coordinate transformation to flatten the vertical levels in predefined sub-domains (e.g. Deleersnijder and Beckers, 1992; Burchard and Petersen, 1997; Shapiro et al., 2013); *(iii)* a quasi-Lagrangian vertical coordinate whose layer distribution in the rezoning step can be chosen to reduce grid slopes or to follow isopycnals (e.g. White et al., 2009; Hofmeister et al., 2010; Leclair and Madec, 2011). Besides the approaches discussed so far, we could imagine alternative strategies. For example, the coordinate system could be determined using only the low-frequency variations in the bathymetry and high frequencies could be handled using an immersed boundary method (e.g. Lundquist et al., 2010). Other alternatives could be the use of well-balanced discretisations (Botta et al., 2004) or to express horizontal momentum using the covariant velocity components instead of the usual contravariant components (Weller and Shahrokhi, 2014). Eventually, as emphasised by Mellor et al. (1994), the interaction between pressure gradient and other terms in the equations should be further clarified, especially the interaction with active tracers advection.

7.3 *Coriolis term (inertial oscillations)*

In the absence of other terms but Coriolis terms in (A.2) and (A.3) we obtain the equations of free motion on a rotating plane

$$\partial_t (h_k u_k) = f h_k v_k; \quad \partial_t (h_k v_k) = -f h_k u_k. \tag{7.7}$$

A characteristic of the Coriolis acceleration is that it is directed perpendicular to the velocity direction. Hence, it does not play any role in the kinetic energy budget, which forms an important constraint for the discretisation (e.g. Arakawa and Lamb, 1977). In (7.7), the quantity fh_kv_k must be given at u-points and fh_ku_k at v-points. If (7.7) is semi-discretised in space, this constraint is trivially satisfied locally on an Arakawa B-grid, since u and v are collocated, but can only be satisfied globally on an Arakawa C-grid. Considering that the Coriolis frequency f is cell centered [4], the following discretisation of the rhs in (7.7)

$$(fh_kv_k)_{i+1/2,j} = \overline{f_{i,j}h_{i,j,k}\overline{v}^{y}_{k}}^{x}, \qquad (fh_ku_k)_{i,j+1/2} = \overline{f_{i,j}h_{i,j,k}\overline{u}^{x}_{k}}^{y}, \tag{7.8}$$

where $\overline{\cdot}^{m}$ is an averaging operator in the direction m ($m = x, y$), ensures that all the terms associated to the Coriolis force cancel when a kinetic energy equation is derived from (A.2) and (A.3) (Sec. III.C in Arakawa and Lamb, 1977). In (7.8), the horizontal variations of the curvature metric terms have been ignored for clarity. An alternative energetically-neutral discretisation providing a different logic for the cancellation of the terms when the kinetic energy budget is formed at the discrete level has been introduced in Espelid et al. (2000) and reads

$$(fh_kv_k)_{i+1/2,j} = f_{i+1/2,j}\overline{(h_kv_k)}^{w}_{i+1/2,j}; (fh_ku_k)_{i,j+1/2} = f_{i,j+1/2}\overline{(h_ku_k)}^{w}_{i,j+1/2}, \tag{7.9}$$

where $\overline{\cdot}^{w}$ is a weighted average defined as

$$\overline{(h_kv_k)}^{w}_{i+1/2,j} = \frac{w_{i+1/2,j,k}}{4}\sum_{n=0}^{n=1}\sum_{m=0}^{m=1}\frac{(hv)_{i+n,j-m+1/2,k}}{w_{i+n,j-m+1/2,k}};\ w_{i+1/2,j,k} = \sqrt{\frac{gh_{i+1/2,j,k}}{|f_{i+1/2,j}|}}$$

for each layer k, same rationale applies to $\overline{(h_ku_k)}^{w}_{i,j+1/2}$. Compared to (7.8), this formulation requires the Coriolis parameter to be defined at u and v points and allows more freedom in the way to define the thickness layer h_k at cell interfaces since in (7.8) h_k at cell interfaces has to be equal to the half sum of surrounding cell centered values of h, this constraint is absent in (7.9).

When the time dimension is discretised, a simple forward Euler step to integrate (7.7) would be unconditionally unstable. The use of a (semi)-implicit scheme would remove stability constraints. This approach is essentially adopted in models which treat the gravity waves in a semi-implicit way (e.g. Walters et al., 2009). In general, for coastal applications, the baroclinic time-step is much smaller than the inertial period meaning that the Coriolis term is not expected to impose any limitation on the time-step. For this reason explicit schemes are generally preferred. To circumvent the stability issues of the Euler forward step, a Forward-Backward in Time (FBT) approach is often used (Bleck and Smith, 1990)

$$\begin{aligned}(h_ku_k)^{n+1}_{i+1/2,j} &= (h_ku_k)^{n}_{i+1/2,j} + \Delta t(fh_kv_k)^{n+m}_{i+1/2,j}\\ (h_kv_k)^{n+1}_{i+1/2,j} &= (h_kv_k)^{n}_{i+1/2,j} - \Delta t(fh_ku_k)^{n+1-m}_{i,j+1/2},\end{aligned} \tag{7.10}$$

and is stable for $f\Delta t \leq 2$. In (7.10), m is either 0 if n is even or 1 otherwise. Other popular explicit schemes to integrate (7.7) include the third-order Adams-Bashforth scheme (stable for $f\Delta t \leq 0.72$) and the leapfrog scheme (stable for $f\Delta t \leq 1$).

[4] In most coastal models, the Coriolis frequency is cell-centered while in large-scale models it is often located at cell-corners since it is required to use potential enstrophy conserving discretization schemes.

Elements about the temporal discretization of external gravity waves are introduced in Sec. 5.1 so that we focus here on internal gravity waves. The numerical integration of those waves can be studied using the following two-dimensional subsystem of equations (3.1), (3.3), (3.10), (3.12)

$$\begin{aligned} \partial_x u + \partial_z w &= 0 \\ \partial_t u + (g/\rho_0)\partial_x \left(\int_z^0 \rho \, \mathrm{d}z' \right) &= 0 \\ \partial_t \rho + \partial_x (u\rho) + \partial_z (w\rho) &= 0 \end{aligned} \tag{7.11}$$

which represents the interactions between momentum and tracer equations, assuming a linear equation of state. Historically, in large-scale and coastal models based on leapfrog time-stepping a very popular scheme to integrate (7.11) was the pressure gradient averaging (a.k.a. Shuman averaging) approach of Brown and Campana (1978) which corresponds to the following steps

$$\begin{aligned} w^n &= \int_{-H}^{z} \partial_x u^n \mathrm{d}z' \\ \rho^{n+1} &= \rho^{n-1} - 2\Delta t \partial_x (u^n \rho^n) - 2\Delta t \partial_z (w^n \rho^n) \\ u^{n+1} &= u^{n-1} - 2(\Delta t/\rho_0)\partial_x \left(\int_z^0 \left[\frac{1}{2}\rho^n + \frac{1}{4}(\rho^{n-1} + \rho^{n+1}) \right] \mathrm{d}z' \right) \end{aligned} \tag{7.12}$$

where the weights in the averaging are chosen to allow the larger stability constraint. For coastal models based on 2-level (one-step) time-stepping the simpler strategy is the so-called forward-backward approach (e.g. Mesinger and Arakawa, 1976)

$$\begin{aligned} w^n &= \int_{-H}^{z} \partial_x u^n \mathrm{d}z' \\ \rho^{n+1} &= \rho^n - \Delta t \partial_x (u^n \rho^n) - \Delta t \partial_z (w^n \rho^n) \\ u^{n+1} &= u^n - (\Delta t/\rho_0)\partial_x \left(\int_z^0 \rho^{n+1} \mathrm{d}z' \right) \end{aligned} \tag{7.13}$$

In the same spirit as (7.13), the time staggering of tracers and momentum equations (e.g. Backhaus, 1985) provides an efficient scheme since it allows some implicitness in the coupling between the two equations. All the schemes discussed so far are second-order accurate and lead to the following stability constraint on a staggered C-grid

$$\alpha_{\mathrm{igw}} = \Delta t \sqrt{c_1^2 \left(\frac{1}{\Delta x^2} + \frac{1}{\Delta y^2} \right)} \leq 1$$

where c_1 is the speed of the fastest internal wave which can be as large as $3.8 \ \mathrm{m \ s^{-1}}$ (e.g. Fig. 3 in Lemarié et al., 2015). Same stability constraint is obtained if the order of integration between momentum and tracer equations is reversed in (7.12) and (7.13). The forward-backward and pressure gradient averaging approaches provide a good combination of efficiency, simplicity and large stability range for internal gravity waves integration, with less emphase on accuracy. However, as resolution keeps increasing in coastal models, a wider spectrum of internal waves can be explicitly represented and accuracy in time and space should also be considered a priority. Better accuracy in time can be achieved by using either high-order predictor-corrector schemes (e.g. Shchepetkin and McWilliams, 2005), or 2-level schemes

(e.g. Rueda et al., 2007; Shchepetkin and McWilliams, 2009a) with forward-backward feedbacks between momentum and tracers equations. As far as the spatial discretisation is concerned, the overwhelming majority of oceanic models consider simple second-order schemes to compute the horizontal divergence ($\partial_x u$ in (7.11)) in the continuity equation and the horizontal pressure gradient ($\partial_x \int_z^0 \rho \mathrm{d}z'$ in (7.11)). However studies by Blayo (2000) and Demange et al. (2014) emphasised that higher-order approximations of those two terms would allow a significantly better representation of internal waves propagation, compared to standard algorithmic choices.

7.5 Orientation of diffusion tensor and numerically-induced mixing

7.5.1 Orientation of diffusion tensor

In (3.18), (3.16) and (3.17) the horizontal turbulent fluxes are oriented in the horizontal direction. For simplicity, in some models the diffusion terms are not transformed to non-orthogonal vertical coordinates, but replaced by diffusion along the model layers. However, in the case of a stratified flow, if the vertical coordinate $s \neq \rho$ it is well known that maintaining the tracer diffusion tensor along the coordinate lines can be responsible for non-physical mixing of water masses and associated spurious baroclinic currents (e.g. Barnier et al., 1998). It is thus relatively common for non-isopycnic models to implement a rotation of the diffusion tensor (via the rotation tensor $\mathbf{R}$ in (3.18)) in a direction non-aligned with the computational grid (e.g. Stelling and Van Kester, 1994; Griffies et al., 1998). Since for a generalized coordinate it is expected that the slope between the isopycnal direction and the direction of the computational grid is larger than for a classical z coordinate, a good compromise is generally to rotate the explicit diffusion in the geopotential direction rather than the physically correct isopycnal direction. This allows to avoid delicacies associated with the computation of isopycnal slopes in unstratified regions and at the intersection with the surface and the bottom. Compared to standard implementations available in climate models, a rotation of the diffusion along isopycnals is not straight-forward in coastal models for several reasons, *(i)* at high horizontal resolution, explicit diffusion is generally handled with a biharmonic operator which is tedious to rotate, mainly for stability reasons; *(ii)* the rotated operators in climate models are derived under the small slope approximation which is not always satisfied in the coastal regions (e.g. Lemarié et al., 2012b, Sec. 2.4.2); *(iii)* because the slopes can be large in coastal applications, the rotated operator will be prone to large dispersive errors and can become inaccurate (Beckers et al., 1998, 2000; Lemarié et al., 2012a).

7.5.2 Numerically-induced mixing

A non negligible amount of non-physical mixing of water masses can also be due to the advection operator. Indeed, as mentioned earlier, oceanic coastal models generally rely either on high-order linear upwind schemes or on flux correcting/limiting approaches to discretise horizontal advection. The associated truncation errors are dissipative. Much effort have been recently directed toward the quantification and/or modification of physical orientation of this mixing of numerical nature (e.g. Burchard and Rennau, 2008; Marchesiello et al., 2009; Ilicak et al., 2012; Klingbeil et al., 2014). For example, Marchesiello et al. (2009) showed that the dissipative truncation error associated to a third-order upwind scheme in a terrain-following coordinate model was greatly exceeding the small level of physically acceptable mixing observed in the oceanic interior. The physical results proved to be greatly improved by splitting the third-order upwind scheme between a centered and a diffusive part and when the diffusive part is rotated in the isopycnal direction (Marchesiello et al., 2009; Lemarié et al., 2012b). An alternative approach to have more control on the orientation of mixing for coastal applications is the use of quasi-Lagrangian approach

(e.g. Hofmeister et al., 2010; Leclair and Madec, 2011). Besides the orientation of the diffusion tensor, Ilicak et al. (2012) emphasised that spurious diapycnal mixing can be aggravated if the grid Reynolds number is too large (i.e. if the velocity field is not smooth on the grid scale). Besides advective terms and explicit diffusion operators, other components of numerical models can be a source of "numerical mixing" (e.g. Soufflet et al., 2016). For example, the time-stepping algorithms are generally diffusive (with the exception of the Leapfrog scheme for which diffusion is provided via the Asselin filter), the stabilization of the time-splitting procedure between the barotropic and baroclinic modes requires extra diffusion (which takes the form of a filtering of the fast barotropic variables).

7.6 Bottom friction

Due to the relatively thick bottom boundary layers in the coastal ocean, see (2.1), an accurate discretisation of bottom friction is required. The no-slip bottom boundary condition for u and v (3.7) is typically not directly discretised, because a vertical resolution on scales of millimetres would be required to obtain sufficient accuracy. Instead, it is assumed that the velocity profiles in the lowest grid box of an ocean model follow the law of the wall:

$$\left[u\left(z'\right), v\left(z'\right)\right] = \frac{1}{\kappa} \ln\left(\frac{z' + z_0^{\mathrm{b}}}{z_0^{\mathrm{b}}}\right) \left[u_*^{\mathrm{b}}, v_*^{\mathrm{b}}\right], \tag{7.14}$$

with the bottom roughness length, z_0^{b}, the bottom friction velocity vector, $\left(u_*^{\mathrm{b}}, v_*^{\mathrm{b}}\right)$ and the distance from the wall, $z' = z + H$. With (7.14), the discrete bottom boundary condition (3.8) has the form of a quadratic friction law

$$\begin{aligned}
\tau_{[\mathrm{x,y}]}^{\mathrm{b}}(h,u,v) &= \left(\left(u_*^{\mathrm{b}}\right)^2 + \left(v_*^{\mathrm{b}}\right)^2\right)^{1/2} \left[u_*^{\mathrm{b}}, v_*^{\mathrm{b}}\right] \\
&= \left(\frac{\kappa}{\ln\left(\frac{h/2+z_0^{\mathrm{b}}}{z_0^{\mathrm{b}}}\right)}\right)^2 \left(u^2+v^2\right)^{1/2} [u,v] \\
&= c_{\mathrm{D}} \left(u^2+v^2\right)^{1/2} [u,v].
\end{aligned} \tag{7.15}$$

In (7.15) $\tau_{[\mathrm{x,y}]}^{\mathrm{b}}$ is the bed stress vector, c_{D} is the non-dimensional bottom drag coefficient, h is the thickness of the lowest grid box, and (u, v) is the velocity vector in the lowest grid box. Note that for the limit of $h \to 0$ we obtain $c_{\mathrm{D}} \to \infty$ and thus retain the original no-slip condition (3.7). In situations when the near-bottom velocity profile deviates strongly from the law of the wall, e.g. when stratification due to high sediment concentrations or a wave-enhanced bottom boundary layer (or both) are present, the vertical resolution needs to be sufficiently high. One other possibility would be to parameterise such unresolved processes (Burchard et al. (2008); Warner et al. (2008)).

In order to prevent instabilities, bottom friction is treated semi-implicitly in the model. An explicit discretisation of the layer-integrated momentum equation (A.2) in the bottom layer,

$$\begin{aligned}
\frac{(hu)^{n+1} - (hu)^{n+}}{\Delta t} &= -\tau_{\mathrm{x}}^{\mathrm{b}}(h, u^{n+}) \\
&\iff (hu)^{n+1} = \left(1 - \Delta t \frac{\tau_{\mathrm{x}}^{\mathrm{b}}(h,u^{n+})}{(hu)^{n+}}\right) (hu)^{n+},
\end{aligned} \tag{7.16}$$

with u^{n+} already containing all other explicit contributions, shows the constraint $\Delta t < \frac{(hu)^{n+}}{\tau_{\mathrm{x}}^{\mathrm{b}}(h,u^{n+})} = \frac{h}{c_{\mathrm{D}}|u^{n+}|}$.

Thus, for high vertical resolution towards the bottom, as typically required in coastal ocean modelling (see Section 2.1), the time step can become strongly constrained. In contrast, with the semi-implicit treatment

$$\frac{(hu)^{n+1}-(hu)^{n+}}{\Delta t}=-\frac{(hu)^{n+1}}{(hu)^{n+}}\tau_{\mathrm{x}}^{\mathrm{b}}(h,u^{n+})$$

$$\Longleftrightarrow (hu)^{n+1}=\left(1+\Delta t\frac{\tau_{\mathrm{x}}^{\mathrm{b}}(h,u^{n+})}{(hu)^{n+}}\right)^{-1}(hu)^{n+} \quad (7.17)$$

the final velocity monotonically tends to zero for increasing Δt, c_{D} or decreasing h.

The source term linearisation in (7.17) is equivalent to the so-called Patankar-trick (Patankar, 1980, Sec. 7.2-2), which is usually applied to guarantee positivity of turbulent quantities and biogeochemical tracer concentrations.

7.7 Numerical treatment of turbulence closure equations

On a Lorenz grid (see Figure 1) discrete turbulent quantities are best located at w-points, i.e. vertically between the tracer points of adjacent layers. Although this offers the prescription of Dirichlet boundary conditions for the turbulent kinetic energy (TKE) k and its dissipation rate ε directly at the bottom and the free surface, Burchard and Petersen (1999) and Burchard et al. (2005) demonstrated, that equivalent Neumann boundary conditions provide much higher accuracy in reproducing the law of the wall.

The temporal discretisation of the prognostic equations for the non-negative scalars k and ε also requires specific care. These quantities often cover several orders of magnitude across fairly short time and spatial scales such as in oscillating tidal flow. For example, a straightforward, explicit-in-time discretisation of the TKE equation (3.19) might require very small time steps during slack tide, when production is small and dissipation is high, in order to guarantee positivity of k (see analogy to (7.16)). Therefore, the so-called Patankar trick (see analogous source term linearisation in (7.17)) is used in almost all discretisations of turbulence closure budget equations, including those for other parameters such as the dissipation rate ε and the turbulence frequency ω, see Deleersnijder et al. (1997) and Burchard et al. (2005) for details.

Another issue of the numerical treatment of turbulence closure models is the energy-consistency between mean flow and turbulence. Physically, the kinetic energy extracted from the mean flow due to vertical stress divergence is a source of turbulent kinetic energy transferred as shear production P. The same applies to the exchange of energy between mean potential energy and turbulence kinetic energy which is transferred as buoyancy production B. Burchard (2002b) shows how a consistent energy exchange can be obtained also on the numerical level.

8 Existing coastal ocean community models

Previous sections have discussed the various choices that have to be made when designing a numerical model with a focus on coastal applications. The present section gives an overview of the specifics of some existing hydrostatic and non-hydrostatic structured-grid models to illustrate the diversity of methods in use in coastal models and their evolution over the years. We have strived here to present a fair description of past and ongoing developments, however the reader must be warned that omissions and inaccuracies in the model description are inherent to this type of exercise.

8.1 Hydrostatic structured-grid models

In this subsection examples of structured-grid oceanic models used in practice to tackle research or engineering applications related to coastal environments are given, see Tab. 1 for a list of the most popular models historically used in this context. In this list we can find models originally designed for shallow seas applications (e.g. BOM, COHERENS, GETM, HAMSOM, Mars3D, MOHID), as well as mesoscale oceanic models (like NCOM, POLCOMS, POM or ROMS), originally designed to cover shelf seas and open ocean regions, and later adapted to handle nearshore and coastal scales (e.g. Oey, 2005; Uchiyama et al., 2010; Warner et al., 2013). More recently, global climate models (e.g. NEMO, Hycom) are also sometimes used to study shelf processes provided some adjustments in their numerical formulation (e.g. Leclair and Madec, 2011; Lahaye et al., 2011). Finally, models specifically designed for commercial/engineering applications (e.g. Delft3D, ECOM-si, MIKE 3, TRIM3D) can also be used for real case studies (e.g. Cheng et al., 1993). As summarised in Tab. 2, the choice of discrete algorithms in oceanic models bear the imprints of their original target application and development time. In the 90's the situation was very clear: climate models were generally discretised on a B-grid using a geopotential coordinate under the rigid-lid assumption and leapfrog (LF) time-stepping (Griffies, 2004) while mesoscale models, largely inspired by POM, made use of a C-grid, a terrain-following coordinate and an explicit free surface. At that time coastal and engineering models were predominantly C-grid models based on a semi-implicit free surface and baroclinic foward in time methods influenced by Backhaus (1985) and Casulli and Cheng (1992). Nowadays, the distinction between the different class of models is less clear because newly developed models are generally designed to handle a larger range of spatio-temporal scales permitted by the advances in computational power and the maturity of nesting strategies (see Sec. 6). In early 2000's, the emergence of models like ROMS, GETM or Hycom came with a thorough rethinking of several model components like time-stepping algorithms (Shchepetkin and McWilliams, 2005), vertical coordinate (Bleck, 2002; Burchard and Beckers, 2004), turbulent closure schemes (Umlauf and Burchard, 2003), or open boundary conditions (Marchesiello et al., 2001) which increased further the diversity of models. Tab. 2 reflects the variety of models and modelling techniques that are presently used. However some general trends can be distinguished :

- Models originally developed with coastal applications in mind are characterized by 2-level (one-step) time-stepping with a coupled space and time treatment of advective terms. This choice combines simplicity and ease to implement monotonicity-preserving advection.
- The majority of models based on a coupled space and time approach favour the superbee slope limiter to impose the TVD property. This choice corresponds to the upper boundary of the TVD region and leads to the least numerical diffusion among the existing slope limiters (e.g. Cushman-Roisin and Beckers, 2011). However, this limiter tends to erroneously amplify the gradients. According to Durran (2010), the monotonized centered limiter is expected to provide superior results in terms of accuracy. Other flux-limiter methods currently used for practical applications is the ultimate quickest scheme (or equivalently the so-called P2-PDM scheme). Note that the WENO or FCT approaches are still relatively marginally used.
- As motivated in Sec. 3.2.1, the overwhelming majority of coastal models rely on TKE-based vertical closure models. A dynamic equation for TKE is solved either in combination with a diagnostic mixing length or with a second dynamic equation for a length related quantity.
- The recently developed models are almost exclusively based on a split-explicit mode splitting (SPE; see Section 5.1.2) which allows more accuracy in the computation of fast barotropic waves (see final paragraph in Section 5.1.2) and is expected to provide enhanced scalability and performance on

parallel computers.

- The vertical coordinate system is one of the aspects that focuses the most attention nowadays. The general trend is to allow more flexibility in the definition of the coordinate within the Arbitrary Lagrangian-Eulerian framework (see Sections 4.2.3 and 4.2.4).

8.2 Non-hydrostatic models

Within the last decade several existing coastal ocean models mentioned above were extended to abandon the hydrostatic pressure assumption (POM: Kanarska and Maderich (2003), BOM: Heggelund et al. (2004), ROMS: Kanarska et al. (2007), Symphonie: Auclair et al. (2011), GETM: Klingbeil and Burchard (2013)). Scaling analysis shows that the nonhydrostatic pressure contribution, formally defined by

$$\partial_z p_{\mathrm{nh}} = -\rho_0 \left(\partial_t w + \partial_x \left(uw \right) + \partial_y \left(vw \right) + \partial_z \left(ww \right) - f_{\mathrm{h}} u - F_{\mathrm{z}} \right), \tag{8.1}$$

cannot be neglected when approaching sufficiently high spatial resolutions that promote processes with significant vertical accelerations (Marshall et al., 1997; Klingbeil and Burchard, 2013). Practical examples on coastal ocean scales are flows above irregular topography, high-frequency internal gravity waves or gravity plumes. In order to simulate these processes in a physically correct way, the vertical momentum balance must not be degenerated to (3.2) anymore.

For solving the full set of incompressible Navier-Stokes equations algorithms were implemented on top of the hydrostatic model kernels that do not require a complete rewrite of the existing kernels. These were usually based on either the classical projection method (Chorin, 1968; Témam, 1969) or the pressure correction method (van Kan, 1986). Both methods require the solution of a Poisson equation for either the nonhydrostatic pressure (Kanarska and Maderich, 2003; Heggelund et al., 2004) or its correction (Kanarska et al., 2007; Auclair et al., 2011), which should be derived by inserting the discrete momentum equations into the discrete incompressibility condition to force a divergence-free final velocity field. The specific characteristics of coastal ocean models demand for some adaptations and care, e.g. for the consistent coupling of the free surface to the corrected nonhydrostatic velocities or for the numerical treatment of the additional diagonals in the coefficient matrix that, in general, is neither symmetric nor positive-definite due to cross-terms caused by the non-orthogonal vertical coordinate transformation. Strategies to avoid the additional diagonals were presented by Heggelund et al. (2004) and Berntsen and Furnes (2005). Following Berntsen and Furnes (2005), Keilegavlen and Berntsen (2009) demonstrated that simulations with the nonhydrostatic pressure defined directly in σ-coordinates showed no significant deviations to results obtained with the pressure defined in z-coordinates. An alternative algorithm for weakly nonhydrostatic regimes (e.g. internal lee waves) that avoids the Poisson equation was presented by Klingbeil and Burchard (2013). They treat the nonhydrostatic pressure as the hydrostatic one, i.e. diagnose the time-lagged right-hand side of (8.1), integrate it vertically and insert it into the horizontal momentum equations.

9 Future perspectives

The present review of the numerics of structured-grid coastal ocean models gives an overview of the numerical methods available for todays coastal ocean models. There is no single model which combines all those methods. Thus, by just recombining existing methods, todays model platforms may be further improved.

Model	Acronym	website
BOM	Bergen Ocean Model	http://www.mi.uib.no/BOM/
COHERENS	Coupled Hydrodynamical Ecological model for Regional Shelf seas	http://odnature.naturalsciences.be/coherens/
Delft-3D	Deltares flow	http://oss.deltares.nl/web/delft3d
ECOM-si	Estuarine, Coastal and Ocean Model (semi-implicit)	http://woodshole.er.usgs.gov/operations/modeling/ecomsi.html
GETM	General Estuarine Transport Model	http://www.getm.eu/
HAMSOM	Hamburg Shelf Ocean Model	https://wiki.zmaw.de/ifm/TO/Hamsom/modelhistory
ROMS	Regional Oceanic Modeling System	
↪ Rutgers		https://www.myroms.org/
↪ UCLA		http://research.atmos.ucla.edu/cesr/ROMS_page.html
↪ AGRIF		http://www.romsagrif.org/
Mars3D	Model for Applications at Regional Scale	http://wwz.ifremer.fr/mars3d/
MIKE 3	Danish Hydraulic Institute	https://www.mikepoweredbydhi.com/
MOHID	Modelo Hidrodinâmico	http://www.mohid.com/
NCOM	Navy Coastal Ocean Model	http://www.dtic.mil/dtic/tr/fulltext/u2/a508063.pdf
POLCOMS	Proudman Oceanographic Laboratory Coastal Ocean Modelling System	http://cobs.noc.ac.uk/modl/polcoms/
POM	Princeton Ocean Model	http://www.ccpo.odu.edu/POMWEB/
Symphonie	Sirocco Ocean Model	http://sirocco.omp.obs-mip.fr/ocean_models/S-model
TRIM-3D	Tidal Residual, Intertidal Mudflat	
Hycom	Hybrid Coordinate Ocean Model	https://hycom.org/
NEMO	Nucleus for the European Modelling of the Ocean	http://www.nemo-ocean.eu/

Table 1
Summary of most significant oceanic models historically used for applications to three-dimensional coastal studies. The ROMS code has three variants referred to as ROMS-Rutgers, ROMS-UCLA, and ROMS-Agrif (see Shchepetkin and McWilliams, 2009b, for more details). Hycom and NEMO are examples for large scale models which are also applied to the coastal ocean.

BOM	Svendsen et al. (1996)	C	SPE	LF-AM3	LF-TR	TVD Superbee	TVD Superbee	s	MY2.5
COHERENS	Luyten et al. (1999)	C	SPI/SPE	2-level	-	TVD Superbee	TVD Superbee	s	k-ε
Delft-3D	Gerritsen et al. (2004)	C	SPI	ADI	ADI	UP3	UP3 w/ Forester fltr	z & s	k-ε
ECOM-si	Blumberg (1992)	C	SPI	2-level	θ-scheme	C2	C2	s	MY2.5
GETM	Burchard and Bolding (2002)	C	SPE	2-level	FB	TVD	TVD	adapt.	GOTM
HAMSOM	Backhaus (1985)	C	SPI	2-level	θ-scheme	TVD	TVD	z	k-ε
ROMS (Rutgers)	Haidvogel et al. (2000)	C	SPE	LF-TR	LF-AM3	UP3	MPDATA	s	GLS
ROMS (UCLA)	Shchepetkin and McWilliams (2005)	C	SPE	LF-AM3	Gen FB	UP3	UP3	s	KPP
ROMS (Agrif)	Penven et al. (2006)	C	SPE	LF-AM3	Gen FB	UP3	WENO5Z	s	KPP
Mars3D	Lazure and Salomon (1991)	C	SPI	2-level	ADI	QK3	QK3	s	GLS
MIKE 3	Pietrzak et al. (2002)	C	SPI	2-level	ADI	Ultimate QK3	Ultimate QK3	s	k-ε
MOHID	Martins et al. (2001)	C	SPI	2-level	ADI	upstream	TVD Superbee	s	GOTM
NCOM	Martin (2000)	C	SPI	LF	θ-scheme	SUP3	FCT(UP3)	hyb z/s	MY2.5
POLCOMS	Holt and James (2001)	B	SPE	2-level	FB	PPM w/ limiters	PPM w/ limiters	s	GOTM
POM	Blumberg and Mellor (1978)	C	SPE	LF	LF	C2	MPDATA	s	MY2.5
Symphonie	Johns et al. (1992) Marsaleix et al. (1998)	C	SPE	LF	LF	C4	SUP3	s	TKE
TRIM-3D	Cheng et al. (1993)	C	SPI	2-level	θ-scheme	SL	TVD Van-Leer	z	GLS
Hycom	Bleck (2002)	C	SPE	LF	LF	Enstrophy-conserving	FCT(C2)	hyb z/s/ρ	KPP
NEMO	Madec et al. (1991)	C	SPE	LF	LF	Enstrophy-	FCT(C2)	z & s	GLS

But what are the future challenges in coastal ocean modelling? There are various trends which will drive further developments. One driver is certainly the ever ongoing growth of computational resources allowing for higher spatial resolution and higher-order numerical schemes, better process representations (such as for turbulence-closure models and parameterisation of surface and internal waves), integration into regional Earth system models of growing complexity, application of more elaborate data assimilation schemes, and use of large ensemble simulations with high numbers of individual model simulations for better representation of model statistics.

Non-hydrostatic and Boussinesq assumption

The possible higher spatial resolution will in many coastal ocean scenarios allow for resolving non-hydrostatic processes. In cases where the horizontal resolution becomes substantially smaller than the water depth, hydrostatic models would loose their predictability when for example relatively short internal waves still propagate at their hydrostatic phase speed. Therefore, one challenge to the developers of coastal ocean models is to allow for efficient non-hydrostatic pressure calculation in situations where needed. As discussed in section 8.2, there are only a few of such examples among the structured-grid models. The challenge would therefore be that models automatically analyse whether in some regions the non-hydrostatic pressure contribution is relevant, and if so, the non-hydrostatic dynamics should be applied. On other (e.g., shallower) parts of the model domain it might be ignored. It should however be kept in mind that diagnosed non-hydrostatic pressure might also be a numerical artefact (Vitousek and Fringer, 2011).

Another possibility to consistently add non-hydrostatic effects, while avoiding the costly direct solution of a 3D Poisson equation for the pressure, is to relax both the hydrostatic and Boussinesq assumptions (Auclair et al., 2016). Since relaxing the Boussinesq assumption reintroduces the acoustic waves, an acoustic mode must be considered on top of the internal and external modes. This three-mode approach has the advantage to be completely explicit (i.e. local in space) and thus to have very good properties in terms of scalability. However, it raises new challenges to derive consistent open boundary conditions to couple models based on different modeling assumptions.

Physics-dynamics coupling

The development of numerical models generally dissociates the dynamical kernel, which handles the resolved scales, from the ”physics”, that account for under-resolved processes. However, both components are strongly coupled since there is constantly a transfer of information back and forth from the dynamics to the physics so that the dynamical core must not violate physical principles. Energy-consistency is certainly one important example of such coupling. As discussed in section 7.1, most advection schemes are not variance conserving, which means for the momentum budget violation of kinetic energy conservation. The rate of numerical dissipation can be diagnosed (e.g. Klingbeil et al., 2014) and it can be shown that more complex advection schemes limit the numerical dissipation (Mohammadi-Aragh et al., 2015). Another source of energy-conservation violation is due to the exchange between mean kinetic energy and potential energy. This exchange is represented by the pressure-gradient term in the momentum equations and the advection terms of the temperature and salinity equations. Since those terms are discretised completely independently, energy-consistency is not given. Another issue is the energy consistency between loss of mean kinetic energy due to vertical stress divergence and production of turbulent kinetic energy (see

section 7.7 and Burchard, 2002b). Generally better energy-consistency may also be achieved by more suitable choices for vertical coordinates. As discussed in section 4.2, generalised vertical coordinates give a high degree of freedom to construct an optimised vertical grid layout. This flexibility needs to be better exploited in the future to improve the performance of coastal ocean models.

It should be briefly mentioned that also the physics of coastal ocean models (as well as for large scale ocean models) is generally not energy-consistent, since e.g. the energy lost by horizontal stress divergence is not reintroduced into any other energy compartment of the model. This is an important issue which could however not be further discussed in this numerical review (see e.g., the discussion by Eden et al., 2014).

Multi-resolution strategies

One other aspect of ongoing discussions in the coastal ocean developers community is the optimal layout for horizontal grids. In both, structured-grid and unstructured-grid models, substantial progress has been made in the past. While unstructured-grid models have inherent ability to solve multi-scale problems, the numerical cost per nominal grid point is generally much larger than for structured-grid models. It does therefore depend on the kind of problem to decide which type of model is better suited. For complex domains such as lagoon systems or estuarine networks, unstructured-grid models are the better choice while for classical coastal or shelf sea scenarios structured-grid models are more efficient. Structured-grid models have gained flexibility due to more flexible grids (such as curvilinear grids, see section 4 or two-way nesting, see section 6.3). Flexible multi-level nesting strategies reducing the number of masked grid points (land points) in the model domain might in the future help to better tackle multi-scale problems using structured grids. And there are efforts to increase the efficiency of unstructured-grid models. However most of them still lack the capability of local time refinement, which could prevent the use of (possibily inaccurate) implicit schemes or the model time step to be constrained by the smallest element size. A long standing issue for the use of unstructured-grid models for large scale applications (and thus for multi-scale simulations) lies in the existence of numerical modes, in particular for high order schemes (e.g. Danilov, 2013) . These spurious modes, also present on structured meshes, are triggered to a greater extent by the irregularity of the grid. To this respect, mixed (structured+unstructured) meshes, with unstructured elements being used only near the coast, provide a promising approach. Both types of models - structured-grid models with flexible nesting and unstructured-grid models - might in the future support horizontal mesh-adaptivity to resolve moving or intermittent dynamic features (as for example done in larger scale models to follow hurricanes). It depends on the success of such developments which type of model is gaining more ground in the future of coastal ocean modelling.

Coupling with other earth system compartments

Finally, stand-alone hydrodynamic coastal ocean models will always have a limited area of application. All such models are developed to also function as hydrodynamic core of coupled model systems. Most common is the coupling to biogeochemical models, where the hydrodynamic model provides advective and turbulent transports as well as the light regime and many other potential functional links between hydrodynamics and biogeochemistry. Without accurate physical and numerical representation of the hydrodynamics (e.g., in terms of the mixed-layer depth), biogeochemical models will have no predictability. Links between hydrodynamics and biogeochemistry may be complex. One tool to flexibly provide such a

link is FABM (Framework of Biogeochemical Models, Bruggeman and Bolding (2014)).

Coupling to several other Earth system compartments is common, such as to statistical surface wave models, sea ice models, atmospheric models, benthic models, and hydrological models. Several comprehensive system models exist, such as COAWST (Warner et al., 2008), interactively coupling hydrodynamics (from ROMS) with surfaces waves, atmosphere, biogeochemistry, sediment transport and benthos to study complex coastal ocean scenarios in hindcast and sensitivity mode, or NEMO-Nordic (Gröger et al., 2015), coupling hydrodynamics (from NEMO) with atmosphere, sea ice, biogeochemistry, and hydrology for the purpose of regional climate downscaling and sensitivity scenarios. It is obvious that all coupling interfaces to other compartments require hydrodynamic process adaptations on the side of the hydrodynamic module, and that those need to be numerically discretised with care. It is expected that in the future, such complex coupled model systems will be much more widely used, such that quite some pressure to further develop hydrodynamic model will be generated.

Despite the substantial growth of computational resources, regional climate system models with runtimes of typically more than a century and which maybe executed as large ensemble runs with many individual simulations will require high accuracy at relatively low resolution. Therefore the development of efficient and accurate numerical schemes at low resolution will be an important task also for the future.

Acknowledgements: This paper is a contribution to the project M5 (Reducing spurious diapycnal mixing in ocean models) of the Collaborative Research Centre TRR 181 on Energy Transfer in Atmosphere and Ocean funded by the German Research Foundation. Further support has been granted by the project MOSSCO (Modular System for Shelves and Coasts) funded by the German Federal Ministry of Research and Education (BMBF) under the project identification number FKZ 03F0667B. F. Lemarié and L. Debreu acknowledge the support of the french national research agency (ANR) through contracts ANR-14-CE23-0010 (HEAT) and ANR-16-CE01-0007 (COCOA). We are grateful to Robert Hallberg (Princeton) for discussing principles of turbulence closure schemes for global ocean models with us. Furthermore, we would like to thank Martin Schmidt (Warnemünde) for many helpful discussions. Finally, we appreciate the very constructive comments from Sergey Danilov and five anonymous reviewers.

A Set of layer-integrated equations

The layer-integrated continuity equation (3.1) reads:

$$\partial_t h_k + \partial_x \left(h_k u_k\right) + \partial_y \left(h_k v_k\right) + \left(w^{\mathrm{s}}_{k+1/2} - w^{\mathrm{s}}_{k-1/2}\right) = 0, \tag{A.1}$$

The layer-integrated momentum equations (3.3) and (3.4) are:

$$\begin{aligned} &\partial_t \left(h_k u_k\right) + \partial_x \left(h_k u_k u_k\right) + \partial_y \left(h_k v_k u_k\right) + \left(w^{\mathrm{s}}_{k+1/2}\widetilde{u}_{k+1/2} - w^{\mathrm{s}}_{k-1/2}\widetilde{u}_{k-1/2}\right) \\ &= h_k \widetilde{F}^{\mathrm{h}}_{\mathrm{x}}(h_k, u_k, v_k) + \left(\tau_{\mathrm{x},k+1/2} - \tau_{\mathrm{x},k-1/2}\right) \\ &\quad + f h_k v_k - h_k \tfrac{1}{\rho_0}\partial_x p_a - g h_k \partial_x \eta + h_k F^{\mathrm{IPG}}_{\mathrm{x},k}, \end{aligned} \tag{A.2}$$

$$\partial_t\left(h_k v_k\right)+\partial_x\left(h_k u_k v_k\right)+\partial_y\left(h_k v_k v_k\right)+\left(w^{\mathrm{s}}_{k+1/2}\widetilde{v}_{k+1/2}-w^{\mathrm{s}}_{k-1/2}\widetilde{v}_{k-1/2}\right)$$

$$=h_k\widetilde{F}^{\mathrm{h}}_{\mathrm{y}}(h_k,u_k,v_k)+\left(\tau_{\mathrm{y},k+1/2}-\tau_{\mathrm{y},k-1/2}\right) \tag{A.3}$$

$$-fh_k u_k-h_k\tfrac{1}{\rho_0}\partial_y p_a-gh_k\partial_y\eta+h_k F^{\mathrm{IPG}}_{\mathrm{y},k},$$

with $\widetilde{F}^{\mathrm{h}}_{[\mathrm{x,y}]}$, $\tau_{[\mathrm{x,y}],k+1/2}$ and $F^{\mathrm{IPG}}_{[\mathrm{x,y}],k}$ defined in (4.4), (4.3) and (4.5).

The layer-integrated temperature equation (3.10) is:

$$\partial_t\left(h_k\Theta_k\right)+\partial_x\left(h_k u_k\Theta_k\right)+\partial_y\left(h_k v_k\Theta_k\right)+\left(w^{\mathrm{s}}_{k+1/2}\widetilde{\Theta}_{k+1/2}-w^{\mathrm{s}}_{k-1/2}\widetilde{\Theta}_{k-1/2}\right)$$

$$=-\partial_x\left(h_k J^{\Theta}_{\mathrm{x},k}\right)-\partial_y\left(h_k J^{\Theta}_{\mathrm{y},k}\right)-\left(J^{\Theta}_{\mathrm{z},k+1/2}-J^{\Theta}_{\mathrm{z},k-1/2}\right) \tag{A.4}$$

$$+\frac{1}{C_p\rho_0}\left(I_{k+1/2}-I_{k-1/2}\right).$$

The layer-integrated salinity equation (3.12) is:

$$\partial_t\left(h_k S_k\right)+\partial_x\left(h_k u_k S_k\right)+\partial_y\left(h_k v_k S_k\right)+\left(w^{\mathrm{s}}_{k+1/2}\widetilde{S}_{k+1/2}-w^{\mathrm{s}}_{k-1/2}\widetilde{S}_{k-1/2}\right)$$

$$=-\partial_x\left(h_k J^{\mathrm{S}}_{\mathrm{x},k}\right)-\partial_y\left(h_k J^{\mathrm{S}}_{\mathrm{y},k}\right)-\left(J^{\mathrm{S}}_{\mathrm{z},k+1/2}-J^{\mathrm{S}}_{\mathrm{z},k-1/2}\right). \tag{A.5}$$

References

References

Adcroft, A., Hallberg, R., Harrison, M., 2008. A finite volume discretization of the pressure gradient force using analytic integration. Ocean Modell. 22, 106–113.

Adcroft, A., Hill, C., Marshall, J., 1997. Representation of topography by shaved cells in a height coordinate ocean model. Mon. Wea. Rev. 125, 2293–2315.

Adcroft, A.J., Campin, J.M., 2004. Rescaled height coordinates for accurate representation of free-surface flows in ocean circulation models. Ocean Modell. 7, 269–284.

Adcroft, A.J., Hallberg, R.W., 2006. On methods for solving the oceanic equations of motion in generalized vertical coordinates. Ocean Modell. 11, 224–233.

Arakawa, A., Lamb, V.R., 1977. Computational design of the basic dynamical processes of the UCLA General Circulation Model. Meth. Comput. Phys. 17, 174–267.

Auclair, F., Bordois, L., Dossmann, Y., Duhaut, T., Paci, A., Ulses, C., Nguyen, C., 2016. A non-hydrostatic non-Boussinesq algorithm for free-surface ocean modelling. Ocean Modell. In revision.

Auclair, F., Estournel, C., Floor, J.W., Herrmann, M.J., Nguyen, C., Marsaleix, P., 2011. A non-hydrostatic algorithm for free-surface ocean modelling. Ocean Modelling 36, 49–70.

BACC II Author Team, 2015. Second assessment of climate change for the Baltic Sea basin. Springer.

Bachmann, S.D., Fox-Kemper, B., Pearson, B., 2017. A scale-aware subgrid model for quasi-geostrophic turbulence. Journal of Geophysical Research: Oceans 122, 1529–1554.

Backhaus, J.O., 1976. Zur Hydrodynamik im Flachwassergebiet. Ein numerisches modell. Dt. Hydrogr. Z. 29, 222–238.

Backhaus, J.O., 1985. A three-dimensional model for the simulation of shelf sea dynamics. Dt. Hydrogr. Z. 38, 165–187.

Barnier, B., Marchesiello, P., Miranda, A.P.D., Molines, J.M., Coulibaly, M., 1998. A sigma-coordinate primitive equation model for studying the circulation in the south atlantic. part i: Model configuration with error estimates. Deep-Sea Res. 45, 543–572.

Beckers, J.M., Burchard, H., Campin, J.M., Deleersnijder, E., Mathieu, P.P., 1998. Another reason why simple discretizations of rotated diffusion operators cause problems in ocean models. Comments on the paper *isoneutral diffusion in a z-coordinate ocean model* by Griffies et al. J. Phys. Oceanogr. 28, 1552–1559.

Beckers, J.M., Burchard, H., Deleersnijder, E., Mathieu, P.P., 2000. On the numerical discretization of rotated diffusion operators in ocean models. Mon. Wea. Rev. 128, 2711–2733.

Beckers, J.M., Deleersnijder, E., 1993. Stability of a FBTCS scheme applied to the propagation of shallow-water inertia-gravity waves on various space grids. J. Comp. Phys. 108, 95–104.

Beckmann, A., Döscher, R., 1997. A method for improved representation of dense water spreading over topography in geopotential-coordinate models. J. Phys. Oceanogr. 27, 581–591.

Berntsen, J., 2011. A perfectly balanced method for estimating the internal pressure gradients in σ-coordinate ocean models. Ocean Modell. 38, 85–95.

Berntsen, J., Furnes, G., 2005. Internal pressure errors in sigma-coordinate ocean models – sensitivity of the growth of the flow to the time stepping method and possible non-hydrostatic effects. Continental Shelf Research 25, 829–848.

Beron-Vera, F., Ochoa, J., Ripa, P., 1999. A note on boundary conditions for salt and freshwater balances. Ocean Modell. 1, 111–118.

Blaas, M., Dong, C., Marchesiello, P., McWilliams, J.C., Stolzenbach, K.D., 2007. Sediment-transport modeling on southern californian shelves: A roms case study. Cont. Shelf Res. 27, 832–853.

Blayo, E., 2000. Compact finite difference schemes for ocean models: 1. ocean waves. J. Comp. Phys. 164, 241–257.

Blayo, E., Debreu, L., 2005. Revisiting open boundary conditions from the point of view of characteristic variables. Ocean Modell. 9, 231–252.

Bleck, R., 2002. An oceanic general circulation model framed in hybrid isopycnic-Cartesian coordinates. Ocean Modell. 4, 55–88.

Bleck, R., Smith, L.T., 1990. A wind-driven isopycnic coordinate model of the north and equatorial atlantic ocean: 1. model development and supporting experiments. J. Geophys. Res. 95, 3273–3285.

Blumberg, A.F., 1992. A Primer for ECOM-si. Technical Report. HydroQual, Inc.

Blumberg, A.F., Mellor, G.L., 1978. A coastal ocean numerical model, in: Sündermann, J., Holz, K.P. (Eds.), Mathematical Modelling of Estuarine Physics. Springer-Verlag, New York, pp. 203–214.

Blumberg, A.F., Mellor, G.L., 1987. A description of a coastal ocean circulation model, in: Heaps, N.S. (Ed.), Three dimensional ocean models. American Geophysical Union, Washington, D.C., pp. 1–16.

Bolding, K., Burchard, H., Pohlmann, T., Stips, A., 2002. Turbulent mixing in the Northern North Sea: a numerical model study. Cont. Shelf Res. 22, 2707–2724.

Bott, A., 2010. Improving the time-splitting errors of one-dimensional advection schemes in multidimensional applications. Atmos. Res. 97, 619–631.

Botta, N., Klein, R., Langenberg, S., Lützenkirchen, S., 2004. Well balanced finite volume methods for nearly hydrostatic flows. J. Comp. Phys. 196, 539–565.

Brown, J.A., Campana, K.A., 1978. An economical time-differencing system for numerical weather prediction. Mon. Wea. Rev. 106, 1125–1136.

Bruggeman, J., Bolding, K., 2014. A general framework for aquatic biogeochemical models. Environmental Modelling & Software 61, 249–265.

Burchard, H., 2001. Simulating the wave-enhanced layer under breaking surface waves with two-equation turbulence models. J. Phys. Oceanogr. 31, 3133–3145.

Burchard, H., 2002a. Applied turbulence modelling in marine waters. volume 100 of *Lecture Notes in Earth Sciences*. Springer, Berlin, Heidelberg, New York.

Burchard, H., 2002b. Energy-conserving discretisation of turbulent shear and buoyancy production. Ocean Modell. 4, 347–361.

Burchard, H., Badewien, T.H., 2015. Thermohaline residual circulation of the Wadden Sea. Ocean Dyn. 65, 1717–1730.

Burchard, H., Baumert, H., 1995. On the performance of a mixed-layer model based on the k-ε turbulence closure. J. Geophys. Res. 100, 8523–8540.

Burchard, H., Baumert, H., 1998. The formation of estuarine turbidity maxima due to density effects in the salt wedge. A hydrodynamic process study. J. Phys. Oceanogr. 28, 309–321.

Burchard, H., Beckers, J.M., 2004. Non-uniform adaptive vertical grids in one-dimensional numerical ocean models. Ocean Modell. 6, 51–81.

Burchard, H., Bolding, K., 2002. GETM – a general estuarine transport model. Scientific Documentation. Technical Report. European Commission.

Burchard, H., Bolding, K., Villarreal, M.R., 2004. Three-dimensional modelling of estuarine turbidity maxima in a tidal estuary. Ocean Dyn. 54, 250–265.

Burchard, H., Craig, P.D., Gemmrich, J.R., van Haren, H., Mathieu, P.P., Meier, H.E.M., Nimmo Smith, W.A.M., Prandke, H., Rippeth, T.P., Skyllingstad, E.D., Smyth, W.D., Welsh, D.J.S., Wijesekera, H.W.,

2008. Observational and numerical modelling methods for quantifying coastal ocean turbulence and mixing. Progr. Oceanogr. 76, 399–442.

Burchard, H., Deleersnijder, E., Stoyan, G., 2005. Some numerical aspects of turbulence-closure models, in: Baumert, H.Z., Simpson, J.H., Sündermann, J. (Eds.), Marine Turbulence: Theories, Observations and Models. Cambridge University Press, Cambridge, Cambridge, pp. 197–206.

Burchard, H., Petersen, O., 1997. Hybridization between σ- and z-co-ordinates for improving the internal pressure gradient calculation in marine models with steep bottom slopes. Int. J. Numer. Meth. Fl. 25, 1003–1023.

Burchard, H., Petersen, O., 1999. Models of turbulence in the marine environment – A comparative study of two-equation turbulence models. J. Mar. Syst. 21, 29–53.

Burchard, H., Petersen, O., Rippeth, T.P., 1998. Comparing the performance of the Mellor-Yamada and the k-ε two-equation turbulence models. J. Geophys. Res. 103, 10543–10554.

Burchard, H., Rennau, H., 2008. Comparative quantification of physically and numerically induced mixing in ocean models. Ocean Modell. 20, 293–311.

Burchard, H., Rippeth, T.P., 2009. Generation of bulk shear spikes in shallow stratified tidal seas. J. Phys. Oceanogr. 39, 969–985.

Capet, X., Campos, E.J., Paiva, A.M., 2008. Submesoscale activity over the Argentinian shelf. Geophys. Res. Lett. 35, 10.1029/2008GL034736.

Carpenter, J.R., Merckelbach, L., Callies, U., Clark, S., Gaslikova, L., Baschek, B., 2016. Potential impacts of offshore wind farms on North Sea stratification. PloS one 11(8), e0160830.

Casulli, V., Cattani, E., 1994. Stability, accuracy and efficiency of a semi-implicit method for three-dimensional shallow water flow. Computers Math. Appl. 27, 99–112.

Casulli, V., Cheng, R.T., 1992. Semi-implicit finite difference methods for three-dimensional shallow water flow. Int. J. Numer. Meth. Fluids 15, 629–648.

Cheng, R.T., Casulli, V., Gartner, J.W., 1993. Tidal, Residual, Intertidal Mudflat (TRIM) model and its applications to San Francisco Bay, California. Estuar., Coast. Shelf S. 36, 235–280.

Chorin, A.J., 1968. Numerical Solution of the Navier-Stokes Equations. Mathematics of Computation 22, 745–762.

Conley, D.J., Paerl, H.W., Howarth, R.W., Boesch, D.F., Seitzinger, S.P., Havens, K.E., Lancelot, C., Likens, G.E., 2009. Controlling eutrophication: nitrogen and phosphorus. Science 323(5917), 1014–1015.

Craig, P.D., 1989. A model for diurnally forced vertical current structure near 30° latitude. Cont. Shelf Res. 9, 965–980.

Cushman-Roisin, B., Beckers, J.M., 2011. Introduction to geophysical fluid dynamics: physical and numerical aspects. volume 101. Academic Press.

Danabasoglu, G., Yeager, S.G., Bailey, D., Behrens, E., Bentsen, M., Bi, D., Biastoch, A., Böning, C., Bozec, A., Canuto, V.M., et al., 2014. North Atlantic simulations in coordinated ocean-ice reference experiments phase II (CORE-II). Part I: mean states. Ocean Modell. 73, 76–107.

Danilov, S., 2013. Ocean modeling on unstructured meshes. Ocean Modell. 69, 195 – 210.

Daru, V., Tenaud, C., 2004. High order one-step monotonicity-preserving schemes for unsteady compressible flow calculations. J. Comp. Phys. 193, 563–594.

Davies, H.C., 1976. A lateral boundary formulation for multi-level prediction models. Q. J. R. Meteorolog. S. 102, 405–418.

Debreu, L., Blayo, E., 2008. Two-way embedding algorithms: a review. Ocean Dyn. 58, 415–428.

Defne, Z., Ganju, N.K., 2015. Quantifying the residence time and flushing characteristics of a shallow,

back-barrier estuary: application of hydrodynamic and particle tracking models. Estuaries and Coasts 38, 1719–1734.

Deleersnijder, E., 1993. Numerical mass conservation in a free-surface sigma coordinate marine model with mode splitting. Journal of Marine Systems 4, 365–370.

Deleersnijder, E., Beckers, J.M., 1992. On the use of the σ-coordinate system in regions of large bathymetric variations. J. Mar. Syst. 3, 381–390.

Deleersnijder, E., Beckers, J.M., Campin, J.M., El Mohajir, M., Fichefet, T., Luyten, P., 1997. Some mathematical problems associated with the development and use of marine models, in: Diaz, J.I. (Ed.), The mathematics of models for climatology and environment. Springer, Berlin, Heidelberg. volume 48 of *NATO ASI Series*, pp. 41–86.

Delhez, E.J.M., Grégoire, M., Nihoul, J.C.J., Beckers, J.M., 1999. Dissection of the GHER turbulence closure scheme. J. Mar. Syst. 21, 379–397.

Demange, J., Debreu, L., Marchesiello, P., Lemarié, F., Blayo, E., 2014. Numerical representation of internal waves propagation. Research report. INRIA. Available online at `http://hal.inria.fr/hal-01063417/PDF/RR-8590.pdf`.

Diaz, R.J., Rosenberg, R., 2008. Spreading dead zones and consequences for marine ecosystems. science 321, 926–929.

Dukhovskoy, D.S., Moreay, S.L., Martin, P.J., O'Brien, James J. Cooper, C., 2009. Application of a vanishing, quasi-sigma, vertical coordinate for simulation of high-speed, deep currents over the Sigsbee Escarpment in the Gulf of Mexico. Ocean Modelling 28, 250–265.

Dukowicz, J.K., 2001. Reduction of density and pressure gradient errors in ocean simulations. J. Phys. Oceanogr. 31, 1915–1921.

Durran, D.R., 2010. Numerical Methods for Fluid Dynamics With Applications to Geophysics. Springer. 2nd edition.

Durski, S.M., Glenn, S.M., Haidvogel, D.B., 2004. Vertical mixing schemes in the coastal ocean: Comparison of the level 2.5 Mellor-Yamada scheme with an enhanced version of the K profile parameterisation. J. Geophys. Res. 109, C01015, doi:10.1029/2002JC001702.

Eden, C., Czeschel, L., Olbers, D., 2014. Toward energetically consistent ocean models. J. Phys. Oceanogr. 44, 3160–3184.

Eden, C., Greatbatch, R.J., 2008. Towards a mesoscale eddy closure. Ocean Modell. 20, 223–239.

Espelid, T.O., Berntsen, J., Barthel, K., 2000. Conservation of energy for schemes applied to the propagation of shallow-water inertia-gravity waves in regions with varying depth. Int. J. for Numer. Meth. Eng. 49, 1521–1545.

Ezer, T., Mellor, G.L., 2004. A generalised coordinate ocean model and a comparison of the bottom boundary layer dynamics in terrain-following and in z-level grids. Øcean Modell. 6, 379–403.

Fairall, C.W., Bradley, E.F., Rogers, D.P., Edson, J.B., Young, G.S., 1996. Bulk parameterization of air-sea fluxes for Tropical Ocean-Global Atmosphere Coupled-Ocean Atmosphere Response Experiment. J. Geophys. Res. 101, 3747–3764.

Feagin, R.A., Sherman, D.J., Grant, W.E., 2005. Coastal erosion, global sea-level rise, and the loss of sand dune plant habitats. Frontiers in Ecology and the Environment 3, 359–364.

Fennel, W., Seifert, T., Kayser, B., 1991. Rossby radii and phase speeds in the Baltic Sea. Cont. Shelf Res. 11, 23–36.

Flather, R., 1976. A tidal model of the north-west european continental shelf. Memoires de la Societe Royale des Sciences de Liege 6, 141–164.

Flather, R.A., Heaps, N.S., 1975. Tidal computations for Morecambe Bay. Geophys. J. Roy. Astron. Soc.

42, 489–517.

Fofonoff, N.P., Millard Jr., R.C., 1983. Algorithms for computation of fundamental properties of seawater. Technical Report. UNESCO. Unesco technical papers in marine science 44.

Fox-Kemper, B., Danabasoglu, G., Ferrari, R., Griffies, S., Hallberg, R., Holland, M., Maltrud, M., Peacock, S., Samuels, B., 2011. Parameterization of mixed layer eddies. iii: Implementation and impact in global ocean climate simulations. Ocean Modelling 39(1), 61–78.

Fox-Kemper, B., Menemenlis, D., 2008. Can Large Eddy Simulation Techniques Improve Mesoscale Rich Ocean Models?, in: Ocean Modeling in an Eddying Regime. AGU. number 177 in Geophysical Monograph Series, pp. 319–337.

Galperin, B., Kantha, L.H., Hassid, S., Rosati, A., 1988. A quasi-equilibrium turbulent energy model for geophysical flows. J. Atmos. Sci. 45, 55–62.

Gao, X., Chen, C.T.A., 2012. Heavy metal pollution status in surface sediments of the coastal Bohai Bay. Water Research 46, 1901–1911.

Gaspar, P., Gregoris, Y., Lefevre, J., 1990. A simple eddy kinetic energy model for simulations of the oceanic vertical mixing: Tests at station Papa and long-term upper ocean study site. J. Geophys. Res. 95, 16179–16193.

Gent, P.R., McWilliams, J.C., 1990. Isopycnal mixing in ocean circulation models. J. Phys. Oceanogr. 20, 150–155.

Gerdes, R., 1993. A primitive equation ocean circulation model using a general vertical coordinate transformation. 1. Description and testing of the model. J. Geophys. Res. 98, 14683–14701.

Gerritsen, H., De Goede, E., Genseberger, M., Uittenbogaard, R., 2004. Validation Document Delft3D-FLOW. Technical Report. WL Delft Hydraulics.

Gottlieb, S., Shu, C.W., 1998. Total variation diminishing runge-kutta schemes. Math. Comput. 67, 73–85.

Gräwe, U., Flöser, G., Gerkema, T., Duran-Matute, M., Badewien, T., Schulz, E., Burchard, H., 2016. A numerical model for the entire Wadden Sea: skill assessment and analysis of hydrodynamics. J. Geophys. Res. 121, 5231–5251.

Gräwe, U., Holtermann, P., Klingbeil, K., Burchard, H., 2015. Advantages of vertically adaptive coordinates in numerical models of stratified shelf seas. Ocean Modell. 92, 56–68.

Griffies, S., Adcroft, A., 2008. Formulating the equations of ocean models, in: Hecht, M., Hasumi, H. (Eds.), Ocean Modeling in an Eddying Regime. American Geophysical Union, Washington, D.C.. volume 177 of *Geophysical Monograph Series*, pp. 281–317.

Griffies, S.M., 2004. Fundamentals of ocean climate models. volume 518. Princeton University Press.

Griffies, S.M., 2007. Elements of mom4p1. Technical Report. NOAA/GFDL. Version prepared on September 27, 2007.

Griffies, S.M., Boning, C., Bryan, F.O., Chassignet, E.P., Gerdes, R., Hasumi, H., Hirst, A., Treguier, A.M., Webb, D., 2000. Developments in ocean climate modelling. Ocean Modell. 2, 123–192.

Griffies, S.M., Gnanadesikan, A., Pacanowski, R.C., Larichev, V.D., Dukowicz, J.K., Smith, R.D., 1998. Isoneutral diffusion in a z-coordinate ocean model. J. Phys. Oceanogr. 28, 805–830.

Griffies, S.M., Hallberg, R.W., 2000. Biharmonic Friction with a Smagorinsky-Like Viscosity for Use in Large-Scale Eddy-Permitting Ocean Models. Monthly Weather Review 128, 2935–2946.

Gröger, M., Dieterich, C., Meier, M.H., Schimanke, S., 2015. Thermal air-sea coupling in hindcast simulations for the North Sea and Baltic Sea on the NW European shelf. Tellus A 67.

Haidvogel, D.B., Arango, H.G., Hedstrom, K., Beckmann, A., Malanotte-Rizzoli, P., Shchepetkin, A.F., 2000. Model evaluation experiments in the north atlantic basin: simulations in nonlinear terrain-following coordinates. Dynam. Atmos. Ocean 32, 239–281.

Halpern, B.S., Walbridge, S., Selkoe, K.A., Kappel, C.V., Micheli, F., D'agrosa, C., Bruno, J.F., Casey, K.S., Ebert, C., Fox, H.E., Fujita, R., Heinemann, D., Lenihan, H.S., Madin, E.M.P., Perry, M.T., Selig, E.R., Spalding, M., Steneck, R., Watson, R., 2008. A global map of human impact on marine ecosystems. Science 319(5865), 948–952.

Haney, R.L., 1991. On the pressure gradient force over steep topography in sigma coordinate ocen models. J. Phys. Oceanogr. 21, 610–619.

Harcourt, R.R., 2014. A second-moment closure model of Langmuir Turbulence. J. Phys. Oceanogr. 43, 673–697.

van Haren, H., Maas, L., Zimmerman, J.T.F., Malschaert, H.R.H., 1999. Strong inertial currents and marginal internal wave stability in the central North Sea. Geophys. Res. Lett. 26, 2993–2996.

Harten, A., 1983. High resolution schemes for hyperbolic conservation laws. J. Comput. Phys. 49, 357–393.

Heggelund, Y., Vikebø, F., Berntsen, J., Furnes, G., 2004. Hydrostatic and non-hydrostatic studies of gravitational adjustment over a slope. Continental Shelf Research 24, 2133–2148.

Hirt, C.W., Amsden, A.A., Cook, J.L., 1974. An Arbitrary Lagrangian-Eulerian Computing Method for All Flow Speeds. J. Comput. Phys. 14, 227–253.

Hofmeister, R., Bolding, K., Hetland, R.D., Schernewski, G., Siegel, H., Burchard, H., 2013. The dynamics of cooling water discharge in a shallow, non-tidal embayment. Cont. Shelf Res. 71, 68–77.

Hofmeister, R., Burchard, H., Beckers, J.M., 2010. Non-uniform adaptive vertical grids for 3d numerical ocean models. Ocean Modell. 33, 70–86.

Holt, J., Harle, J., Proctor, R., Michel, S., Ashworth, M., Batstone, C., Allen, I., Holmes, R., Smyth, T., Haines, K., Bretherton, D., Smith, G., 2009. Modelling the global coastal ocean. Philosophical Transactions of the Royal Society of London A: Mathematical, Physical and Engineering Sciences 367, 939–951.

Holt, J.T., James, I.D., 2001. An s coordinate density evolving model of the northwest european continental shelf: 1. model description and density structure. J. Geophys. Res. 106, 14015–14034.

Holt, J.T., James, I.D., 2006. An assessment of the fine-scale eddies in a high-resolution model of the shelf seas west of Great Britain. Ocean Modell. 13, 271–291.

Hordoir, R., Axell, L., Löptien, U., Dietze, H., Kuznetsov, I., 2015. Influence of sea level rise on the dynamics of salt inflows in the Baltic Sea. Journal of Geophysical Research: Oceans 120, 6653–6668.

Horner-Devine, A.R., Hetland, R.D., MacDonald, D.G., 2015. Mixing and transport in coastal river plumes. Annu. Rev. Fluid Mech. 47, 569–594.

Hundsdorfer, W., Trompert, R.A., 1994. Method of lines and direct discretization: A comparison for linear advection. Appl. Numer. Math. 13, 469–490.

Huthnance, J.M., 1995. Circulation, exchange and water masses at the ocean margin: the role of physical processes at the shelf edge. Progr. Oceanogr. 35, 353–431.

Ilicak, M., Adcroft, A.J., Griffies, S.M., Hallberg, R.W., 2012. Spurious dianeutral mixing and the role of momentum closure. Ocean Modell. 45-46, 37–58.

IOC, SCOR and IAPSO, 2010. The international thermodynamic equation of seawater - 2010: Calculation and use of thermodynamic properties. Technical Report. Intergovernmental Oceanographic Commission. UNESCO.

Jackson, J.B.C., Kirby, M.X., Berger, W.H., Bjorndal, K.A., Botsford, L.W., Bourque, B.J., Bradbury, R.H., Cooke, R., Erlandson, J., Estes, J.A., Hughes, T.P., Kidwell, S., Lange, C.B., Lenihan, H.S., Pandolfi, J.M., Peterson, C.H., Steneck, R.S., Tegner, M.J., Warner, R.R., 2001. Historical overfishing and the recent collapse of coastal ecosystems. science 293(5530), 629–637.

Jackson, L., Hallberg, R., Legg, S., 2008. A parameterization of shear-driven turbulence for ocean climate models. J. Phys. Oceanogr. 38, 1033–1053.

James, I., 2000. A high-performance explicit vertical advection scheme for ocean models: how {PPM} can beat the {CFL} condition. Appl. Math. Model. 24(1), 1 – 9.

Jay, D.A., Musiak, J.D., 1994. Particle trapping in estuarine tidal flows. J. Geophys. Res. 99, 20445–20461.

Jensen, T.G., 1998. Open boundary conditions in stratified ocean models. J. Mar. S. 16, 297–322.

Johns, B., Marsaleix, P., Estournel, C., Vhil, R., 1992. On the wind-driven coastal upwelling in the gulf of lions. J. Mar. S. 3, 309–320.

Jungclaus, J.H., Backhaus, J.O., 1994. Application of a transient reduced gravity plume model to the denmark strait overflow. J. Geophys. Res. 99, 12375–12396.

Kållberg, P., 1977. Test of a lateral boundary relaxation scheme in a barotropic model. Internal Report. ECMWF Research Department.

van Kan, J., 1986. A second-order accurate pressure correction scheme for viscous incompressible flow. Journal of Science and Statistical Computation 7, 870–891.

Kanarska, Y., Maderich, V., 2003. A non-hydrostatic numerical model for calculating free-surface stratified flows. Ocean Dynamics 53, 176–185.

Kanarska, Y., Shchepetkin, A., McWilliams, J., 2007. Algorithm for non-hydrostatic dynamics in the Regional Oceanic Modeling System. Ocean Modell. 18, 143–174.

Kantha, L.H., Clayson, C.A., 2000a. Numerical models of oceans and oceanic processes. volume 66 of *International Geophysics Series*. Academic Press.

Kantha, L.H., Clayson, C.A., 2000b. Small-scale processes in geophysical fluid flows. volume 67 of *International Geophysics Series*. Academic Press.

Kasahara, A., 1974. Various Vertical Coordinate Systems Used For Numerical Weather Prediction. Mon. Wea. Rev. 102, 509–522.

Keilegavlen, E., Berntsen, J., 2009. Non-hydrostatic pressure in σ-coordinate ocean models. Ocean Modelling 28, 240–249.

Klingbeil, K., Burchard, H., 2013. Implementation of a direct nonhydrostatic pressure gradient discretisation into a layered ocean model. Ocean Modell. 65, 64–77.

Klingbeil, K., Mohammadi-Aragh, M., Gräwe, U., Burchard, H., 2014. Quantification of spurious dissipation and mixing - discrete variance decay in a finite-volume framework. Ocean Modell. 81, 49–64.

Knight, P.J., Howarth, M.J., Rippeth, T.P., 2002. Inertial currents in the Northern North Sea. J. Sea Res. 47, 269–284.

Kondo, J., 1975. Air-sea bulk transfer coefficients in diabatic conditions. Bound. Layer Meteor. 9, 91–112.

Lahaye, S., Gouillon, F., Baraille, R., Pichon, A., Pineau-Guillou, L., Morel, Y., 2011. A numerical scheme for modeling tidal wetting and drying. J. Geophys. Res. 116. C03028.

Large, W.G., McWilliams, J.C., Doney, S.C., 1994. Oceanic vertical mixing: a review and a model with nonlocal boundary layer parameterisation. Rev. Geophys. 32, 363–403.

Lazure, P., Salomon, J.C., 1991. Coupled 2-d and 3-d modeling of coastal hydrodynamics. Oceanol. Acta 14, 173–180.

Leclair, M., Madec, G., 2011. $\tilde{z}$-coordinate, an arbitrary lagrangian-eulerian coordinate separating high and low frequency motions. Ocean Modell. 37, 139–152.

Lemarié, F., Debreu, L., Madec, G., Demange, J., Molines, J., Honnorat, M., 2015. Stability constraints for oceanic numerical models: implications for the formulation of time and space discretizations. Ocean Modell. 92, 124–148.

Lemarié, F., Debreu, L., Shchepetkin, A., McWilliams, J., 2012a. On the stability and accuracy of the harmonic and biharmonic isoneutral mixing operators in ocean models. Ocean Modell. 52-53, 9–35.

Lemarié, F., Kurian, J., Shchepetkin, A.F., Molemaker, M.J., Colas, F., McWilliams, J.C., 2012b. Are There Inescapable Issues Prohibiting the use of Terrain-Following Coordinates in Climate Models ? Ocean Modell. 42, 57–79.

Lenhart, H.J., Mills, D.K., Baretta-Bekker, H., Van Leeuwen, S.M., Van Der Molen, J., Baretta, J.W., Blaas, M., Desmit, X., Kühn, W., Lacroix, G., et al., 2010. Predicting the consequences of nutrient reduction on the eutrophication status of the North Sea. J. Mar. Syst. 81, 148–170.

Lilly, D.K., 1965. On the computational stability of numerical solutions of time-dependent non-linear geophysical fluid dynamics problems. Mon. Wea. Rev. 93, 11–25.

Lin, S.J., 1997. A finite-volume integration method for computing pressure gradient force in general vertical coordinates. Quart. J. Roy. Meteorol. Soc. 123, 1749–1762.

Lorenz, E.N., 1960. Energy and Numerical Weather Prediction. Tellus 12, 364–373.

Lotze, H.K., Lenihan, H.S., Bourque, B.J., Bradbury, R.H., Cooke, R.G., Kay, M.C., Kidwell, S.M., Kirby, M.X., Peterson, C.H., Jackson, J.B.C., 2006. Depletion, degradation, and recovery potential of estuaries and coastal seas. Science 312, 1806–1809.

Lundquist, K.A., Chow, F.K., Lundquist, J.K., 2010. An immersed boundary method for the weather research and forecasting model. Mon. Wea. Rev. 138, 796–817.

Luyten, P., Jones, J., Proctor, R., Tabor, A., Tett, P., Wild-Allen, K., 1999. COHERENS - A coupled hydrodynamical-ecological model for regional and shelf seas: User Documentation. Technical Report. MUMM Report, Management Unit of the Mathematical Models of the north Sea.

MacCready, P., Geyer, W.R., 2010. Advances in estuarine physics. Annu. Rev. Fluid Mech. 2, 35–58.

Madala, R.V., Piacsek, S.A., 1977. A semi-implicit numerical model for baroclinic oceans. J. Comp. Phys. 23, 167–178.

Madec, G., Delecluse, P., Crepon, M., Chartier, M., 1991. A three-dimensional numerical study of deep-water formation in the northwestern mediterranean sea. J. Phys. Oceanogr. 21, 1349–1371.

Marchesiello, P., Debreu, L., Couvelard, X., 2009. Spurious diapycnal mixing in terrain-following coordinate models: The problem and a solution. Ocean Modell. 26, 159–169.

Marchesiello, P., McWilliams, J.C., Shchepetkin, A., 2001. Open boundary conditions for long-term integration of regional oceanic models. Ocean Modell. 3, 1–20.

Marsaleix, P., Auclair, F., Estournel, C., Nguyen, C., Ulses, C., 2011. An accurate implementation of the compressibility terms in the equation of state in a low order pressure gradient scheme for sigma coordinate ocean models. Ocean Modell. 40, 1–13.

Marsaleix, P., Auclair, F., Floor, J.W., Herrmann, M.J., Estournel, C., Pairaud, I., Ulses, C., 2008. Energy conservation issues in sigma-coordinate free-surface ocean models. Ocean Modell. 20, 61–89.

Marsaleix, P., Estournel, C., Kondrachoff, V., Vehil, R., 1998. A numerical study of the formation of the Rhône River plume. J. Marine Syst. 14, 99–115.

Marshall, J., Hill, C., Perelman, L., Adcroft, A.J., 1997. Hydrostatic, quasi-hydrostatic, and nonhydrostatic ocean modeling. Journal of Geophysical Research 102 (C3), 5733–5752.

Martin, P.J., 1985. Simulation of the mixed layer at OWS November and Papa with several models. J. Geophys. Res. 90, 903–916.

Martin, P.J., 2000. Description of the Navy Coastal Ocean Model Version 1.0. Technical Report. NRL Report.

Martinho, A.S., Batteen, M.L., 2006. On reducing the slope parameter in terrain-following numerical ocean models. Ocean Modell. 13, 166–175.

Martins, F., Leitão, P., Silva, A., Neves, R., 2001. 3D modeling in the Sado estuary using a new generic vertical discretization approach. Oceanologica Acta 24, S51–S62.

Martinsen, E.A., Engedahl, H., 1987. Implementation and testing of a lateral boundary scheme as an open boundary condition in a barotropic ocean model. Coast. Eng. 11, 603–627.

Mason, E., Molemaker, J., Shchepetkin, A.F., Colas, F., McWilliams, J.C., Sangrà, P., 2010. Procedures for offline grid nesting in regional ocean models. Ocean Modell. 35, 1–15.

Mathis, M., Elizalde, A., Mikolajewicz, U., Pohlmann, T., 2015. Variability patterns of the general circulation and sea water temperature in the North Sea. Progr. Oceanogr. 135, 91–112.

McCalpin, J.D., 1994. A comparison of second-order and fourth-order pressure gradient algorithms in a σ-coordinate ocean model. Int. J. Numer. Meth. Fl. 18, 361–383.

Meier, H.E.M., Kjellström, E., Graham, L.P., 2006. Estimating uncertainties of projected Baltic Sea salinity in the late 21st century. Geophys. Res. Lett. 33(15), 10.1029/2006GL026488.

Mellor, G.L., 2002. Oscillating bottom boundary layers. J. Phys. Oceanogr. 32, 3075–3088.

Mellor, G.L., Blumberg, A.F., 1985. Modeling vertical and horizontal diffusivities with the sigma coordinate system. Mon. Wea. Rev. 113, 1379–1383.

Mellor, G.L., Ezer, T., Oey, L.Y., 1994. The pressure gradient conundrum of sigma coordinate ocean models. J. Atmos. Ocean. Technol. 11, 1126–1134.

Mellor, G.L., Yamada, T., 1982. Development of a turbulence closure model for geophysical fluid problems. Rev. Geophys. 20, 851–875.

Mesinger, F., Arakawa, A., 1976. Numerical Methods used in atmospheric models, vol. 1. Technical Report. World Meteor. Org. GARP Publ. Ser. 17.

Mohammadi-Aragh, M., Klingbeil, K., Brüggemann, N., Eden, C., Burchard, H., 2015. The impact of advection schemes on restratifiction due to lateral shear and baroclinic instabilities. Ocean Modell. 94, 112–127.

Nataf, F., 2013. Absorbing boundary conditions and perfectly matched layers in wave propagation problems. Direct and Inverse problems in Wave Propagation and Applications 14, 219–231.

Neumann, T., Fennel, W., Kremp, C., 2002. Experimental simulations with an ecosystem model of the Baltic Sea: a nutrient load reduction experiment. Global Biogeochemical Cycles 16, 10.1029/2001GB001450.

Nicholls, R.J., Hoozemans, F.M.J., Marchand, M., 1999. Increasing flood risk and wetland losses due to global sea-level rise: regional and global analyses. Global Environmental Change 9, S69–S87.

Nihoul, J.C., Waleffe, F., Djenidi, S., 1986. A 3d-numerical model of the northern bering sea. Environmental Software 1, 76–81.

O'Dea, E.J., Arnold, A.K., Edwards, K.P., Furner, R., Hydler, P., Martin, M.J., Siddorn, J.R., Storkey, D., While, J., Holt, J.T., Liu, H., 2012. An operational ocean forecast system incorporating NEMO and SST data assimilation for the tidally driven European North-West shelf. Journal of Operational Oceanography 5, 3–17.

Oey, L.Y., 2005. A wetting and drying scheme for POM. Ocean Modell. 9, 133–150.

Olbers, D., Willebrand, J., Eden, C., 2012. Ocean dynamics. Springer-Verlag Berlin Heidelberg.

Oliger, J., Sundström, A., 1978. Theoretical and practical aspects of some initial boundary value problems in fluid dynamics. SIAM J. Appl. Math. 35, 419–446.

Orlanski, I., 1976. A simple boundary condition for unbounded hyperbolic flows. J. Comput. Phys. 21, 251–269.

Oschlies, A., 2002. Improved representation of upper ocean dynamics and mixed layer depths in a model of the North Atlantic on switching from eddy-permitting to eddy-resolving grid resolution. J. Phys.

Oceanogr. 32, 2277–2298.
Palma, E.D., Matano, R.P., 2000. On the implementation of open boundary conditions for a general circulation model: The three-dimensional case. J. Geophys. Res. 105, 8605–8627.
Patankar, S.V., 1980. Numerical Heat Transfer and Fluid Flow. McGraw-Hill, New York.
Paulson, C.A., Simpson, J.J., 1977. Irradiance measurements in the upper ocean. J. Phys. Oceanogr. 7, 952–956.
Peaceman, D.W., Rachford, Jr., H.H., 1955. The numerical solution of parabolic and elliptic differential equations. SIAM Journal 3, 28–41.
Pearson, B., Fox-Kemper, B., Bachman, S., Bryan, F., 2017. Evaluation of scale-aware subgrid mesoscale eddy models in a global eddy-rich model. Ocean Modelling 115, 42–58.
Penven, P., Debreu, L., Marchesiello, P., McWilliams, J.C., 2006. Evaluation and application of the roms 1-way embedding procedure to the central california upwelling system. Ocean Modell. 12, 157–187.
Perkins, A.L., Smedstad, L.F., Blake, D.W., Heburn, G.W., Wallcraft, A.J., 1997. A new nested boundary condition for a primitive equation ocean model. J. Geophys. Res. 102, 3483–3500.
Pietrzak, J., Jakobson, J.B., Burchard, H., Vested, H.J., Petersen, O., 2002. A three-dimensional hydrostatic model for coastal and ocean modelling using a generalised topography following co-ordinate system. Ocean Modell. 4, 173–205.
Quante, M., Colijn, F. (Eds.), 2016. North Sea Region Climate Change Assessment. Springer.
Raymond, W.H., Kuo, H.L., 1984. A radiation boundary condition for multi-dimensional flows. Q.J.R. Meteorol. Soc. 110, 535–551.
Rennau, H., Schimmels, S., Burchard, H., 2012. On the effect of structure-induced resistance and mixing on inflows into the Baltic Sea: a numerical model study. Coastal Engineering 60, 53–68.
Rippeth, T.P., Fisher, N., Simpson, J.H., 2001. The semi-diurnal cycle of turbulent dissipation in the presence of tidal straining. J. Phys. Oceanogr. 31, 2458–2471.
Rodi, W., 1987. Examples of calculation methods for flow and mixing in stratified flows. J. Geophys. Res. 92, 5305–5328.
Roquet, F., Madec, G., McDougall, T.J., Barkerd, P.M., 2015. Accurate polynomial expressions for the density and specific volume of seawater using the TEOS-10 standard. Ocean Modell. , 29–43.
Ross, M.A., Mehta, A.J., 1989. On the mechanics of lutoclines and fluid mud. J. Coastal Res. , 51–62.
Rueda, F.J., Sanmiguel-Rojas, E., Hodges, B.R., 2007. Baroclinic stability for a family of two-level, semi-implicit numerical methods for the 3d shallow water equations. Int. J. Numer. Meth. Fluids 54, 237–268.
Schär, C., Leuenberger, D., Fuhrer, O., Lüthi, D., Girard, C., 2002. A new terrain-following vertical coordinate formulation for atmospheric prediction models. Mon. Wea. Rev. 130, 2459–2480.
Scotti, A., Pineda, J., 2004. Observation of very large and steep internal waves of elevation near the Massachusetts coast. Geophys. Res. Lett. 31, 10.1029/2004GL021052.
Screen, J.A., Simmonds, I., 2010. The central role of diminishing sea ice in recent Arctic temperature amplification. Nature 464, 1334–1337.
Shapiro, G., Luneva, M., Pickering, J., Storkey, D., 2013. The effect of various vertical discretization schemes and horizontal diffusion parameterization on the performance of a 3-d ocean model: the black sea case study. Ocean Sci. 9(2), 377–390.
Shchepetkin, A.F., 2015. An adaptive, courant-number-dependent implicit scheme for vertical advection in oceanic modeling. Ocean Modell. 91, 38–69.
Shchepetkin, A.F., McWilliams, J.C., 2003. A method for computing horizontal pressure-gradient force in an oceanic model with a non-aligned vertical coordinate. J. Geophys. Res. 108 (C3), 3090–3124.

Shchepetkin, A.F., McWilliams, J.C., 2005. The Regional Oceanic Modeling System: A split-explicit, free-surface, topography-following-coordinate ocean model. Ocean Modell. 9, 347–404.

Shchepetkin, A.F., McWilliams, J.C., 2009a. Computational kernel algorithms for fine-scale, multiprocess, longtime oceanic simulations, in: Ciarlet, P.G. (Ed.), Computational methods for the atmosphere and the oceans Special Volume. Elsevier. volume XIV of *Handbook of numerical analysis*, pp. 121–183.

Shchepetkin, A.F., McWilliams, J.C., 2009b. Correction and commentary for "ocean forecasting in terrain-following coordinates: Formulation and skill assessment of the regional ocean modeling system" by Haidvogel et al., J. Comp. Phys. 227, pp. 3595-3624. J. Comput. Phys. 228, 8985–9000.

Sheng, J., Greatbatch, R.J., Zhai, X., Tang, L., 2005. A new two-way nesting technique for ocean modeling based on the smoothed semi-prognostic method. Ocean Dyn. 55, 162–177.

Shu, C.W., 1987. TVB uniformly high-order accurate schemes for conservation laws. Math. Comput. 49, 105–121.

Shu, C.W., 1988. Total-variation-diminishing time discretizations. SIAM J. Sci. Stat. Comput. 9, 1073–1084.

Simons, T.J., 1974. Verification of Numerical Models of Lake Ontario: Part I. Circulation in Spring and Early Summer. Journal of Physical Oceanography 4, 507–523.

Simpson, J.H., Brown, J., Matthews, J., Allen, G., 1990. Tidal straining, density currents, and stirring in the control of estuarine stratification. Estuaries 13, 125–132.

Smagorinsky, J., 1963. General circulation experiments with the primitive equations. Mon. Wea. Rev. 91, 99–164.

Smyth, W.D., Skyllingstad, E.D., Crawford, G.B., Wijesekera, H., 2002. Nonlocal fluxes and stokes drift effects in the K-profile parameterization. Ocean Dyn. 52, 104–115.

Song, Y., Haidvogel, D.B., 1994. A semi-implicit ocean circulation model using a generalised topography-following coordinate. J. Comput. Phys. 115, 228–244.

Soufflet, Y., Marchesiello, P., Lemarié, F., Jouanno, J., Capet, X., Debreu, L., Benshila, R., 2016. On effective resolution in ocean models. Ocean Modell. 98, 36–50.

Starr, V.P., 1945. A quasi-lagrangian system of hydrodynamical equations. Journal of Meteorology 2, 227–237.

Stelling, G.S., Duinmeijer, S.P.A., 2003. A staggered conservative scheme for every Froude number in rapidly varied shallow water flows. Int. J. Numer. Meth. Fluids 43, 1329–1354.

Stelling, G.S., Van Kester, J.A.T.M., 1994. On the approximation of horizontal gradients in sigma co-ordinates for bathymetry with steep bottom slopes. Int. J. Numer. Methods Fluids 18, 915–935.

Stockdon, H.F., Holman, R.A., Howd, P.A., Sallenger, A.H., 2006. Empirical parameterization of setup, swash, and runup. Coastal Engineering 53(7), 573–588.

Suresh, A., Huynh, H., 1997. Accurate monotonicity-preserving schemes with runge-kutta time stepping. J. Comp. Phys. 136, 83–99.

Svendsen, E., Berntsen, J., Skogen, M., dlandsvik, B., Martinsen, E., 1996. Joint numerical sea modelling model simulation of the skagerrak circulation and hydrography during skagex. J. Marine Syst. 8, 219–236.

Sydeman, W.J., García-Reyes, M., Schoeman, D.S., Rykaczewski, R.R., Thompson, S.A., Black, B.A., Bograd, S.J., 2014. Climate change and wind intensification in coastal upwelling ecosystems. Science 345, 77–80.

Témam, R., 1969. Sur l'Approximation de la Solution de Équations de Navier-Stokes par la Méthode de Pas Fractionnaires (II). Arch. Rational Mech. Anal. 32, 377–385.

Témam, R., Tribbia, J., 2003. Open boundary conditions for the primitive and boussinesq equations. J.

Atmos. Sci. 60, 2647–2660.
Uchiyama, Y., McWilliams, J.C., Shchepetkin, A.F., 2010. Wave-current interaction in an oceanic circulation model with a vortex-force formalism: Application to the surf zone. Ocean Modell. 34, 16–35.
Umlauf, L., Burchard, H., 2003. A generic length-scale equation for geophysical turbulence models. J. Mar. Res. 61, 235–265.
Umlauf, L., Burchard, H., 2005. Second-order turbulence models for geophysical boundary layers. A review of recent work. Cont. Shelf Res. 25, 795–827.
Van Maren, D.S., Oost, A.P., Wang, Z.B., Vos, P.C., 2016. The effect of land reclamations and sediment extraction on the suspended sediment concentration in the ems estuary. Mar. Geol. 376, 147–157.
Vitousek, S., Fringer, O., 2011. Physical vs numerical dispersion in nonhydrostatic ocean modeling. Ocean Modell. 40, 72–86.
Wahl, T., Haigh, I.D., Woodworth, P.L., Albrecht, F., Dillingh, D., Jensen, J., Nicholls, R.J., Weisse, R., Wöppelmann, G., 2013. Observed mean sea level changes around the North Sea coastline from 1800 to present. Earth-Science Reviews 124, 51–67.
Waldron, K.M., Paegle, J., Horel, J.D., 1996. Sensitivity of a spectrally filtered and nudged limited-area model to outer model options. Mon. Wea. Rev. 124, 529–547.
Walters, R.A., Lane, E.M., Hanert, E., 2009. Useful time-stepping methods for the Coriolis term in a shallow water model. Ocean Modell. 28, 66–74.
Warner, J.C., Defne, Z., Haas, K., Arango, H.G., 2013. A wetting and drying scheme for ROMS. Computers & Geosci. 58, 54–61.
Warner, J.C., Sherwood, C.R., Arango, H.G., Signell, R.P., 2005. Performance of four turbulence closure models implemented using a generic length scale method. Ocean Modell. 8, 81–113.
Warner, J.C., Sherwood, C.R., Signell, R.P., Harris, C.K., Arango, H.G., 2008. Development of a three-dimensional, regional, coupled wave, current, and sediment-transport model. Computers & Geosci. 34, 1284–1306.
Weller, H., Shahrokhi, A., 2014. Curl-free pressure gradients over orography in a solution of the fully compressible euler equations with implicit treatment of acoustic and gravity waves. Mon. Wea. Rev. 142, 4439–4457.
Wheless, G.H., Klinck, J.M., 1995. The evolution of density-driven circulation over sloping bottom topography. J. Phys. Oceanogr. 25, 888–901.
White, L., Adcroft, A., Hallberg, R., 2009. High-order regridding-remapping schemes for continuous isopycnal and generalized coordinates in ocean models. J. Comput. Phys. 228, 8665–8692.
White, L., Adcroft, A.J., 2008. A high-order finite volume remapping scheme for nonuniform grids: The piecewise quartic method (PQM). J. Comput. Phys. 227, 7394–7422.
Wilcox, D.C., 1998. Turbulence Modeling for CFD. DCW Industries. 2 edition.
Wilkin, J.L., Arango, H.G., Haidvogel, D.B., Lichtenwalner, C., Glenn, S.M., Hedström, K.S., 2005. A regional ocean modeling system for the long-term ecosystem observatory. J. Geophys. Res. 110.
Wiltshire, K.H., Manly, B.F.J., 2004. The warming trend at Helgoland Roads, North Sea: phytoplankton response. Helgol. Mar. Res. 58, 269–273.
Winterwerp, J.C., Wang, Z.B., van Braeckel, A., van Holland, G., Kösters, F., 2013. Man-induced regime shifts in small estuariesII: a comparison of rivers. Ocean Dyn. 63, 1293–1306.